



NYU

POLYTECHNIC SCHOOL
OF ENGINEERING



NYU WIRELESS TR 2015-002

Technical Report

Indoor Office Wideband Millimeter-Wave Propagation Measurements and Channel Models at 28 GHz and 73 GHz for Ultra- Dense 5G Wireless Networks

Results published in:

G. R. MacCartney, Jr., T. S. Rappaport, S. Sun, and S. Deng, "Indoor Office Wideband Millimeter-Wave Propagation Measurements and Channel Models at 28 GHz and 73 GHz for Ultra-Dense 5G Wireless Networks, (Invited Paper)," *IEEE Access*, 2015.

**George R. MacCartney, Jr., Sijia Deng, Shu Sun, and
Theodore S. Rappaport**

gmac@nyu.edu, sijia @nyu.edu, ss7152@nyu, and tsr@nyu.edu

NYU WIRELESS
NYU Polytechnic School of Engineering
2 MetroTech Center
Brooklyn, NY 11201

Oct. 1, 2015

This page is intentionally left blank.

Acknowledgements

This material is based upon work supported by the NYU WIRELESS Industrial Affiliates: AT&T, CableLabs, Cablevision, Ericsson, Huawei, Intel Corporation, InterDigital Inc., Keysight Technologies, L3 Communications, Nokia, National Instruments, Qualcomm Technologies, Samsung Corporation, SiBeam, Straight Path Communications, and UMC. This work is also supported by the GAANN Fellowship Program and three National Science Foundation Grants: 1320472, 1302336, and 1555332.



Abstract

This report provides the world's first comprehensive study of indoor channels at 28 GHz and 73 GHz using different antenna polarizations and combined polarizations to generate large-scale path loss models and time delay spreads for the development of 5G standards at 28 GHz and 73 GHz. Directional and omnidirectional path loss models and directional multipath RMS delay spread values are presented, yielding insight into mmWave indoor office propagation characteristics. The results show that novel large-scale path loss models provided here are simpler and more physically-based compared to previous 3GPP and ITU indoor propagation models that require more model parameters, yet offer very little additional accuracy and lack physical basis. The closed-form expressions that optimize existing and newly proposed large-scale path loss models are given in Appendix A, the raw omnidirectional data used to create the large-scale path loss models in this report are tabulated in Appendix B, and standard deviations of each large-scale path loss model are tabulated for side-by-side comparison in Appendix C. The technical report describes the extensive ultra-wideband millimeter-wave indoor propagation measurement campaign conducted at 28 GHz and 73 GHz by the NYU WIRELESS research team during the summer of 2014. The measurements were sponsored by the NYU WIRELESS Industrial Affiliates Program and the National Science Foundation.

Measurements were performed using two similar 400 Mega-chips-per-second sliding correlator channel sounder systems with mechanically-steerable, highly-directional 15 dBi (at 28 GHz) and 20 dBi (at 73 GHz) horn antennas at both the transmitter and receiver, with the transmitter antennas always vertically polarized and the receiver antennas vertically and horizontally polarized to measure co- and cross-polarized channel characteristics. The indoor measurements were conducted in a typical office environment on the 9th floor of 2 MetroTech Center, Brooklyn, NY. Transmit antennas were set at a height of 2.5 meters near the ceiling (typical indoor wireless access point heights), and receiver antennas were placed at heights of 1.5 meters (typical handset heights), to emulate a typical WLAN environment. Five transmitter (TX) locations and 33 receiver (RX) locations were chosen and a total of 48 TX-RX location combinations were measured (identical locations at both frequencies) in a typical office environment to investigate the complex indoor propagation channel. The measurement environment was a closed-plan in-building scenario that included line-of-sight and non-line-of-sight corridor, hallway, cubicle-farm, and adjacent-room communication links. A corridor environment is when a propagating signal travels down a corridor to reach the receiver by a line-of-sight path, reflections, and/or diffraction, but not penetration. An cubicle-farm environment includes a large layout and a central TX location, where the propagating signal reaches the receiver by a line-of-sight path, reflections, and/or diffraction, but not penetration. A closed-plan environment is when a propagating signal penetrates an obstruction to reach the receiver in addition to potential reflections, and/or diffraction. All measurement environment scenarios are included as part of the closed-plan environment, and the models in this report are for closed-plan and thus include all locations measured (both line-of-sight and non-line-of-sight).

Power delay profiles were acquired at unique antenna pointing angles for each TX-RX location combination for distances that ranged from 3.9 m to 45.9 m for both frequencies, with -6.5 dBm to 24 dBm of transmit power at 28 GHz and -7.9 dBm to 12.3 dBm of transmit power at 73 GHz. Six angle of arrival (AOA) antenna sweeps and two angle of departure (AOD) antenna sweeps were conducted in the azimuth plane at fixed elevation planes for each TX and RX location combination using highly-directional and steerable horn antennas for vertical-to-vertical (V-V) antenna polarizations. Six identical AOA and two identical AOD antenna

sweeps were also performed for vertical-to-horizontal (V-H) antenna polarizations, resulting in 16 overall measurement sweeps for each TX-RX location combination.

The chapters in this report provide a literature review of previous measurements and present the measurement hardware, measurement environments, measurement procedures, and measurement results of the 28 GHz and 73 GHz campaign, including directional (unique pointing angle) and omnidirectional path loss models, and time dispersion properties. Single frequency and multi-frequency path loss models are introduced, with the closed-form expressions for optimization provided in Appendix A. Path loss models are given for both separate and combined polarization scenarios. The comparative analysis of path loss models shows the value of including a free space path loss leveraging point based on actual physics, that provides better predictability and stability than models that do not include a reference distance. Appendix B includes a listing of the raw omnidirectional path loss data used to calculate the models presented in this report, and Appendix C provides a side-by-side comparison of the standard deviations of each model. The time dispersion characteristics such as RMS delay spread are provided for arbitrary antenna pointing angles and for the strongest receive power antenna pointing angle combinations.

The models and characteristics will be helpful for mmWave radio-system design and system-wide simulations, in order to estimate network capacity and overall data throughput in indoor office environments at the 28 GHz and 73 GHz mmWave frequency bands.

Contents

Contents	vii
List of Figures	ix
List of Tables	xi
1 Introduction	1
1.1 Millimeter-Wave Communications Background and Motivation	1
1.2 Project Overview	1
1.3 Report Overview	2
2 Literature Review	5
2.1 Below 6 GHz	5
2.2 Above 6 GHz	7
2.3 Recent Activities for Indoor MmWave Studies	10
3 Measurement Descriptions	11
3.1 Locations and Environments	11
3.1.1 MTC1 and corresponding RX locations	13
3.1.2 MTC2 and corresponding RX locations	15
3.1.3 MTC3 and corresponding RX locations	17
3.1.4 MTC4 and corresponding RX locations	18
3.1.5 MTC5 and corresponding RX locations	20
3.2 System Descriptions	22
3.2.1 Transmitter Hardware	22
3.2.2 Receiver Hardware	22
3.3 Measurement Procedure	24
4 Large-Scale Path Loss Models	29
4.1 Single Frequency Path Loss Models	29
4.2 Multi-Frequency Path Loss Models	30
5 Path Loss Model Parameters and Analysis	33
5.1 Directional Path Loss Models for Co- and Cross-Polarized Antennas	33
5.2 Omnidirectional Path Loss Models for Co- and Cross-polarized Antennas	38
5.3 Directional Path Loss Models for Combined Polarizations	43
5.4 Omnidirectional Path Loss Models for Combined Polarizations	44

6	Time Dispersion Properties	49
6.1	MmWave Indoor Time Dispersion Properties	49
6.1.1	Multipath Time Dispersion Statistics for Co- or Cross-Polarized Antennas	49
6.1.2	Multipath Time Dispersion Statistics for Combined-Polarized Antennas	52
7	Conclusion	55
A	Path Loss Model Parameter Closed-Form Expressions	59
A.1	CI Path Loss Model	59
A.2	CIX Path Loss Model	60
A.3	CIF Path Loss Model	61
A.4	CIFX Path Loss Model	63
A.5	FI Path Loss Model	64
A.6	ABG Path Loss Model	65
A.7	ABGX Path Loss Model	66
B	Omnidirectional Path Loss Values	69
C	Path Loss Model Standard Deviations Side-by-Side	75

List of Figures

3.1	Map of the 2 MetroTech Center 9th floor with five TX locations and 33 RX locations. The yellow stars represent the TX locations, and the red dots represent the RX locations.	12
3.2	View of the open office area for the MTC1 TX location on the 9th floor of 2 MetroTech Center. Partition panels and furniture occupy a majority of the working area and can be categorized as office partitions.	14
3.3	Map displaying the MTC1 TX location and RX1-RX9 locations. The yellow star indicates the MTC1 TX location, the open red circles indicate LOS RX locations, and solid blue squares indicate NLOS RX locations. The nine RX locations were chosen around the TX and the area between each TX-RX location combination includes various office partitions and walls. The black arrows originating from the TX location indicate the initial TX antenna azimuth pointing angles for a particular RX location. All measured azimuth angles are identified with respect to the compass in the upper right corner of the figure, where the positively increasing direction is clockwise. The initial TX and RX antenna azimuth and elevation pointing angles are provided in Table 3.2	14
3.4	View of the lobby area outside of two classrooms at the end of a long corridor for the MTC2 TX location.	15
3.5	Map displaying the MTC2 TX location, RX10 to RX22, and RX161 locations. The yellow star indicates the MTC1 TX location, the open red circles indicate LOS RX locations, and solid blue squares indicate NLOS RX locations. The 14 RX locations were chosen around the TX and the area between each TX-RX link combination includes various obstructions and partitions such as drywall, elevators, glass doors, and metal doors. RX16 and RX161 are at the same location, but with the NYU WIRELESS front entrance glass door closed for RX16, and open for RX161. The black arrows originating from the TX location indicate the initial TX azimuth boresight angles for a particular RX location. All measured azimuth angles are identified with respect to the compass in the upper right corner of the figure, where the positively increasing direction is clockwise. The initial TX and RX antenna azimuth and elevation pointing angles are provided in Table 3.3.	16
3.6	View of the open room area with partition panels and office furniture obstructions near the MTC3 TX location.	17
3.7	Map displaying the MTC3 TX location, RX16, RX17, and RX23-RX27 locations. The yellow star indicates the MTC3 TX location, the open red circle indicates the LOS RX location, and the solid blue squares indicate the NLOS RX locations. The seven RX locations were chosen around the TX and are behind various combinations of walls, glass doors, and metal doors. The black arrows originating from the TX location indicate the initial TX antenna azimuth pointing angles for a particular RX location. All measured azimuth angles were identified with respect to the compass in the upper right corner of the map, where the positively increasing direction is clockwise. The initial TX and RX antenna azimuth and elevation pointing angles are provided in Table 3.4.	18
3.8	View of the long corridor where the MTC4 TX was placed outside of the elevator partition entrance.	19

3.9 Map showing the MTC4 location and corresponding RX11-RX16, RX18, RX28, RX121, and RX161 locations. The yellow star indicates the MTC4 TX location, the open red circles indicate the four LOS RX locations, and the solid blue squares indicate the six NLOS RX locations. The black arrows originating from the TX location indicate the initial TX antenna azimuth pointing angles for a particular RX location. All azimuth angles in the measurements were with respect to the compass in the upper right corner of the map, where the positively increasing direction is clockwise. The initial TX and RX antenna azimuth and elevation pointing angles are provided in Table 3.5. 19

3.10 View of the inside of the classroom where the MTC5 TX location was placed, surrounded by desks and chairs. 20

3.11 Map displaying the MTC5 TX location, and RX8, RX19, and RX28-RX33 locations. The yellow star indicates the MTC5 TX location and the solid blue squares indicate the eight NLOS RX locations. The black arrows originating from the TX location indicate the initial TX antenna azimuth pointing angles for a particular RX location. All azimuth angles in the measurements were with respect to the compass in the upper right corner of this figure, where the positively increasing direction is clockwise. The initial TX and RX antenna azimuth and elevation pointing angles are provided in Table 3.6. 21

3.12 Block diagram of the 28 GHz transmitter. The TX PN generator produced a 400 Mcps PN sequence that was modulated by a 5.4 GHz IF and then multiplied by a 22.6 GHz LO, thus upconverted to a 28 GHz centered RF signal. The RF signal was then transmitted through a highly-directional horn antenna with 15 dBi of gain and 28.8° azimuth HPBW. 22

3.13 Block diagram of the 73 GHz transmitter. The TX PN generator produced a 400 Mcps PN sequence that was modulated by a 5.625 GHz IF and then multiplied by a 67.875 GHz (tripled 22.625 GHz) LO, thus upconverted to a 73.5 GHz centered RF signal. The RF signal was then transmitted through a highly-directional horn antenna with 20 dBi of gain and 15° azimuth HPBW. 23

3.14 Block diagram of the RX system used to characterize the 28 GHz indoor channel. The received signal was downconverted from the 28 GHz centered RF signal via an LO of 22.6 GHz, which was then subsequently demodulated down to its *I* and *Q* baseband components via an IF-stage 5.4 GHz LO. A PN sequence identical to that at the TX was generated, but at a slightly slower rate of 399.95 Mcps, and was then mixed with the received signal’s baseband *I* and *Q* signals, that were used to recover a time-dilated impulse response of the channel. 24

3.15 Block diagram of the RX system used to characterize the 73 GHz indoor channel. The received signal was downconverted from the 73.5 GHz centered RF signal via an LO of 67.875 GHz, which was then subsequently demodulated down to its *I* and *Q* baseband components via an IF-stage 5.625 GHz LO. A PN sequence identical to that at the TX was generated, but at a slightly slower rate of 399.95 Mcps, and was then mixed with the received signal’s baseband *I* and *Q* signals, that were used to recover a time-dilated impulse response of the channel. . . 25

List of Tables

3.1	TX and corresponding RX locations measured for the 28 GHz and 73 GHz indoor propagation measurements referenced to Fig. 3.1. 3D T-R separation distance ranges are provided for each TX and corresponding RX locations, as well as RX locations that experienced outage (e.g. no detectable signal for all pointing angles) for V-V or V-H antenna polarization configurations. A “-” indicates no outage and the RX ID number indicates where an outage occurred.	12
3.2	TX and RX location IDs, T-R separation distances, initial TX and RX antenna azimuth and elevation pointing angles for each TX-RX location combination, and environment types for the co- and cross-polarization antenna configuration measurements for the MTC1 TX location. All angle configurations are the same for both 28 GHz and 73 GHz measurements for RX2-RX9. However, the RX1 initial angle configurations were different for the 28 GHz and 73 GHz measurements, as specified in the table.	15
3.3	TX and RX location IDs, T-R separation distances, initial TX and RX antenna azimuth and elevation pointing angles for each TX-RX location combination, and environment types for the co- and cross-polarization antenna configuration measurements for the MTC2 TX location. All angle configurations are identical for the 28 GHz and 73 GHz measurements.	16
3.4	TX and RX location IDs, T-R separation distances, initial TX and RX antenna azimuth and elevation pointing angles for each TX-RX location combination, and environment types for the co- and cross-polarization antenna configuration measurements for the MTC3 TX location. All angle configurations are identical for the 28 GHz and 73 GHz measurements.	17
3.5	TX and RX location IDs, T-R separation distances, initial TX and RX antenna azimuth and elevation pointing angles for each TX-RX location combination, and environment types for the co- and cross-polarization antenna configuration measurements for the MTC4 TX location. All angle configurations are identical for the 28 GHz and 73 GHz measurements.	20
3.6	TX and RX location IDs, T-R separation distances, initial TX and RX antenna azimuth and elevation pointing angles for the each TX-RX location combination, and environment types for the co- and cross-polarization antenna configuration measurements for the MTC5 TX location. All angle configurations are identical for the 28 GHz and 73 GHz measurements.	21
3.7	Broadband sliding correlator channel sounding system specifications for the 28 GHz and 73 GHz indoor measurement campaign [6, 97–100].	23
3.8	The measurement routine for each TX and RX location combination. Elevation angles are with respect to boresight (initial) angles, which can be found in Tables 3.2 – 3.6. HPBW indicates the step increment in the azimuth plane (tilt change in the elevation plane), where the antenna azimuth HPBW for the 28 GHz measurements was 28.8° , but the step increment was 30° . As previously described the HPBW step increment for the 73 GHz measurements was 15°	27
5.1	Path loss environment definitions for directional path loss models.	33

5.2	Single frequency directional CI path loss model (4.1) parameters with $d_0 = 1$ m for 28 GHz and 73 GHz indoor channels with TX heights of 2.5 m and RX heights of 1.5 m for V-V and V-H antenna polarization configurations. The 28 GHz TX and RX antennas had 15 dBi (28.8° azimuth HPBW) of gain and the 73 GHz TX and RX antennas had 20 dBi (15° azimuth HPBW) of gain. “Freq.” stands for carrier frequency and “Pol.” stands for TX-RX antenna polarization configuration. The LOS distances ranged from 4.6 m to 21.3 m and the NLOS distances ranged from 3.9 m to 45.9 m.	35
5.3	Single frequency directional CIX path loss model (4.2) parameters with $d_0 = 1$ m for 28 GHz and 73 GHz indoor channels with TX heights of 2.5 m and RX heights of 1.5 m for V-H antenna polarization configurations. The 28 GHz TX and RX antennas had 15 dBi (28.8° azimuth HPBW) of gain and the 73 GHz TX and RX antennas had 20 dBi (15° azimuth HPBW) of gain. “Freq.” stands for carrier frequency and “Pol.” stands for TX-RX antenna polarization configuration.	35
5.4	Single frequency directional FI path loss model (4.3) parameters for 28 GHz and 73 GHz indoor channels with TX heights of 2.5 m and RX heights of 1.5 m for both V-V and V-H antenna polarization configurations. The 28 GHz TX-RX antennas had 15 dBi (28.8° azimuth HPBW) of gain and the 73 GHz TX-RX antennas had 20 dBi (15° azimuth HPBW) of gain. “Ant. Pol.” stands for antenna polarization.	35
5.5	28 GHz and 73 GHz multi-frequency directional path loss model parameters for the CI, CIX, CIF, CIFX, ABG, and ABGX models for LOS, NLOS, and NLOS-Best environments and scenarios. The CIX, CIFX, and ABGX cross-polarized models use the corresponding parameters found for their respective co-polarized models to find the XPD factor in dB that minimizes σ . “Pol.” stands for polarization configuration (either V-V or V-H).	36
5.6	Path loss definitions for omnidirectional path loss models.	39
5.7	Single frequency omnidirectional CI path loss model parameters with $d_0 = 1$ m and FI path loss model parameters for 28 GHz and 73 GHz indoor propagation channels with TX heights of 2.5 m and RX heights of 1.5 m for both V-V and V-H antenna polarization configurations for LOS and NLOS environments. “Freq.” stands for carrier frequency, “Pol.” stands for TX-RX antenna polarization configuration, and “Env.” stands environment.	41
5.8	Single frequency omnidirectional CIX path loss model parameters with $d_0 = 1$ m for 28 GHz and 73 GHz indoor channels with TX heights of 2.5 m and RX heights of 1.5 m for V-H antenna polarization configurations. The 28 GHz TX and RX antennas had 15 dBi (28.8° azimuth HPBW) of gain and the 73 GHz TX and RX antennas had 20 dBi (15° azimuth HPBW) of gain. “Freq.” stands for carrier frequency and “Pol.” stands for TX-RX antenna polarization configuration	41
5.9	28 GHz and 73 GHz multi-frequency omnidirectional path loss model parameters for the CI, CIX, CIF, CIFX, ABG, and ABGX models for LOS and NLOS environments. The CIX, CIFX, and ABGX cross-polarized models use the corresponding parameters found for their respective co-polarized models to find the XPD factor in dB that minimizes σ . “Pol.” stands for polarization configuration (either V-V or V-H).	41
5.10	Single frequency combined polarization directional path loss models at 28 GHz and 73 GHz for LOS, NLOS, and NLOS-Best scenarios.	43
5.11	28 GHz and 73 GHz multi-frequency combined polarization directional path loss models for LOS, NLOS, and NLOS-Best scenarios.	45
5.12	28 GHz and 73 GHz single frequency combined polarization CI and FI omnidirectional path loss models for LOS and NLOS environments.	45
5.13	28 GHz and 73 GHz multi-frequency combined polarization CI, CIF, and ABG omnidirectional path loss models for LOS and NLOS environments.	46

6.1	Comparison of mean, standard deviation, and maximum RMS delay spreads at 28 GHz and 73 GHz for V-V and V-H antenna polarization combinations in LOS and NLOS indoor propagation environments. “Ant. Pol.” means TX-RX antenna polarization and “Env.” indicates the environment type of the RX locations.	53
6.2	Comparison of mean, standard deviation, and maximum RMS delay spreads at 28 GHz and 73 GHz for combined antenna polarizations in LOS and NLOS indoor propagation environments. “Env.” indicates the environment type of the RX locations.	53
B.1	28 GHz co-polarized antenna (V-V) omnidirectional path loss values with corresponding Environment (Env.) TX IDs, RX IDs, path loss (PL) in dB, and 3D T-R separation distance in meters.	70
B.2	28 GHz cross-polarized antenna (V-H) omnidirectional path loss values with corresponding Environment (Env.) TX IDs, RX IDs, path loss (PL) in dB, and 3D T-R separation distance in meters.	71
B.3	73 GHz co-polarized antenna (V-V) omnidirectional path loss values with corresponding Environment (Env.) TX IDs, RX IDs, path loss (PL) in dB, and 3D T-R separation distance in meters.	72
B.4	73 GHz cross-polarized antenna (V-H) omnidirectional path loss values with corresponding Environment (Env.) TX IDs, RX IDs, path loss (PL) in dB, and 3D T-R separation distance in meters.	73
C.1	Single frequency directional path loss model standard deviations for the CI model with $d_0 = 1$ m, the CIX model, and the FI path loss model. “Freq.” stands for carrier frequency, “Pol.” stands for TX-RX antenna polarization configuration, “Env.” stands for environment, and “Comb.” stands for combined polarization. Differences in standard deviations are also shown.	75
C.2	Multi-frequency directional path loss model standard deviations for the CI, CIX, CIF, CIFX, ABG, and ABGX large-scale path loss models. “Pol.” stands for TX-RX antenna polarization configuration, “Env.” stands for environment, and “Comb.” stands for combined polarization. Differences in standard deviations are also shown.	76
C.3	Single frequency omnidirectional path loss model standard deviations for the CI model with $d_0 = 1$ m, the CIX model, and the FI path loss model. “Freq.” stands for carrier frequency, “Pol.” stands for TX-RX antenna polarization configuration, “Env.” stands for environment, and “Comb.” stands for combined polarization. Differences in standard deviations are also shown.	76
C.4	Multi-frequency omnidirectional path loss model standard deviations for the CI, CIX, CIF, CIFX, ABG, and ABGX large-scale path loss models. “Pol.” stands for TX-RX antenna polarization configuration, “Env.” stands for environment, and “Comb.” stands for combined polarization. Differences in standard deviations are also shown.	77

This page is intentionally left blank.

Chapter 1

Introduction

1.1 Millimeter-Wave Communications Background and Motivation

Over the past few years there has been an explosion in mobile data traffic as a consequence of the growth of smartphones, tablets, and devices that provide, monitor, transfer, and record ZettaBytes of data every year [1–3]. Smartphone adoption rates are sharply increasing as carriers and service providers attempt to attract more customers [4, 5]. The advent of smartphones and “Wireless Fidelity” (WiFi) enabled devices has facilitated the surge in wireless technologies and applications, but has created congestion in the sub-6 GHz spectrum in which a majority of these devices operate in [6–9].

The 2.4 GHz and 5 GHz WiFi bands have been widely used for indoor wireless communications in typical office environments, restaurants, and hotels since the early 2000’s [10, 11], but dense deployment of indoor hotspots and new wireless multimedia devices has led to increased congestion and traffic over indoor networks [12]. Offices are “cutting the cord,” by investing in numerous wireless multimedia devices for video. In addition to the 2.4 GHz and 5 GHz WiFi bands, the 60 GHz millimeter-wave (mmWave) band is used for WiGig to support high-data-rate applications. The vast available bandwidth (57-64 GHz) at 60 GHz (and unlicensed availability in the U.S. and other countries) motivated extensive 60 GHz indoor propagation measurements to understand channel characteristics necessary for designing indoor wireless local area network (WLAN) systems capable of achieving multi-gigabits-per-second throughputs [13, 14]. The study of mmWave propagation has been widely conducted at 60 GHz (with fewer studies at other mmWave bands) for common indoor environments in order to properly model path loss and channel characteristics.

The impending spectrum and capacity crunch for outdoor cellular may very well lead to the use of the 28 GHz and 73 GHz mmWave frequency bands as an extension for 5G outdoor and indoor communications, especially due to the trend of shrinking cell sizes. If the 28 GHz and 73 GHz bands are to eventually become unlicensed similar to the 60 GHz band, the wide range of applications and events they could support would tremendously reduce the load on the cellular and backhaul networks as we move into the age of Internet of Things (IoT) [15]. In any case, extensive indoor propagation measurements at the 28 GHz and 73 GHz bands are needed in order to accurately characterize and model the channel to design capable indoor systems at these frequencies.

1.2 Project Overview

The NYU WIRELESS research center conducted extensive measurements at 28 GHz and 73 GHz with various transmitter (TX) and receiver (RX) antenna azimuth and elevation pointing angle combinations and

for different antenna polarization configurations in the summer of 2014 in a typical office building. Over 70 GB of raw data were collected and are the basis for the models and characteristics presented in this report.

The measurements were conducted on the 9th floor of 2 MetroTech Center (MTC) in Downtown Brooklyn, New York. The single floor office environment (35 meters \times 65.5 meters) consisted of typical office partitions and furniture (such as cubicles, desks, chairs, metal shelves, wood closets, concrete walls, glass doors, and elevator doors). A 400 Megachips-per-second (Mcps) sliding correlator channel sounding system and two pairs of steerable directional horn antennas were used to measure co- and cross-polarization channel characteristics at the 28 GHz and 73 GHz frequency bands. A pair of 15 dBi gain horn antennas with 28.8° half-power beamwidth (HPBW) in the azimuth plane and a pair of 20 dBi gain horn antennas with 15° HPBW in the azimuth plane were used at the TX and RX when performing measurements at 28 GHz and 73 GHz, respectively. Five TX locations and 33 RX locations with 48 overall TX-RX location combinations and with transmitter-receiver (T-R) separation distances ranging from 3.9 meters (m) to 45.9 m were chosen in order to investigate the complex indoor propagation channels. The TX antennas were set at heights of 2.5 m (near the ceiling) above ground level (AGL) to emulate indoor wireless access points, and the RX antennas were fixed at heights of 1.5 m AGL (similar to the height of a mobile phone carried by a human). For each measured TX-RX location combination, 16 different unique pointing angle measurement sweeps were performed to investigate angle of departure (AOD) and angle of arrival (AOA) statistics, and a power delay profile (PDP) was acquired at each unique azimuth and elevation antenna pointing angle, separated by step increments of 15° or 30° in the azimuth plane for the 28 GHz and 73 GHz frequencies, respectively. The measurements included two antenna polarization combinations: vertical-to-vertical (V-V), where the TX and RX antennas were vertically polarized (perpendicular to the ground), and vertical-to-horizontal (V-H), where the TX antenna was vertically polarized and the RX antenna was horizontally polarized, in order to study the impact of polarization for indoor mmWave communications systems at 28 GHz and 73 GHz.

1.3 Report Overview

The following sections of the report discuss details from numerous indoor propagation campaigns below 6 GHz and above 6 GHz in the mmWave frequency bands including measurement hardware, environments, configurations, and results. The specifications regarding the 28 GHz and 73 GHz measurement equipment that was used to measure the indoor channel at NYU are also described, in addition to the measurement procedures, settings, and scenarios for all 48 TX-RX location combinations conducted at each band. Traditional single frequency path loss models such as the close-in free space reference distance (CI) and *alpha-beta* floating-intercept (FI) models are discussed, in addition to multi-frequency path loss models such as the *alpha-beta-gamma* (ABG) model and a new close-in free space reference distance with frequency weighting factor (CIF) model. Furthermore, cross-polarized versions of each path loss model, that includes a cross-polarization discrimination (XDP) factor are introduced. The closed-form expressions for optimizing model parameters are provided in Appendix A. After introducing the models, the report gives the estimated directional and omnidirectional path loss model parameters for separate and combined polarizations for single and multi-frequency path loss models from line-of-sight (LOS) and non-line-of-sight (NLOS) measurement data. Multipath time dispersive characteristics from the directional measurements are then provided for the best and worst cases (smallest and largest delay spreads), and for the unique pointing angles that resulted in the lowest path loss between the TX and RX for each location combination. Time dispersive characteristics are given for both separate and combined polarization scenarios.

In Appendix B a compilation of the post-processed omnidirectional path loss data at 28 GHz and 73 GHz is provided so that researchers may generate their own omnidirectional path loss models and perform analyses from the measurement data. As previously mentioned, the closed-form expressions that optimize the parameters for each model are given in Appendix A.

This page is intentionally left blank.

Chapter 2

Literature Review

This chapter presents an extensive literature review on previous indoor propagation studies that have focused on wireless channel characterization for the creation of statistical models, vital to the development of new standards and technologies for wireless communications systems. The current WiFi and 4G standards were developed based on propagation measurements that assisted in accurately characterizing the temporal and spatial indoor propagation channel below 6 GHz frequencies. A literature review of channel measurements and models is presented for frequencies below 6 GHz and above 6 GHz (mainly focused on 60 GHz) for various indoor scenarios.

2.1 Below 6 GHz

Extensive studies for indoor wireless propagation and channel models below 6 GHz have been conducted for many years. As just a sample of typical work in an indoor office environment, a 900 MHz signal with 200 kHz of bandwidth experienced between 28 and 61 dB of attenuation per decade of distance for distances up to 27 m, across multiple floors [16]. Ericsson used a path loss model from multi-floor measurements of an office building that had four breakpoints, but assumed 30 dB of attenuation at $d_0 = 1$ m (free space for first meter) at 900 MHz and measured a PLE of 2 for up to 10 m, and used a multiple slope model at greater distances [17]. Indoor multipath propagation measurements were performed by Saleh and Valenzuela with a 10 ns probing pulse centered at 1.5 GHz with vertically polarized discone TX and RX antennas at 2 meter (m) heights [18]. The indoor channel was observed to vary slowly with time, resulting in maximum RMS delay spreads of 50 ns in adjacent rooms, and signal attenuation between 30 dB and 40 dB per decade of distance.

Bultitude measured the 910 MHz band in an indoor office-style building with a CW (continuous wave) tone transmitted at 500 mW with an omnidirectional TX antenna, and a quarter-wave monopole RX antenna [19]. Results indicated that in line-of-sight (LOS) environments, signal attenuation over distance closely followed Friis' free space path loss equation where propagating signals attenuate following the square power law. In some cases, the received power was greater than predicted free space propagation, indicating a waveguide effect in narrow hallways of the office building.

In the late 1980's, Motley and Keenan performed indoor multi-floor measurements and found PLEs of 4 and 3.5 relative to a 1 m free space reference distance at 900 MHz and 1700 MHz, respectively, using TX and RX dipole antennas [20]. Rappaport *et al.* conducted wideband multipath measurements at 1300 MHz in factory buildings with a 10 nanosecond (ns) transmitting pulse in both LOS and NLOS environments with

TX and RX discone antennas that resulted in path loss attenuation of 22 dB per decade of distance and an RMS delay spread that ranged from 30 ns to 300 ns [21].

In the early 1990's, Rappaport *et al.* performed indoor measurements at 1.3 GHz and 4.0 GHz for both circularly and linearly polarized antennas. Results indicated similar propagation path loss for both frequencies, and larger cross-polarization discrimination was found in LOS channels compared to NLOS or obstructed channels [22–24]. Additionally, the use of an omnidirectional TX antenna and a directional circularly-polarized RX antenna provided the lowest RMS delay spread and the lowest maximum excess delay (10 dB down) compared to various polarizations of omnidirectional and directional antennas.

A paper on indoor propagation by J. B. Andersen *et al.* in 1995 highlighted the value of using a 1 m close-in free space reference distance for meaningful indoor path loss models [25]. The paper also demonstrated the viability of ray-tracing for indoor channel impulse response prediction for single and multi-floor propagation. Single story retail and grocery stores had PLEs of 2.2 and 1.8 at 914 MHz, respectively, with respect to (w.r.t.) a 1 m reference distance. Indoor offices with soft partitions measured at 900 and 1900 MHz had PLEs w.r.t. a 1 m reference distance of 2.4 and 2.6, respectively, with standard deviations between 9.6 dB and 14.1 dB. Radio-frequency penetration was also reported to attenuate between 3 dB and 30 dB for metallic tinted windows. Rappaport and Sandhu published a survey paper in 1994 that summarized radio-propagation measurements for frequencies between 850 MHz and 4000 MHz and the problems of radio-wave propagation into buildings for wireless communications systems [26]. Average floor attenuation factors were found to be 24.4 dB and 31.6 dB at 914 MHz for a transmitter and receiver separated by 3 floors in two different office buildings.

Alvarez *et al.* studied the indoor radio channel between 1 GHz and 9 GHz, and defined four scenarios: LOS (when there was a direct path between the TX and RX), Soft-NLOS (when there was no direct path, but rather reflected paths between the TX and RX), Hard-NLOS (when there was no direct or reflected path between the TX and RX), and corridor (special case for LOS, when there was a direct path and many strong reflected paths between the TX and RX) [27]. A VNA channel sounder with omnidirectional TX and RX antennas was used to record the channel transfer function by concatenating frequency sweeps between 1 and 5 GHz and 5 and 9 GHz. The estimated PLEs from the measurement data were 1.4 ($d_0 = 15.1$ cm) for the LOS scenario, 3.2 ($d_0 = 8.2$ cm) for Soft-NLOS, and 4.1 ($d_0 = 6.7$ cm) for Hard-NLOS.

Ghassemzadeh *et al.* used a Vector Network Analyzer (VNA) to transmit an ultra-wideband 1250 MHz radio-frequency (RF) bandwidth signal centered at 5 GHz with a conical monopole omnidirectional TX and RX antenna inside 23 homes in northern and central New Jersey [28]. In LOS environments the close-in free space reference distance path loss model relative to a 1 m free space path loss (FSPL) distance resulted in a PLE of 1.7, and was determined to be 3.1 in NLOS environments. The standard deviation or shadow factor about the mean path loss lines ranged from 2.8 dB to 4.4 dB, indicating small large-scale signal fluctuations in the indoor home environments for ultra-wideband propagation at 5 GHz.

In the late 1990's Durgin *et al.* performed numerous CW indoor and outdoor-to-indoor measurements between walls and other partitions to derive path loss models in residential areas at 5.85 GHz [29–32]. The propagation models developed from the measurements were helpful for outdoor-to-indoor deployments, as the main results indicated that signals that penetrated homes attenuated on average by about 14 dB, with tree shadowing attenuation that varied from 11 dB to 16 dB. Close-in building shadowing also attenuated the propagating signals by 15 dB to 21 dB, depending on RX antenna heights.

Durgin *et al.* studied angle delay and dispersion characteristics for outdoor and indoor peer-to-peer channels centered at 1920 MHz in the early 2000's. Both omnidirectional and directional (30° half-power beamwidth (HPBW)) antennas were used to measure angles of arrival and delay spread statistics. Typical results for outdoor cross-campus measurements resulted in 17 ns to 219 ns RMS delay spreads, whereas three indoor-to-indoor locations resulted in 27 ns to 34 ns RMS delay spreads and 0.73-0.90 angular spreads [33, 34].

Patawari *et al.* also studied peer-to-peer propagation, but at 1.8 GHz with low antenna heights and with 200 MHz of first null-to-null RF bandwidth, with measured RMS delay spreads up to 330 ns in rural areas and up to 200 ns in urban peer-to-peer environments [35].

Ray-tracing simulations are another popular method for modeling indoor and outdoor propagation channels, and are less time-intensive and less costly compared to actual measurements. Motorola demonstrated the viability of ray-tracing for its revolutionary 18 GHz Altair WLAN product in the early 1990's [36]. The University of Bristol and Virginia Tech were two of the first institutions to demonstrate the promise of ray-tracing for small-cell and indoor deployments [37]. Schaubach *et al.* used geometric optics to estimate average path loss and delay spread in microcellular environments by building database environments and writing a computer program to perform ray-tracing on the databases. Simulations compared with time-delay measurements at 914 MHz on the Virginia Tech campus validated the program and methodology [38].

Work by Seidel *et al.* in the 1990's showed good agreement for path loss and delay spread characteristics using predictive ray-tracing techniques and measurements at 1.3 GHz and 4.0 GHz. The predicted and measured path loss differed by less than 6 dB over most locations and RMS delay spreads were within 20 ns for each measured location in rooms with 4.5 m ceiling heights [39, 40]. Additional ray-tracing simulations using 3D building databases and transmitted, reflected, and scattered ray mechanisms successfully predicted propagation at 1900 MHz using a spread spectrum system [41]. An indoor ray-tracing software developed in the 1990's was able to predict path loss, partition loss, and floor attenuation loss for indoor environments at various sub-6 GHz frequencies by taking advantage of attenuation models based on the types of partitions, frequency, and distance [42, 43]. Improved ray-tracers for indoor wireless propagation included 3D ray-launching methods by using geodesic spheres and distributed wavefronts to increase accuracy and prediction at 900 MHz [44].

A measurement-based statistical indoor radio-channel impulse response model (SIRCIM) and statistical outdoor simulator (SMRCIM) were successfully implemented from many thousands of collected channel impulse responses (CIRs) in factories at 1.3 GHz [45, 46], and from outdoor cellular channel PDPs [47, 48]. These CIR models were popular with industry in the 1990's during the early years of digital cellular and WiFi [49]. The SIRCIM and SMRCIM models were based on statistical and geometrical models to synthesize the phases and directions of arrival and departure in an IR model [49, 50].

2.2 Above 6 GHz

Many studies at mmWave bands for the indoor environment have been conducted, predominantly in the 60 GHz band, one of the most promising candidates for multi-gigabit wireless indoor communications systems. The large swath of available spectrum in the unlicensed 57-66 GHz band (60 GHz band) represents one of the largest unlicensed areas of spectrum real-estate to achieve ultra-high data rates for multi-Gbps wireless communications performance, spectrum flexibility, and capacity [51, 52]. While the 60 GHz spectrum has a large amount of bandwidth to offer, oxygen attenuation is more severe than other mmWave bands [53]. Yong *et al.* presented an overview of 60 GHz technologies and their potential to provide next generation multi-gigabit wireless communications, along with a series of technical challenges to resolve before large-scale deployments [54]. Today, higher transmit power is allowed at 60 GHz compared to other existing wireless local area networks (WLANs) and wireless personal area network (WPANs) systems. While high path loss in the first meter of propagation and transmission loss at 60 GHz may limit the operation to one room, interference is reduced compared to the severe interference experienced in the congested 2-2.5 GHz and 5-5.8 GHz bands. Additionally, the form factor of mmWave systems and antennas will be smaller, compared to sub-6 GHz systems, making it convenient highly-directional steerable antenna arrays to be integrated into electronic products [55–57]. A number of open issues and technical challenges have yet to be fully

addressed at 60 GHz, and they can be generally classified into the following categories: channel propagation, antenna technologies, RF solutions, and modulation schemes [54, 58–61]. Next-generation WLANs will also exploit 60 GHz spectrum with the development of the IEEE 802.11ad and WiGig standards, supported by WiFi companies who recognized that current spectral resources are insufficient for next-generation applications [51, 53]. Researchers in Japan conducted pioneering research in the 1990’s in the 60 GHz band, and developed point-to-point base-stations and user-stations with mmWave monolithic microwave integrated circuit (MMIC) devices with antennas the size of a quarter that could transmit as high as 156 Mbps for wireless local area networks (WLANs) [62, 63]. In a recent indoor experiment down a narrow hallway, researchers were able to transmit 7.5 Gbps at a distance of 15 m using a high gain Antipodal Linear Tapered Slot Antenna (AL TSA) at 60 GHz [64], with additional studies resulting in path loss exponents slightly above free space ($n = 2$) in LOS [65]. Researchers in India also focused on mmWave antenna design at 60 GHz with relatively high gains and small form factors for gigabit wireless communications and applications [66].

There have been extensive channel measurements and modeling efforts for indoor and outdoor scenarios at 60 GHz, but this report focuses on indoor environments. Some of the earliest mmWave indoor channel modeling work happened in Europe and Japan. Smulders *et al.* performed frequency-domain measurements across 2 GHz of bandwidth centered at 58 GHz in an indoor environment and employed biconical horn antennas with omnidirectional radiation patterns at the TX and RX [67–69]. The wideband mmWave measurements yielded RMS delay spreads between 15 ns and 45 ns in small rooms and between 30 ns and 70 ns in larger rooms indicating that more paths with considerable energy arrive at the receiver over a larger time delay in larger rooms. A worst case RMS delay spread of 100 ns was also reported.

Xu *et al.* studied the 60 GHz indoor channel using a directional horn antenna with 7° HPBW in the azimuth plane and 29 dBi of gain at the RX, and an open-ended waveguide with 90° HPBW in the azimuth plane and 6.7 dBi of gain at the TX [13, 70]. A sliding correlator channel sounder was utilized with an RF null-to-null bandwidth of 200 MHz and a 10 ns time resolution, with power delay profiles (PDPs) or channel impulse responses, captured at discrete pointing angles while rotating the RX antenna. LOS measurements resulted in a PLE less than 2 (theoretical FSPL), relative to a 1 m close-in free space reference distance. These findings were similar to those at lower frequencies in indoor environments, where ground and ceiling bounce reflections and a waveguide effect are known to increase power at the receiver such that the measured path loss is less than theoretical FSPL.

Measurements similar to those conducted by Xu *et al.*, were performed by Bensebti *et al.* to study large-scale path loss in the indoor multipath propagation channel at 60 GHz at the University of Bristol using a spread spectrum channel sounder with directional, semi-directional, and omnidirectional TX and RX antennas placed at heights of 1.5 m [71]. Excess delay spreads ranged from 10 ns to 40 ns over short distances, with minimal deep fades. The total received discrete power was exponentially distributed in a LOS environment along a corridor that was 3 m x 30 m for 7 m to 33 m transmitter-receiver (T-R) separation distances.

Zwick *et al.* performed numerous wideband channel measurements at 60 GHz using a heterodyne transmitter and receiver. They measured propagation at 60 GHz with a channel sounder consisting of a 500 MHz bandwidth (2 ns resolution) PN sequence as the probing signal that was transmitted at 10 different frequency slots between 59 GHz and 64 GHz and concatenated the measurements (for 5 GHz of total bandwidth), using omnidirectional antennas in several different rooms for short-range distances [72]. Using omnidirectional TX and RX antennas, they measured median RMS delay spreads from 3 ns to 9 ns, in addition to calculating a PLE of 1.33 relative to a 1 m free space reference distance and a shadow factor of 5.1 dB across all measurements.

Geng *et al.* conducted 60 GHz propagation measurements in various indoor environments in continuous-route (CR) and direction-of-arrival (DOA) measurement campaigns [73]. The RMS delay spread trended to a log-normal distribution, and the typical range was from 3 ns to 80 ns. The propagation mechanisms were studied based on DOA measurements, indicating that the direct wave and the first-order reflected waves

from smooth surfaces were sufficient in LOS propagation environments, while in NLOS cases, diffraction was a significant propagation mechanism, and the transmission loss through walls was very high. Geng *et al.* also conducted 60 GHz measurements in corridor, LOS hallway, and NLOS hallway environments, and the measured PLEs were 1.6 in LOS corridor, 2.2 in LOS hallway, and 3.0 in NLOS hallway environments [74].

Anderson *et al.* conducted indoor wideband measurements at 2.5 GHz and 60 GHz using a broadband vector sliding correlator channel sounder to record PDPs [75, 76]. For the 2.5 GHz measurements, both the transmitter and receiver antennas were vertically polarized omnidirectional biconical antennas with 6 dBi of gain. The transmit power before the antenna was 0 dBm in order to emulate the same operating power of 2.4 GHz WLAN networks. For the 60 GHz measurements, vertically polarized pyramidal horn antennas with 25 dBi of gain and a HPBW of 50° were used at both the transmitter and receiver. The transmit power was -10 dBm in order to maintain the linear operation of the power amplifier at the transmitter and to avoid saturating the low noise amplifier of the receiver at short distances. An EIRP of 15 dBm was comparable to the power of a femtocellular system to study a typical single-cell-per-room network environment. Anderson *et al.* selected eight transmitter locations and 22 receiver locations with T-R separation distances from 3.5 m to 27.4 m on the same floor in a modern office building with a variety of obstructions in the signal path [75, 76]. The transmitter and receiver locations were chosen to represent a wide range of typical office femtocellular propagation environments. The heights of the transmitter and receiver antennas were 1.2 m relative to the ground, with an exception at one receiver location where the RX antenna was 2.4 meters relative to the floor. By using a minimum mean square error fit, the PLE with respect to a 1 m free space reference distance at 2.5 GHz was found to be 2.4 with a standard deviation of 5.8 dB, and at 60 GHz the PLE was 2.1 with a standard deviation of 7.9 dB.

Manabe *et al.* investigated how the radiation patterns and antenna polarizations at remote terminals affects multipath propagation characteristics at 60 GHz, in a conference room [77, 78]. Four types of antennas were used to examine the effects of radiation patterns of RX antennas: an omnidirectional antenna and three directive antennas with wide, medium, and narrow HPBWs. The use of a directive antenna at the remote terminal was an effective method to reduce the effects of multipath propagation. Further reduction in multipath effects was achieved with the use of circularly polarized directive antennas instead of linearly polarized directive antennas.

In 2005, Moraitis and Constantinou performed indoor 60 GHz radio channel measurements by recording power delay profiles using a direct RF pulse technique with a 10 ns repetitive square pulse, modulated up to the 60 GHz carrier having a bandwidth of 100 MHz and 10 dBm of transmit power while using identical 21 dBi vertically polarized horn antennas at the TX and RX [79]. The extracted power delay profiles revealed that excess delay was much less in hallways (up to 8.18 ns) compared to offices (up to 14.69 ns). The measurements also revealed that the office environment did not experience large channel variation over local areas.

Maltsev *et al.* used an 800 MHz OFDM channel sounder centered at 60 GHz using circular horn antennas at the transmitter and receiver and found that cross-polarized antennas in LOS environments could yield approximately 20 dB of isolation at 60 GHz [14, 80], and about 10-20 dB of isolation for NLOS environments. Torkildson *et al.* investigated the potential for exploiting spatial multiplexing as a means to increase spectral efficiency at 60 GHz in an indoor environment [81, 82]. The robustness of a link was observed to improve by increasing the number of antennas at the RX, which would also reduce the sensitivity of the channel capacity. The indoor channel was significantly degraded when the LOS path was blocked due to an obstruction, suggesting more accurate and elaborate channel models were needed to better assess link performance in the absence of a LOS path.

Aside from the majority of indoor propagation research at 60 GHz, little is known about other mmWave bands. In the early 1990's, Motorola conducted extensive 18 GHz indoor propagation measurements using both sectored and omnidirectional antennas in support of their Altair WLAN product, but little was

published. Haneda *et al.* conducted numerous measurement campaigns in the 60 GHz and 70 GHz bands in indoor shopping malls, railway stations, and office environments using a VNA based channel sounding method over 5 GHz of bandwidth [83, 84]. The measurements employed a directional horn antenna at the TX with 20 dBi of gain, and a biconical omnidirectional antenna at the RX. Specular reflections in the propagation channel accounted for 75% of the received power in office environments, and 90% of the received power in a shopping mall and railway station, and delay spreads were similar at both 60 GHz and 70 GHz.

Wu *et al.* conducted 28 GHz indoor laboratory measurements using horn antennas that rotated in the entire azimuth plane while using a VNA to measure the channel [85]. They used the Saleh-Valenzuela model to characterize the indoor channel and were able to extract intra-cluster parameters. Lei *et al.* also performed indoor 28 GHz channel propagation measurements in an indoor environment with a VNA and a pair of 26 dBi gain horn antennas for distances up to 30 m. Path loss attenuation slopes as a function of log-distance in different indoor environments were estimated to be 2 in free space, 2.2 in a hallway, 1.2 in a corridor, and 1.8 in an office [86].

2.3 Recent Activities for Indoor MmWave Studies

Research groups are now beginning to study the indoor propagation channel at mmWave frequencies other than 60 GHz. Fixed point-to-point WLANs in the 71–76 GHz, 81–86 GHz, and 92–95 GHz bands have been, or soon will be deployed using light licensing rules and recommendations by the Federal Communications Commission (FCC) [87, 88] in the United States, the Electronic Communications Commission (ECC) [89] in Europe, the Office of Commission (Ofcom) [90] in the United Kingdom, the Canadian Radio-television and Telecommunications Commission (CRTC) [91] in Canada, and the Australian Communications and Media Authority (ACMA) [91] in Australia.

An even stronger indication for the impending use of mmWave frequency bands in future fifth generation (5G) indoor and outdoor wireless communications systems can be found in public comments filed in response to the FCC's 2014 notice of inquiry (NOI) FCC 14-154 and FCC 14-177 regarding the use of spectrum above 24 GHz [92, 93]. The UK Office of Commission (Ofcom) requested similar public comments in 2015 on the use of spectrum in higher mmWave frequency bands [94]. It is also noted here that mmWave frequencies are used for other applications and have a wide range of use cases, specifically passive imaging which is becoming more widespread as a means for detecting concealed weapons and for through-the-wall imaging [95].

Chapter 3

Measurement Descriptions

Measurements were conducted in the NYU WIRELESS research center on the 9th floor of 2 MetroTech Center in Downtown Brooklyn, New York, which is a 10-story building constructed in the early 1990's with tinted windows and steel reinforcement between each floor. The 9th floor is a typical single floor office environment with common obstructions such as desks, chairs, cubicle partitions, offices, classrooms, doors, hallways, walls made of drywall, and elevators. We tried to measure between adjacent floors (9th to 10th) with a wide range of antenna pointing angle combinations between the TX and RX at 73 GHz with maximum transmit power, but the metal and concrete structure and tinted glass windows of the building prevented any signals from being measured between adjacent office floors. This test was not attempted at 28 GHz. Identical TX and RX locations were used for both the 28 GHz and 73 GHz measurements with both co- and cross-polarization antenna configurations between the TX and RX. For co-polarization measurements, the TX and RX horn antennas were vertically polarized (V-V), whereas for the cross-polarization measurements, the TX antenna was vertically polarized and the RX antenna was horizontally polarized (V-H). Since future mmWave wireless systems will be used by people and appliances with various physical orientations, approximately half of the measurements used co-polarized antennas at the TX and RX, and half used cross-polarized antennas. TX antennas were placed 2.5 m above the floor, very close to the 2.7 m ceiling to emulate common indoor hotspot locations, and RX antennas were placed 1.5 m above the floor (typical handset level heights).

3.1 Locations and Environments

Five TX locations and 33 RX locations were selected, resulting in measurements from 48 TX-RX location combinations that had 3D transmitter-receiver (T-R) separation distances ranging from 3.9 m to 45.9 m, with RX locations chosen in LOS and NLOS environments (the floor dimensions were 35 m x 65.5 m). The 10 LOS measurement locations had 3D distances ranging from 4.6 m to 21.3 m, and the 38 NLOS measurement locations had 3D distances that ranged from 3.9 m to 45.9 m.

Fig. 3.1 displays a map of the five TX locations, the 33 RX locations (some were used for multiple transmitters), and basic descriptions of the surrounding obstructions. The 33 RX locations were randomly chosen around the corresponding TX locations with various combinations of partition materials between the TXs and RXs. The height of the office floor walls (drywall) was approximately 2.7 m, and most doors had heights of 2.1 m relative to the floor. Each TX was set to 2.5 m AGL (close to the ceiling), while each RX was set to 1.5 m AGL (just below cubicle partition heights of 1.7 m). The measurement environment was a closed-plan in-building scenario that included line-of-sight and non-line-of-sight corridor, hallway, cubicle-farm, and adjacent-room communication links. A corridor environment is when a propagating signal travels down a corridor to reach the receiver by a line-of-sight path, reflections, scattering, and/or diffraction, but not

Table 3.1: TX and corresponding RX locations measured for the 28 GHz and 73 GHz indoor propagation measurements referenced to Fig. 3.1. 3D T-R separation distance ranges are provided for each TX and corresponding RX locations, as well as RX locations that experienced outage (e.g. no detectable signal for all pointing angles) for V-V or V-H antenna polarization configurations. A “-” indicates no outage and the RX ID number indicates where an outage occurred.

TX ID	RX IDs	T-R Dist (m)	V-V Outages		V-H Outages	
			28 GHz	73 GHz	28 GHz	73 GHz
1	1–9	$6.4 \leq d \leq 32.9$	-	9	9	8, 9
2	10, 11–22, 161	$4.1 \leq d \leq 45.9$	-	17, 20	14, 15, 17	13–15, 17, 19, 20
3	16,17, 23–27	$5.3 \leq d \leq 8.7$	-	-	-	-
4	11–16, 18, 28, 121, 161	$7.1 \leq d \leq 33.0$	-	-	-	-
5	8, 19, 28–33	$3.9 \leq d \leq 31.2$	-	-	-	-

penetration. An open-plan environment includes a cubicle-farm and a central TX location around soft partitions such as cubicle walls [43, 96]. A closed-plan environment is when a propagating signal must penetrate an obstruction such as a fixed building wall to reach the receiver. All of these measurement environments typically occur in a closed-plan indoor environment.

A subset of RX locations (typically 8 to 10) were measured for each TX location during the measurement campaign. The identical 48 TX-RX location combinations were measured at 28 GHz and 73 GHz, to enable direct comparison across the two frequency bands. Table 3.1 provides the RX locations that were measured for each TX location, and indicates which TX-RX combinations resulted in outages (for V-V, V-H, or both antenna polarization configurations).

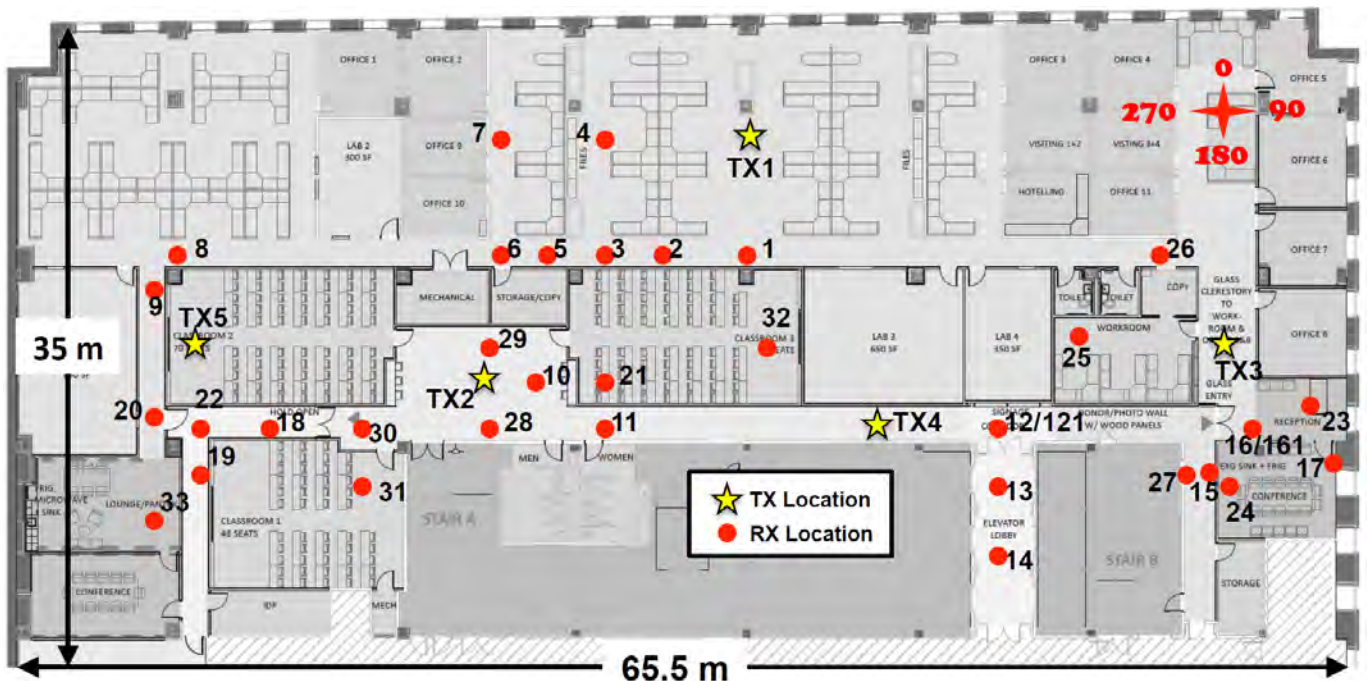


Fig. 3.1: Map of the 2 MetroTech Center 9th floor with five TX locations and 33 RX locations. The yellow stars represent the TX locations, and the red dots represent the RX locations.

Measured environment types were categorized according to the following definitions for each unique antenna pointing angle in the azimuth and elevation planes between the TX and RX antennas:

- **Line-of-Sight Boresight (LOS_B)**: when both the TX and RX antennas are pointed directly towards each other on boresight and aligned in both the azimuth and elevation planes with no obstructions between the antennas. For LOS environments, only the first rotation index (**Rot 0**)* of **Measurement 1** and **Measurement 9** (RX sweeps), and of **Measurement 6** and **Measurement 14** (TX sweeps) were considered LOS_B measurements since the **Rot 0** index of those specific measurements corresponds to when the TX and RX antennas are as close to true boresight-to-boresight as possible.
- **Line-of-Sight Non-Boresight (LOS_NB)**: when the TX and RX antennas have no obstructions between them, but the antennas are not pointed directly towards each other in either the azimuth or elevation plane, or both, commonly known as *off-boresight*. In LOS environments, for all measurement rotations except the LOS boresight angle configuration, the TX and RX antennas are NOT aligned on boresight with each other (labeled as LOS_NB).
- **Non-Line-of-Sight (NLOS)**: when the TX and RX antennas are in an environment with obstructions between each other, with no clear optical path between the two.

Chapter 4 describes the path loss models used to characterize each environment for both directional and omnidirectional cases. The following subsections describe the environment and specifications for each TX location used, and the corresponding RX locations used for each. Again, each TX-RX location combination was measured for both the 28 GHz and 73 GHz mmWave bands.

3.1.1 MTC1 and corresponding RX locations

The first TX location (MTC1) was placed in the center of an open area office space inside the NYU WIRELESS research center on the 9th floor of 2 MetroTech Center. Nine RX locations (RX1 to RX9) were identified with T-R separation distances, that ranged from 6.4 m to 32.9 m. Fig. 3.2 displays the open area working space with office partitions such as cubicles, desks, chairs, metal shelves, and wood closets. The nine RX locations were chosen around the TX with various combinations of office partitions and walls between the TX and RX. The TX antenna was set 2.5 m AGL near the ceiling (2.7 m), to emulate current indoor wireless access points, and the nine RX's were set at heights of 1.5 m AGL (typical heights of mobile devices). Cubicle partition heights were 1.7 m relative to the floor, slightly higher than the RX height.

Fig. 3.3 displays a map of MTC1 with its corresponding RX locations (RX1 to RX9). Table 3.2 provides the T-R separation distances, initial TX and RX antenna azimuth and elevation pointing angles, and environments for both the co- and cross-polarization measurements, for each TX-RX location combination. The initial TX and RX azimuth and elevation angles indicated in Tables 3.2 – 3.6 are calculated according to basic trigonometry formulas using the measured T-R separation distances and TX and RX heights. Field antenna alignment tests were conducted at LOS RX locations to find the true boresight angle combinations that resulted in the strongest received power, thus, some of the indicated elevation angles may be different from the calculated elevation angle values, due in part to the different sizes of our up- and down- converter boxes and the two sets of antennas used for the 28 GHz and 73 GHz frequency bands. Note that the TX and RX elevation angle combinations of the MTC1-RX1 location combination for the 28 GHz measurements are slightly different than for the 73 GHz measurements. The field antenna alignment test indicated that the $-8^\circ/+8^\circ$ TX/RX elevation angles for the TX and RX1 resulted in the strongest received power for the 28 GHz measurements, whereas the $-9^\circ/+9^\circ$ TX/RX elevation angles for the TX and RX1 antennas resulted in the strongest received power for the 73 GHz measurements.

*Rot, the abbreviation for *Rotation* will be explained later



Fig. 3.2: View of the open office area for the MTC1 TX location on the 9th floor of 2 MetroTech Center. Partition panels and furniture occupy a majority of the working area and can be categorized as office partitions.

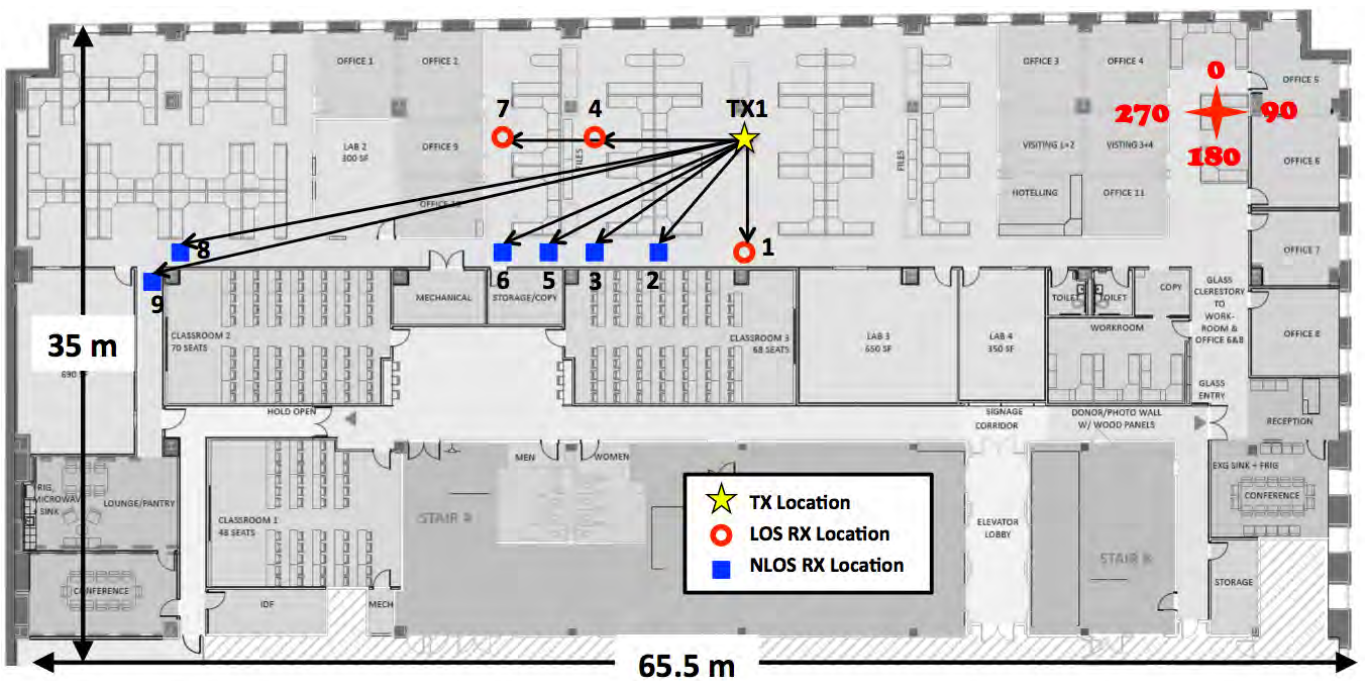


Fig. 3.3: Map displaying the MTC1 TX location and RX1-RX9 locations. The yellow star indicates the MTC1 TX location, the open red circles indicate LOS RX locations, and solid blue squares indicate NLOS RX locations. The nine RX locations were chosen around the TX and the area between each TX-RX location combination includes various office partitions and walls. The black arrows originating from the TX location indicate the initial TX antenna azimuth pointing angles for a particular RX location. All measured azimuth angles are identified with respect to the compass in the upper right corner of the figure, where the positively increasing direction is clockwise. The initial TX and RX antenna azimuth and elevation pointing angles are provided in Table 3.2

Table 3.2: TX and RX location IDs, T-R separation distances, initial TX and RX antenna azimuth and elevation pointing angles for each TX-RX location combination, and environment types for the co- and cross-polarization antenna configuration measurements for the MTC1 TX location. All angle configurations are the same for both 28 GHz and 73 GHz measurements for RX2-RX9. However, the RX1 initial angle configurations were different for the 28 GHz and 73 GHz measurements, as specified in the table.

TX	RX	T-R Distance (m)	TX Azimuth($^{\circ}$)	TX Elevation($^{\circ}$)	RX Azimuth($^{\circ}$)	RX Elevation($^{\circ}$)	Environment
MTC1	1	6.4	180	-8 (28 GHz) / -9 (73 GHz)	0	8 (28 GHz) / 9 (73 GHz)	LOS
MTC1	2	7.8	216	-7	36	7	NLOS
MTC1	3	10.1	231	-6	51	6	NLOS
MTC1	4	7.9	270	-7	90	7	LOS
MTC1	5	11.9	238	-5	58	5	NLOS
MTC1	6	14.4	244	-4	64	4	NLOS
MTC1	7	12.9	270	-7	90	7	LOS
MTC1	8	25.9	258	-2	78	2	NLOS
MTC1	9	32.9	256	-2	76	2	NLOS

3.1.2 MTC2 and corresponding RX locations

The second TX location (MTC2) was located in the center of an open area outside the NYU WIRELESS research center on the 9th floor of 2 MetroTech Center. Specifically, MTC2 was placed in a lobby outside of two classrooms and at one end of a long corridor. One RX location (RX10) was in a LOS environment, and 13 RX locations (RX11-RX22 and RX161) were in a NLOS environment, for the MTC2 TX location. Fig. 3.4 displays the TX MTC2 location outside one of the classrooms.

Fig. 3.5 displays a map of MTC2 with its corresponding RX locations (RX10 to RX22 and RX161). The blockage materials include drywall outside the classrooms and along the corridor, glass doors at the front entrance of the NYU WIRELESS research center, metal doors at the rear entrance of NYU WIRELESS, wooden doors with glass windows at the corridor entrance, and elevator doors. RX locations were chosen with various combinations of partitions in order to study the loss caused by multiple obstructions and reflections for NLOS indoor environments. The RX161 location was at the exact same position as RX16, but with the glass door kept open at the front of the NYU WIRELESS entrance. Table 3.3 lists the T-R

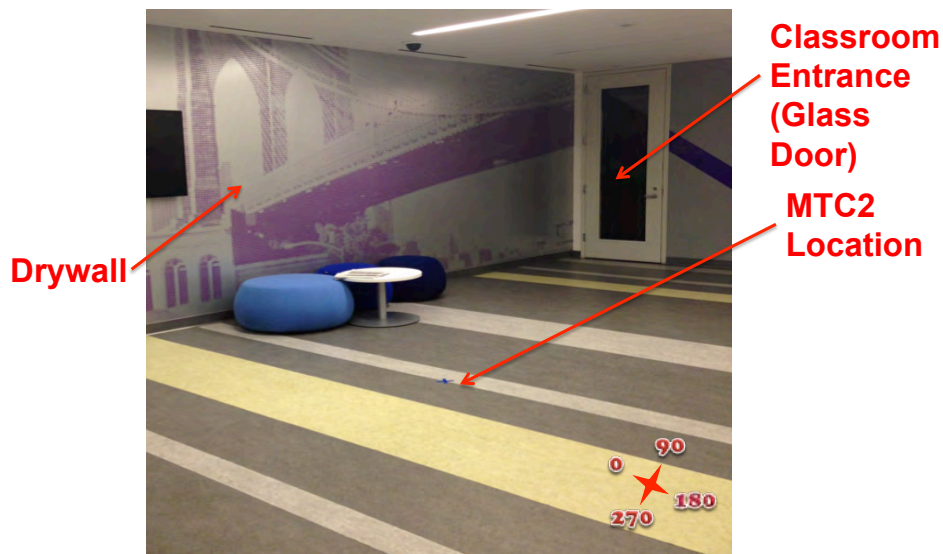


Fig. 3.4: View of the lobby area outside of two classrooms at the end of a long corridor for the MTC2 TX location.

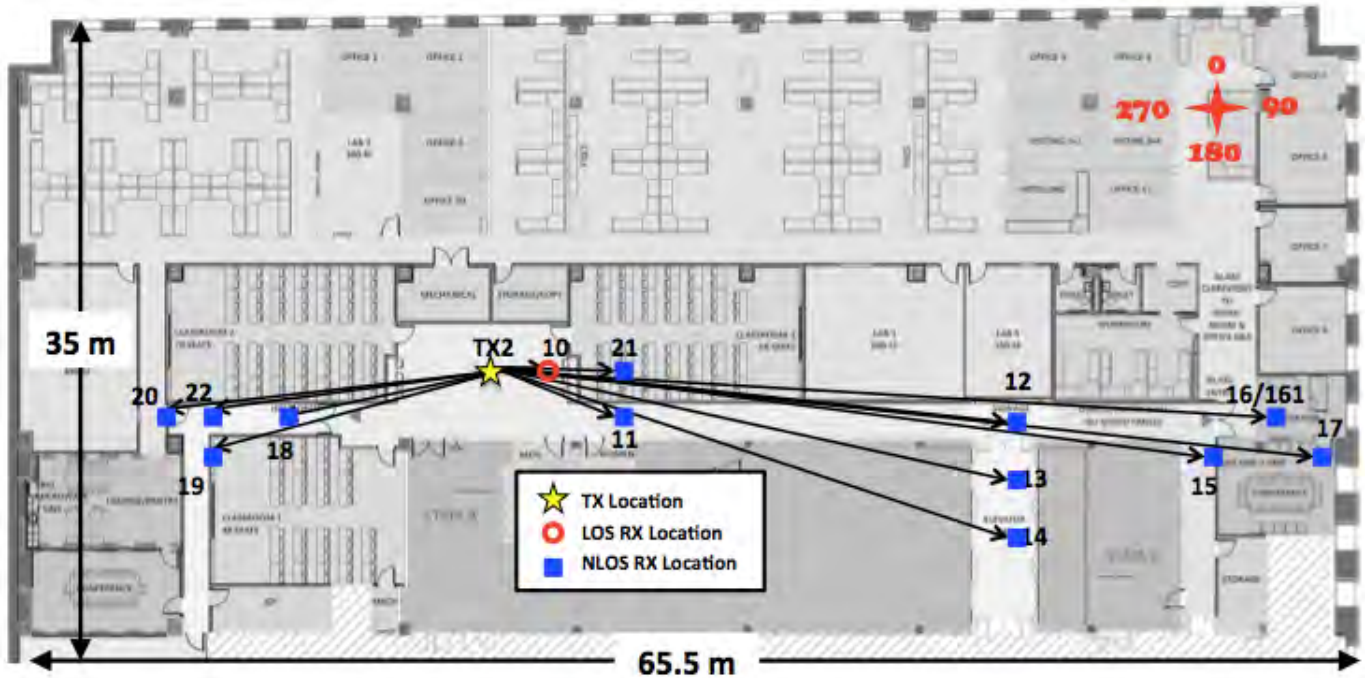


Fig. 3.5: Map displaying the MTC2 TX location, RX10 to RX22, and RX161 locations. The yellow star indicates the MTC1 TX location, the open red circles indicate LOS RX locations, and solid blue squares indicate NLOS RX locations. The 14 RX locations were chosen around the TX and the area between each TX-RX link combination includes various obstructions and partitions such as drywall, elevators, glass doors, and metal doors. RX16 and RX161 are at the same location, but with the NYU WIRELESS front entrance glass door closed for RX16, and open for RX161. The black arrows originating from the TX location indicate the initial TX azimuth boresight angles for a particular RX location. All measured azimuth angles are identified with respect to the compass in the upper right corner of the figure, where the positively increasing direction is clockwise. The initial TX and RX antenna azimuth and elevation pointing angles are provided in Table 3.3.

Table 3.3: TX and RX location IDs, T-R separation distances, initial TX and RX antenna azimuth and elevation pointing angles for each TX-RX location combination, and environment types for the co- and cross-polarization antenna configuration measurements for the MTC2 TX location. All angle configurations are identical for the 28 GHz and 73 GHz measurements.

TX	RX	T-R Distance (m)	TX Azimuth($^{\circ}$)	TX Elevation($^{\circ}$)	RX Azimuth($^{\circ}$)	RX Elevation($^{\circ}$)	Environment
MTC2	1	4.1	90	-14	270	14	LOS
MTC2	11	9.0	108	-6	288	6	NLOS
MTC2	12	28.5	96	-2	276	2	NLOS
MTC2	13	29.2	104	-2	284	2	NLOS
MTC2	14	30.4	111	-2	291	2	NLOS
MTC2	15	39.2	99	-1	279	1	NLOS
MTC2	16	41.9	94	-1	274	1	NLOS
MTC2	161	41.9	94	-1	274	1	NLOS
MTC2	17	45.9	96	-1	276	1	NLOS
MTC2	18	12.1	257	-5	77	5	NLOS
MTC2	19	15.5	250	-4	70	4	NLOS
MTC2	20	17.1	261	-3	81	3	NLOS
MTC2	21	6.7	90	-9	270	9	NLOS
MTC2	22	14.8	259	-4	79	4	NLOS

separation distances, initial TX and RX antenna azimuth and elevation pointing angle combinations, and environments for both the co- and cross-polarization measurements, for each TX-RX location combination.

3.1.3 MTC3 and corresponding RX locations

The third TX location (MTC3) was located in the center of an office area inside the NYU WIRELESS research center on the 9th floor of 2 MetroTech Center. One LOS RX location (RX16) and six NLOS RX locations (RX17 and RX23-RX27) were measured for the MTC3 TX location. Fig. 3.6 displays the MTC3 TX location, with the TX located outside several office rooms near the front entrance of the NYU WIRELESS research center.

Fig. 3.7 displays a map of MTC3 with its corresponding RX locations (RX16, RX17, and RX23-RX27). The environment obstructions include drywall, glass doors at the front entrance of NYU WIRELESS, office doors, and metal doors at the nearby conference room. Table 3.4 lists the T-R separation distances, the initial TX and RX antenna azimuth and elevation pointing angle combinations, and the environments for both co- and cross-polarization measurements, for each TX-RX location combination.



Fig. 3.6: View of the open room area with partition panels and office furniture obstructions near the MTC3 TX location.

Table 3.4: TX and RX location IDs, T-R separation distances, initial TX and RX antenna azimuth and elevation pointing angles for each TX-RX location combination, and environment types for the co- and cross-polarization antenna configuration measurements for the MTC3 TX location. All angle configurations are identical for the 28 GHz and 73 GHz measurements.

TX	RX	T-R Distance (m)	TX Azimuth($^{\circ}$)	TX Elevation($^{\circ}$)	RX Azimuth($^{\circ}$)	RX Elevation($^{\circ}$)	Environment
MTC3	16	5.3	163	-11	243	11	LOS
MTC3	17	8.7	144	-7	224	7	NLOS
MTC3	23	5.6	133	-10	313	10	NLOS
MTC3	24	7.8	180	-8	0	8	NLOS
MTC3	25	8.4	266	-7	86	7	NLOS
MTC3	26	5.5	318	-10	138	10	NLOS
MTC3	27	8.3	194	-7	14	7	NLOS

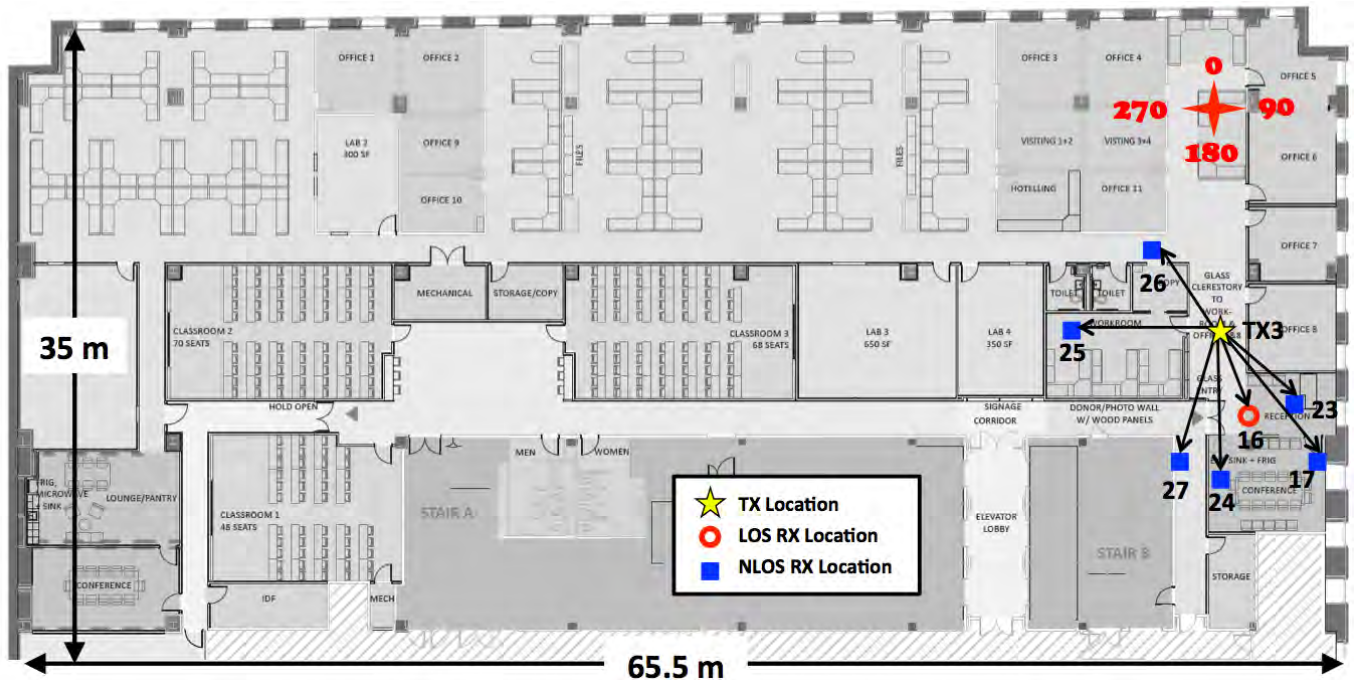


Fig. 3.7: Map displaying the MTC3 TX location, RX16, RX17, and RX23-RX27 locations. The yellow star indicates the MTC3 TX location, the open red circle indicates the LOS RX location, and the solid blue squares indicate the NLOS RX locations. The seven RX locations were chosen around the TX and are behind various combinations of walls, glass doors, and metal doors. The black arrows originating from the TX location indicate the initial TX antenna azimuth pointing angles for a particular RX location. All measured azimuth angles were identified with respect to the compass in the upper right corner of the map, where the positively increasing direction is clockwise. The initial TX and RX antenna azimuth and elevation pointing angles are provided in Table 3.4.

3.1.4 MTC4 and corresponding RX locations

The fourth TX location (MTC4) was located in a corridor outside the elevator partition entrance of the NYU WIRELESS research center on the 9th floor of 2 MetroTech Center. Four LOS RX locations (RX11, RX12, RX28, and RX121) and six NLOS RX locations (RX13-RX16, RX18, and RX161) were measured for the MTC4 TX location. Fig. 3.4 displays the corridor environment of the MTC4 TX location.

Fig. 3.9 displays a map of MTC4 with its corresponding RX locations (RX11-RX16, RX18, RX28, RX121, and RX161). The environment and obstructions consist of drywall, glass doors at the front entrance of NYU WIRELESS, metal doors at the rear entrance of NYU WIRELESS, and elevators outside the partitioned entrance. The heights of all the blockage materials are the same as the ceiling height (2.7 m). The RX121 and RX161 locations are identical to RX12 and RX16, respectively, except the glass door entrance to the front of the NYU WIRELESS research center was closed for RX12 and RX16 measurements, and was open for the RX121 and RX161 measurements. Table 3.5 lists the T-R separation distances, initial TX and RX antenna azimuth and elevation pointing angle combinations, and environments for both the co- and cross-polarization measurements, for each TX-RX location combination.



Fig. 3.8: View of the long corridor where the MTC4 TX was placed outside of the elevator partition entrance.

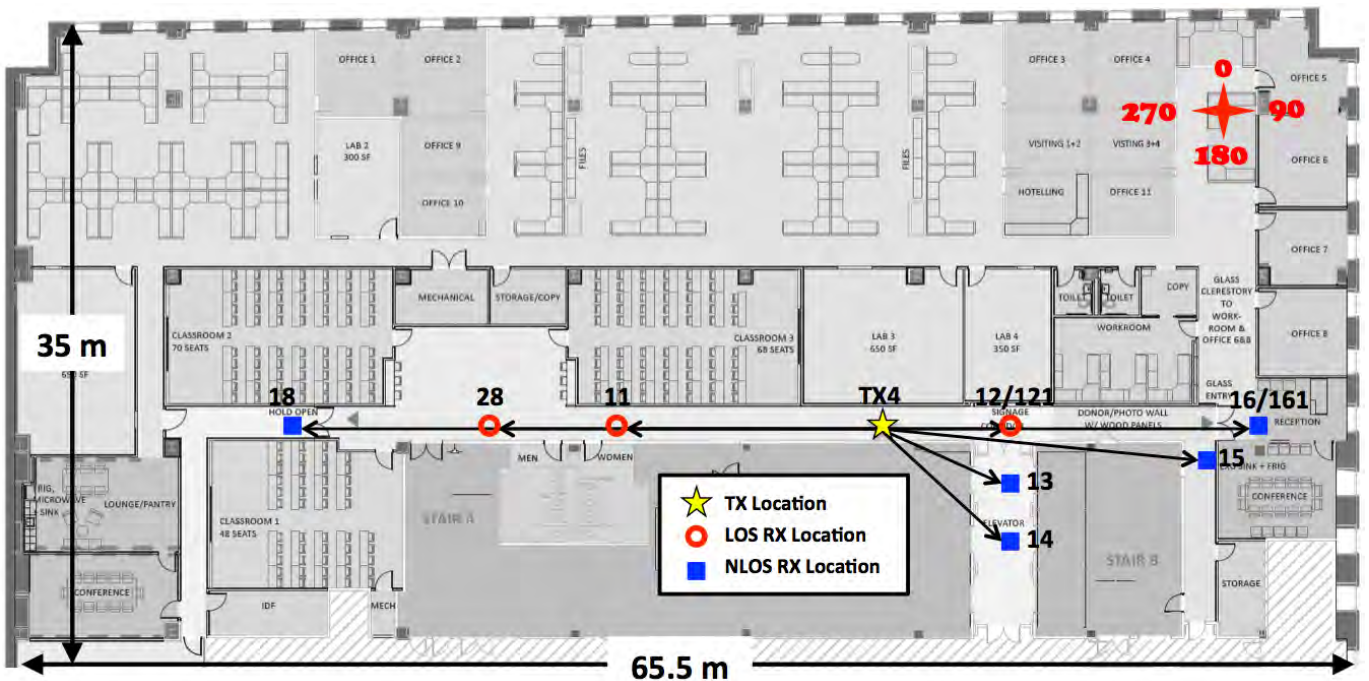


Fig. 3.9: Map showing the MTC4 location and corresponding RX11-RX16, RX18, RX28, RX121, and RX161 locations. The yellow star indicates the MTC4 TX location, the open red circles indicate the four LOS RX locations, and the solid blue squares indicate the six NLOS RX locations. The black arrows originating from the TX location indicate the initial TX antenna azimuth pointing angles for a particular RX location. All azimuth angles in the measurements were with respect to the compass in the upper right corner of the map, where the positively increasing direction is clockwise. The initial TX and RX antenna azimuth and elevation pointing angles are provided in Table 3.5.

Table 3.5: TX and RX location IDs, T-R separation distances, initial TX and RX antenna azimuth and elevation pointing angles for each TX-RX location combination, and environment types for the co- and cross-polarization antenna configuration measurements for the MTC4 TX location. All angle configurations are identical for the 28 GHz and 73 GHz measurements.

TX	RX	T-R Distance (m)	TX Azimuth($^{\circ}$)	TX Elevation($^{\circ}$)	RX Azimuth($^{\circ}$)	RX Elevation($^{\circ}$)	Environment
MTC4	11	12.7	270	-5	90	5	LOS
MTC4	12	7.1	90	-8	270	8	LOS
MTC4	121	7.1	90	-8	270	8	LOS
MTC4	13	8.2	120	-7	300	7	NLOS
MTC4	14	10.8	139	-5	319	5	NLOS
MTC4	15	20.8	100	-3	280	3	NLOS
MTC4	16	20.6	90	-3	270	3	NLOS
MTC4	161	20.6	90	-3	270	3	LOS
MTC4	18	33.0	270	-2	90	2	NLOS
MTC4	28	21.3	270	-3	90	3	LOS

3.1.5 MTC5 and corresponding RX locations

The fifth TX location (MTC5) was located in a classroom adjacent to the long corridor on the 9th floor of 2 MetroTech Center. Eight RX locations (RX8, RX19, and RX28-RX33) were selected, all in NLOS environments. Fig. 3.10 displays the classroom environment for the MTC5 TX location.

Fig. 3.11 displays the RX locations placed outside of the classroom on the 9th floor of 2 MetroTech Center. The blockage materials included numerous drywalls outside the classroom and along the corridor, and metal doors at the rear entrance of NYU WIRELESS. Table 3.6 lists the T-R separation distances, initial TX and RX antenna azimuth and elevation pointing angle combinations, and environments for both the co- and cross-polarization measurements, for each TX-RX location combination.

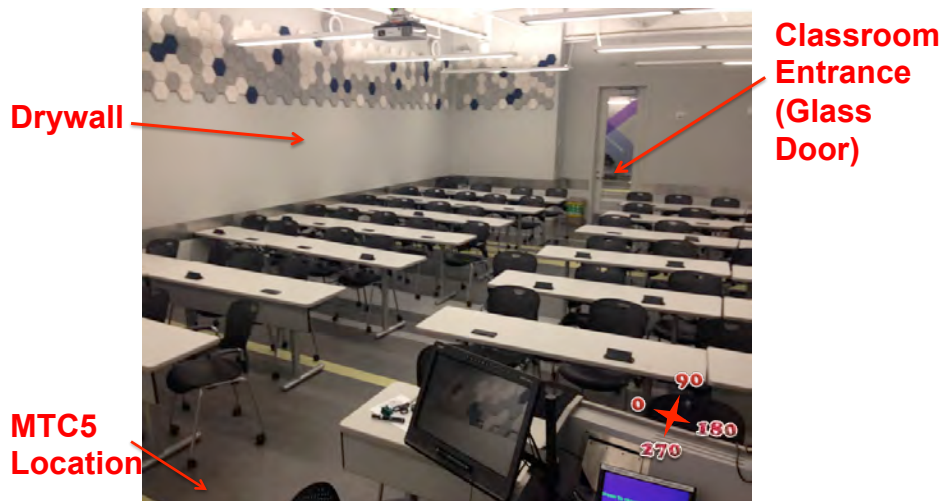


Fig. 3.10: View of the inside of the classroom where the MTC5 TX location was placed, surrounded by desks and chairs.

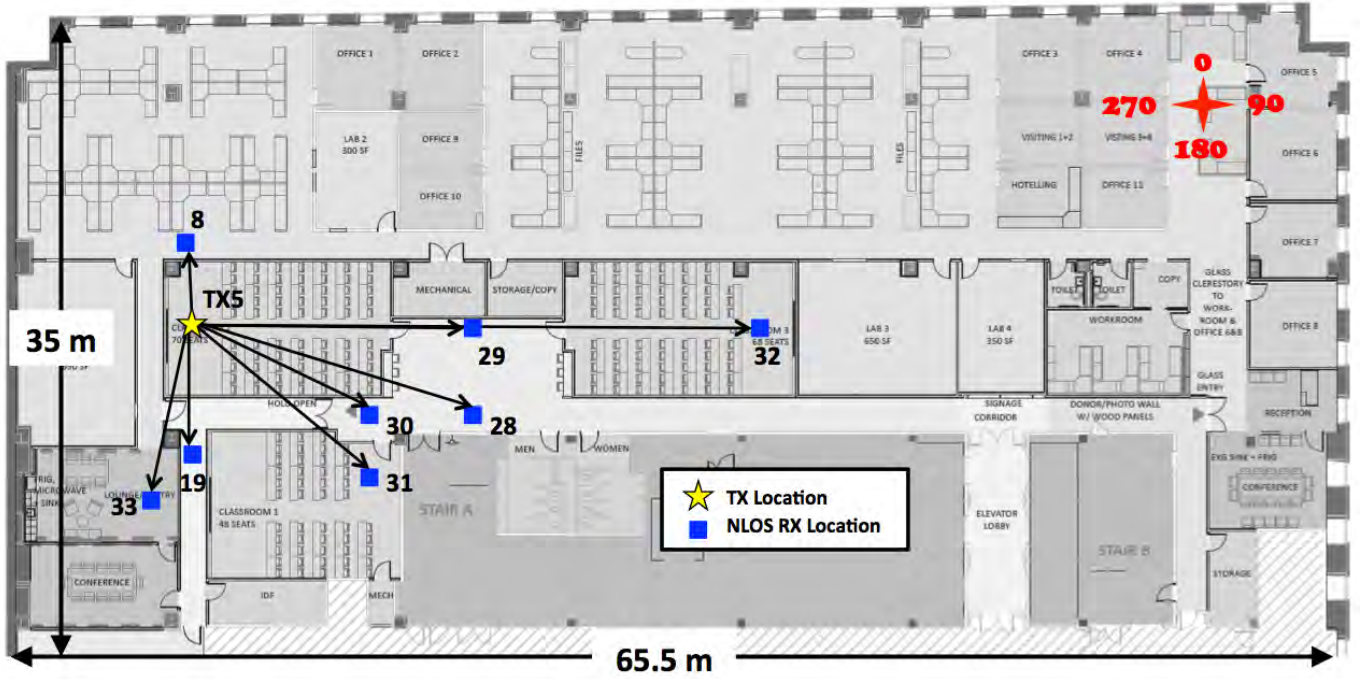


Fig. 3.11: Map displaying the MTC5 TX location, and RX8, RX19, and RX28-RX33 locations. The yellow star indicates the MTC5 TX location and the solid blue squares indicate the eight NLOS RX locations. The black arrows originating from the TX location indicate the initial TX antenna azimuth pointing angles for a particular RX location. All azimuth angles in the measurements were with respect to the compass in the upper right corner of this figure, where the positively increasing direction is clockwise. The initial TX and RX antenna azimuth and elevation pointing angles are provided in Table 3.6.

Table 3.6: TX and RX location IDs, T-R separation distances, initial TX and RX antenna azimuth and elevation pointing angles for the each TX-RX location combination, and environment types for the co- and cross-polarization antenna configuration measurements for the MTC5 TX location. All angle configurations are identical for the 28 GHz and 73 GHz measurements.

TX	RX	T-R Distance (m)	TX Azimuth(°)	TX Elevation(°)	RX Azimuth(°)	RX Elevation(°)	Environment
MTC5	8	3.9	9	-14	189	14	NLOS
MTC5	19	6.9	180	-8	0	8	NLOS
MTC5	28	15.6	106	-4	286	4	NLOS
MTC5	29	15.0	90	-4	270	4	NLOS
MTC5	30	11.4	127	-5	307	5	NLOS
MTC5	31	13.9	139	-4	319	4	NLOS
MTC5	32	31.2	90	-2	270	2	NLOS
MTC5	33	9.1	193	-6	13	6	NLOS

3.2 System Descriptions

Two 400 Mcps broadband sliding correlator channel sounders were employed, one at 28 GHz and the other at 73 GHz, both consisting of similar architectures with varying Intermediate Frequency (IF) and Local Oscillator (LO) frequencies, as well as interchangeable RF up- and down-converter front-ends.

3.2.1 Transmitter Hardware

The TX sides of the channel sounding systems used for the 28 GHz and 73 GHz measurements are displayed in Figs 3.12 and 3.13, respectively. The systems used state-of-the-art signal generators provided by National Instruments (NI) and PhaseMatrix for an Intermediate Frequency (IF) of 5.4 GHz and 5.625 GHz and a Local Oscillator (LO) frequency of 22.6 GHz and 22.625 GHz (subsequently tripled to 67.875 GHz) for the 28 GHz and 73 GHz measurements, respectively. At the TX, we generated a maximal length 2047 pseudorandom noise (PN) sequence (or pseudorandom binary sequence (PRBS)) clocked at 400 MHz, which was mixed with the IF of 5.4 GHz or 5.625 GHz, and was then modulated with either the LO of 22.6 GHz or 67.875 GHz, allowing us to reach either center frequency of 28 GHz or 73.5 GHz, respectively, resulting in an RF signal with 800 MHz null-to-null bandwidth. The 22.625 GHz LO frequency used in the 73 GHz system was frequency-tripled inside the RF up-converter to achieve an LO of 67.875 GHz. The RF signal was transmitted through a highly-directional horn antenna (mounted to a waveguide output) with 15 dBi of gain (28.8° azimuth HPBW) and 20 dBi of gain (15° azimuth HPBW) for the 28 GHz and 73 GHz measurements, respectively.

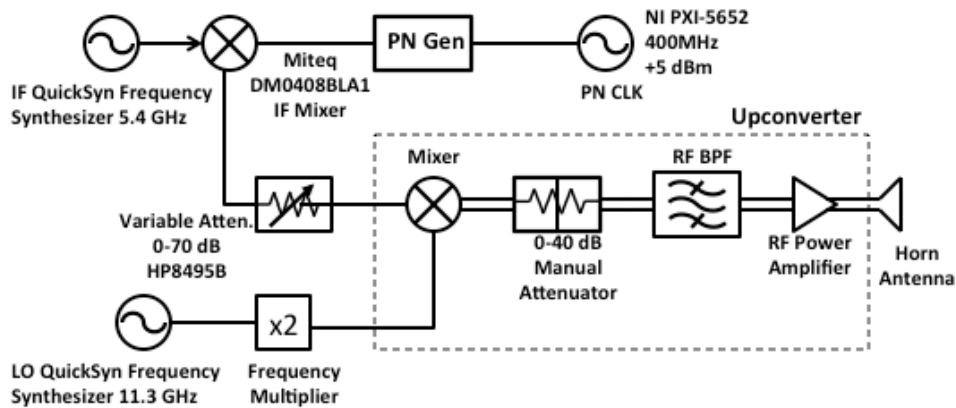


Fig. 3.12: Block diagram of the 28 GHz transmitter. The TX PN generator produced a 400 Mcps PN sequence that was modulated by a 5.4 GHz IF and then multiplied by a 22.6 GHz LO, thus upconverted to a 28 GHz centered RF signal. The RF signal was then transmitted through a highly-directional horn antenna with 15 dBi of gain and 28.8° azimuth HPBW.

3.2.2 Receiver Hardware

Figs. 3.14 and 3.15 display the block diagrams of the 28 GHz and 73 GHz RX systems, respectively. In the down-converter stage, the received 28 GHz or 73.5 GHz centered spread spectrum RF signal was down-converted into the 5.4 GHz or 5.625 GHz IF, and was then further demodulated using an IF-stage LO of 5.4 GHz or 5.625 GHz, into the in-phase I and quadrature Q , baseband signals. Both the I and Q baseband components were then mixed with a PRBS sequence identical to the transmitted signal, but at a slightly slower rate of 399.95 Mcps, which produced an impulse when both codes were aligned in time. The cross-correlation mixing operation reduced the bandwidth of the I and Q signals to 50 kHz due to the time

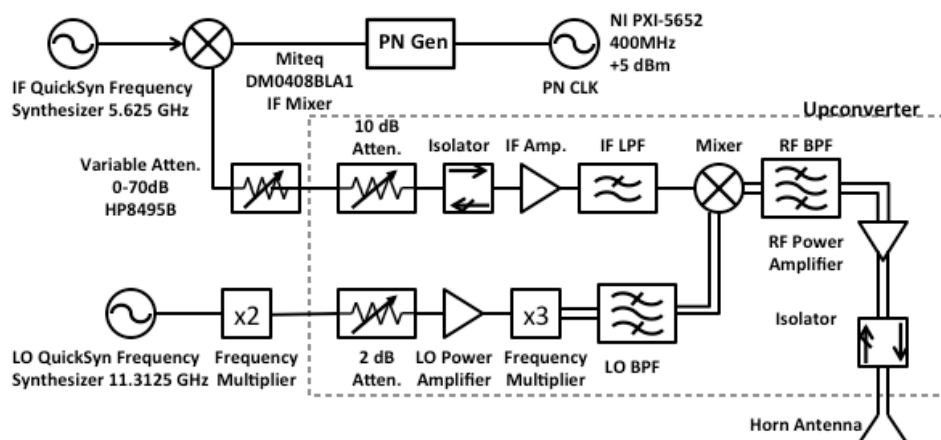


Fig. 3.13: Block diagram of the 73 GHz transmitter. The TX PN generator produced a 400 Mcps PN sequence that was modulated by a 5.625 GHz IF and then multiplied by a 67.875 GHz (tripled 22.625 GHz) LO, thus upconverted to a 73.5 GHz centered RF signal. The RF signal was then transmitted through a highly-directional horn antenna with 20 dBi of gain and 15° azimuth HPBW.

Table 3.7: Broadband sliding correlator channel sounding system specifications for the 28 GHz and 73 GHz indoor measurement campaign [6, 97–100].

Carrier Frequency	28 GHz	73.5 GHz
Probing Signal	11 th order PRBS (length=2047)	
TX PN Code Chip Rate	400 Mcps	
TX PN Code Chip Width	2.5 ns	
RX PN Code Chip Rate	399.95 Mcps	
Slide Factor	8000	
Digitizer Sampling Rate	2 Megasamples / second	
RF Bandwidth (Null-to-Null)	800 MHz	
TX/RX IF Frequency	5.4 GHz	5.625 GHz
TX/RX LO Frequency	22.6 GHz	67.875 GHz
TX/RX LO Power	10 dBm	
Max. TX Output Power	23.9 dBm	12.1 dBm
TX/RX Antenna Gain	15 dBi	20 dBi
TX/RX Azimuth HPBW	28.8°	15°
TX/RX Elevation HPBW	30°	15°
Max. TX EIRP	38.9 dBm	32.1 dBm
TX Antenna Height	2.5 m	
RX Antenna Height	1.5 m	
Max. Measureable Path Loss	152 dB	162 dB
Multipath Time Resolution	2.5 ns	
TX Polarization	Vertical	
RX Polarization	Vertical / Horizontal	

dilation properties of sliding correlation (slide factor of 8000) [49, 101, 102]. The subsequent I and Q voltage signals then passed through a 100 kHz low pass filter and were then individually sampled at 2 MS/s. Using LabVIEW software, the digital I and Q samples ($I^2 + Q^2$) were squared and then summed to generate the raw PDP of the channel. Each sampled signal resulted in a power delay profile (PDP) that was 60,000 samples long. In order to increase the SNR of the received signal, 20 successive PDPs were averaged to obtain a recorded PDP for each individual measurement[†]. At the receiver, directionality across a large portion of the azimuth and elevation planes was made possible by mechanically steering the directional receiver antennas with gimbals controlled by LabVIEW software. The flexibility in maneuvering the RX antennas allowed many different angles of arrival (AOAs) over the entire 360° azimuth plane to be measured in addition to many elevation planes. Future measurements will use recently upgraded synchronization between the TX and RX to recover true propagation delay of recorded PDPs. Table 3.7 provides the channel sounder specifications for the 28 GHz and 73 GHz measurement systems.

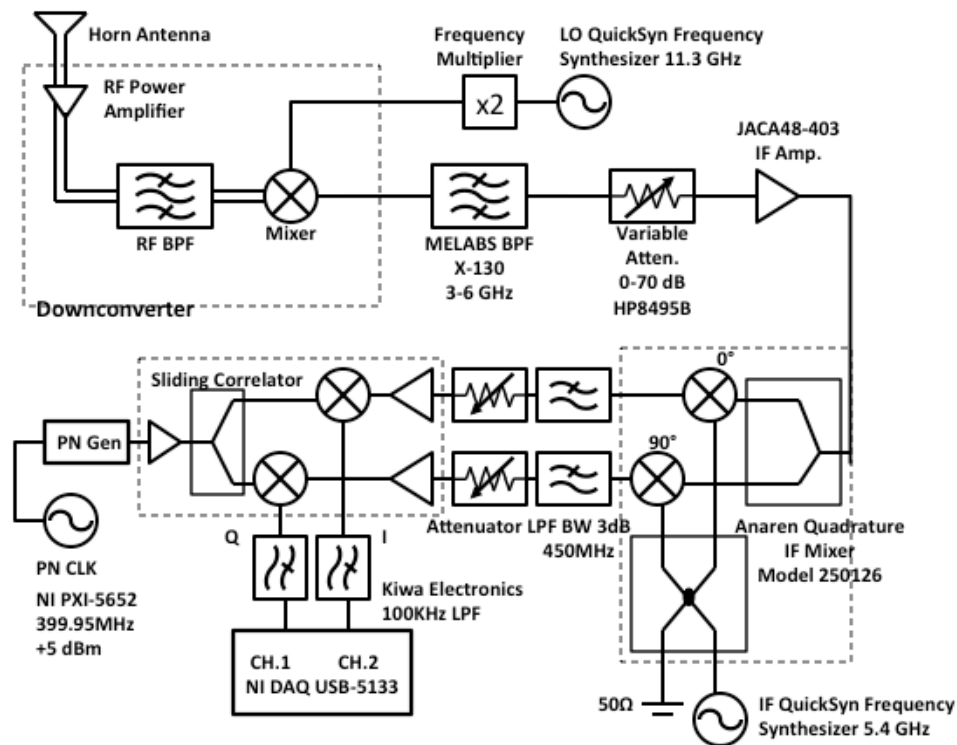


Fig. 3.14: Block diagram of the RX system used to characterize the 28 GHz indoor channel. The received signal was downconverted from the 28 GHz centered RF signal via an LO of 22.6 GHz, which was then subsequently demodulated down to its I and Q baseband components via an IF-stage 5.4 GHz LO. A PN sequence identical to that at the TX was generated, but at a slightly slower rate of 399.95 Mcps, and was then mixed with the received signal’s baseband I and Q signals, that were used to recover a time-dilated impulse response of the channel.

3.3 Measurement Procedure

The indoor measurement days started and ended with a free space system calibration routine at a known distance of 4 m, with vertically-polarized TX and RX antennas at heights of 2 m. The purpose of calibration was to find the linear range and gain of the RX system in order to recover the true received power from each individually recorded field measurement. Calibration was necessary at the end of the measurement

[†]Results in this report may be slightly different than those initially reported in [103, 104] due to this updated averaging method and the use of a more stringent 5 dB SNR thresholding algorithm described in [105].

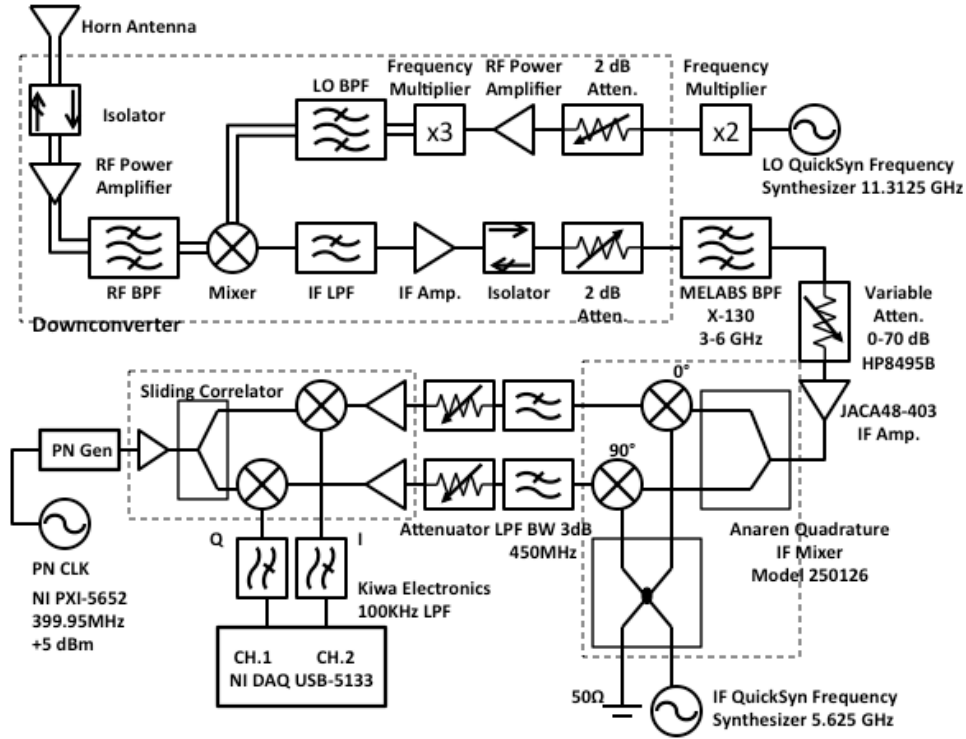


Fig. 3.15: Block diagram of the RX system used to characterize the 73 GHz indoor channel. The received signal was downconverted from the 73.5 GHz centered RF signal via an LO of 67.875 GHz, which was then subsequently demodulated down to its *I* and *Q* baseband components via an IF-stage 5.625 GHz LO. A PN sequence identical to that at the TX was generated, but at a slightly slower rate of 399.95 Mcps, and was then mixed with the received signal’s baseband *I* and *Q* signals, that were used to recover a time-dilated impulse response of the channel.

day, since the RX system gain was prone to change due to temperature fluctuations throughout the day, and to ensure equipment fidelity and accuracy after each measurement day. Therefore, field measurements conducted in the morning and afternoon would use the RX system gain calculated from the morning and end-of-day calibrations, respectively.

After calibration, the TX antenna was elevated close to the ceiling (2.5 m), to emulate typical indoor access points of office buildings. The RX was then moved to the specific measurement location, and the height of the RX antenna was set to 1.5 m AGL for each measurement. For the cross-polarization measurements (V-H), a 90° waveguide twist was attached to the antenna waveguide flange to change the polarization pattern of the RX antenna from vertical, to horizontal.

For each TX-RX location combination measured, 16 measurement sweeps in the azimuth plane for various fixed TX and RX antenna elevation angle combinations and different RX antenna polarization configurations were conducted. Measurements 1 through 8 corresponded to co-polarization (V-V) measurements, whereas Measurements 9 through 16 corresponded to cross-polarization (V-H) measurements. For each RX location, the TX and RX antennas were pointed perfectly towards each other for the initial azimuth and elevation angle setup (Measurement 1, Rotation (Rot) 0), and then the TX or RX antenna was swept in the azimuth plane in 30° or 15° step increments (depending on the antenna used for each carrier frequency as provided in Table 3.7). A PDP was recorded at each step increment in the azimuth plane for each measurement. In NLOS environments, trigonometry calculations were performed before measurements in order to point the TX and RX antennas directly towards each other in the azimuth plane for the initial angle positions, regardless of the obstructions between the two. Doing so helped us to align the antennas in NLOS environments as specified in Tables 3.2 - 3.6. Each step increment in the azimuth plane for measurement sweeps was identified by a specific rotation number. Ascending rotation numbers corresponded to the antenna moving

in the counterclockwise direction with respect to the compass in Fig. 3.1, while descending rotation numbers corresponded to the antenna moving in the clockwise direction. Tables 3.2 - 3.6 indicate the Measurement 1, Rot 0 TX and RX antenna azimuth and elevation pointing angles for each specific TX-RX location combination measured for both the 28 GHz and 73 GHz measurements.

The list of items to follow indicates the change in TX and/or RX antenna azimuth and elevation angles for the Rot 0 pointing direction of Measurements 1 through 8 (V-V). Measurements 9 through 16 (V-H) are identical to 1 through 8, except the RX antenna was configured for horizontal polarization. For RX sweeps (Measurements 1-5, 7, 9-13, and 15), the TX antenna was fixed in the azimuth and elevation planes with the RX antenna elevation fixed, and then swept in step increments in the azimuth plane. For TX sweeps (Measurements 6, 8, 14, and 16), the RX antenna was fixed in the azimuth and elevation planes with the TX antenna elevation fixed, and then swept in step increments in the azimuth plane. RX antenna sweeps are also known as AOA sweeps, and TX antenna sweeps are also known as AOD sweeps. For each measurement sweep and at each incremental step, a PDP was recorded at the RX. The detailed description of each measurement sweep is listed below. The measurement sweep descriptions hold true for both LOS and NLOS environments.

- Measurement 1 (M1): The TX and RX antennas were pointed directly towards each other on boresight in both the azimuth and elevation planes (for LOS or NLOS environments). The RX antenna was then swept in the azimuth plane in steps of 30° or 15° , for a fixed TX antenna at the boresight azimuth and elevation angles.
- Measurement 2 (M2): With respect to the boresight angle in elevation, the RX antenna was uptilted by 30° or 15° and then swept in the azimuth plane in steps of 30° or 15° , for a fixed TX antenna at the boresight azimuth and elevation angles.
- Measurement 3 (M3): With respect to the boresight angle in elevation, the RX antenna was downtilted by 30° or 15° and then swept in the azimuth plane in steps of 30° or 15° , for a fixed TX antenna at the boresight azimuth and elevation angles.
- Measurement 4 (M4): With respect to the boresight angle in elevation, the TX antenna was uptilted by 30° or 15° . The RX antenna was fixed at the boresight elevation angle, and then swept in the azimuth plane in steps of 30° or 15° .
- Measurement 5 (M5): With respect to the boresight angle in elevation, the TX antenna was downtilted by 30° or 15° . The RX antenna was fixed at the boresight elevation angle, and then swept in the azimuth plane in steps of 30° or 15° .
- Measurement 6 (M6): The TX and RX antennas were pointed directly towards each other on boresight in both the azimuth and elevation planes. The TX antenna was then swept in the azimuth plane in steps of 30° or 15° , for a fixed RX antenna at the boresight azimuth and elevation angles.
- Measurement 7 (M7): This measurement was an RX sweep with the TX antenna set to the second strongest AOD in the azimuth and elevation plane. The second strongest AOD was determined by comparing the trigger level from all the AODs during Measurement 6, except for the angles corresponding to the main angle of arrival. The RX antenna was fixed at the boresight elevation angle and then swept in steps of 30° or 15° in the azimuth plane.
- Measurement 8 (M8): This measurement corresponds to the second TX sweep with TX antenna either uptilted or downtilted by 30° or 15° after determining the elevation plane with the strongest received power from Measurement 4 and Measurement 5 during field measurements. The RX antenna was pointed towards the initial boresight azimuth and elevation angles, and the TX was uptilted or downtilted by 30° or 15° , and then swept in steps of 30° or 15° in the azimuth plane.

Table 3.8: The measurement routine for each TX and RX location combination. Elevation angles are with respect to boresight (initial) angles, which can be found in Tables 3.2 – 3.6. HPBW indicates the step increment in the azimuth plane (tilt change in the elevation plane), where the antenna azimuth HPBW for the 28 GHz measurements was 28.8° , but the step increment was 30° . As previously described the HPBW step increment for the 73 GHz measurements was 15°

Measurement Number	TX Azimuth	TX Elevation	RX Azimuth	RX Elevation	Sweep Type	Polarization
1	0	0	0	0	RX	V-V
2	0	0	0	+HPBW	RX	V-V
3	0	0	0	-HPBW	RX	V-V
4	0	+HPBW	0	0	RX	V-V
5	0	-HPBW	0	0	RX	V-V
6	0	0	0	0	TX	V-V
7	Second strongest AOD	0	0	0	RX	V-V
8	0	+/- HPBW	0	0	TX	V-V
9	0	0	0	0	RX	V-H
10	0	0	0	+HPBW	RX	V-H
11	0	0	0	-HPBW	RX	V-H
12	0	+HPBW	0	0	RX	V-H
13	0	-HPBW	0	0	RX	V-H
14	0	0	0	0	TX	V-H
15	Second strongest AOD	0	0	0	RX	V-H
16	0	+/- HPBW	0	0	TX	V-H

Measurement 9 through Measurement 16 followed the same procedure as Measurement 1 through Measurement 8, but with the RX antenna horizontally polarized. A detailed breakdown of the measurements is provided in Table 3.8. All the elevation values provided in the table are with respect to elevation boresight (or initial) angles, from Tables 3.2 - 3.6. Some measurement sweep angle combinations depended on prior sweeps and therefore were determined during field measurements, namely for Measurements 7, 8, 15, and 16.

Additionally, in order to keep the RX system performance and gain in the linear range, a variable attenuator was used to attenuate signals with strong received power (exceeding the upper bound of the linear range obtained from the morning calibration).

At each unique pointing angle combination during a measurement sweep, a PDP was acquired at the receiver. Up to 192 (16 measurements x $12 (\frac{360^\circ}{30^\circ})$ angles) and 384 (16 measurements x $24 (\frac{360^\circ}{15^\circ})$ angles) total PDPs were possible for acquisition at each TX-RX location combination for the 28 GHz and 73 GHz measurements, respectively. Measurements at most NLOS locations, however, only provided a small number of angles with energy for recording, since no PDP was acquired if there was no signal for a particular pointing angle.

This page is intentionally left blank.

Chapter 4

Large-Scale Path Loss Models

Large-scale path loss models estimate the attenuation over distance of propagating signals, and are vital for designing communications systems. Different types (deterministic, empirical, and stochastic) of large-scale path loss models exist, but measurement-based path loss models provide realistic insight into propagation characteristics of a wireless channel [105, 106].

4.1 Single Frequency Path Loss Models

A common path loss model is the close-in free space reference distance (CI) path loss model provided in Eq. (4.1) and parameterized by the average path loss exponent (PLE) n :

$$\text{PL}^{\text{CI}}(f, d)[\text{dB}] = \text{FSPL}(f, d_0) + 10n \log_{10} \left(\frac{d}{d_0} \right) + X_{\sigma}^{\text{CI}} \quad \text{for } d \geq d_0, \text{ where } d_0 = 1 \text{ m} \quad (4.1)$$

where X_{σ}^{CI} is a zero mean Gaussian random variable with standard deviation σ in dB (large-scale channel fluctuations due to shadowing [49]). The CI model uses a physically-based reference distance d_0 , where $\text{FSPL}(f, d_0) = 10 \log_{10} \left(\frac{4\pi d_0}{\lambda} \right)^2$. The CI path loss model is found by determining the PLE n via the minimum mean-square error (MMSE) approach that fits the measured data with smallest error (by minimizing σ) using a true physical anchor point that expresses the free space transmitted power from the TX antenna out to the close-in distance d_0 . The closed-form expression for optimizing the CI PLE can be found in Appendix A. For the mmWave CI model, $d_0 = 1$ m is used, proposed as a standard in [25, 105]. High gain directional antennas may have far-field radiation patterns (Fraunhofer distances) greater than 1 m from the antenna, but the CI path loss model can easily be reverted back to a 1 m reference distance by assuming that the far-field begins at 1 m (even if it does not). The error between the near- and far-field will not be significant in communication analysis using a 1 m reference distance, since very few users would ever be this close to the TX antenna, and close-in users will have extremely strong signals and little path loss [105]. Standardizing to a $d_0 = 1$ m reference distance allows for easy model comparison between different frequency bands and measurements from other researchers, and allows closed-form computation in analysis, and intuitive computation of path loss or received power without a calculator, since the power decays by $10n$ dB per decade of distance beyond 1 m [105]. The CI path loss model may be used for estimating path loss from either cross- or co-polarization measurements, or for a generalized data set that combines both co- and cross-polarized (combined polarized) measurements (as would occur in a practical cellular system with random device orientations). As shown in [105], the single parameter CI model may be used for multiple frequencies with good accuracy in outdoor channels, but as shown subsequently, a two parameter variation of the CI model offers a better fit for indoor channels.

An extension of the basic (CI) path loss model for the special case of cross-polarization propagation is to add a constant attenuation factor known as the *cross-polarization discrimination* (XPD) factor, that best fits the measured data via an MMSE method [22, 24, 49, 107] given by:

$$\text{PL}^{\text{CIX}}(f, d)[\text{dB}] = \text{FSPL}(f, d_0) + 10n_{(\text{V-V})} \log_{10} \left(\frac{d}{d_0} \right) + \text{XPD}[\text{dB}] + X_{\sigma}^{\text{CIX}} \quad (4.2)$$

This model, which we call the *close-in reference distance with XPD* (CIX) path loss model, is similar to the constant floor attenuation model introduced in [42, 43, 96], and uses the co-polarization PLE in (4.1) to determine the best fit XPD factor caused by antenna polarization mismatch. Instead of solving for a PLE for cross-polarized measured path loss in (4.1), the CIX model uses the PLE found from co-polarized antenna measurements at identical locations of cross-polarized measurements, and adds an optimized constant attenuation (XPD). One simply solves for the optimal XPD value (in dB) via the MMSE method that fits the measured cross-polarized path loss data with the smallest error (by minimizing σ). As seen from (4.2), the CIX model uses the optimum attenuation factor (XPD) in dB that is added to the CI model to minimize the error between the estimator and measured cross-polarized path loss. In (4.2), $n_{(\text{V-V})}$ represents the co-polarization PLE determined from measurements, as provided in Table 5.2, XPD is the optimized cross-polarization attenuation factor in dB, and X_{σ}^{CIX} is the zero mean Gaussian (in dB) shadow fading random variable for the CIX model in (4.2) that describes the large-scale variation of signal power about mean path loss and constant XPD attenuation term as a function of distance. The CIX model provides the best-fit to the cross-polarized data (minimizes error via MMSE), while using the co-polarized PLE from (4.1) and a 1 m free space reference distance. The CIX model closed-form expressions for optimizing the XPD value are given in Appendix A.

The *floating-intercept* (FI) path loss model is used in the WINNER II and 3GPP standards [108, 109]. This model requires two parameters and does not consider a physically-based anchor to the transmitted power, and has a similar form to (4.1):

$$\text{PL}^{\text{FI}}(d)[\text{dB}] = \alpha + 10 \cdot \beta \log_{10}(d) + X_{\sigma}^{\text{FI}} \quad (4.3)$$

where α is the floating-intercept in dB (different than a FSPL reference), and β is the slope of the line (different than a PLE), also with a zero mean Gaussian (in dB) shadow fading random variable X_{σ}^{FI} which describes large-scale signal fluctuations about the mean path loss over distance. Similar to the CI and CIX models, the best-fit involves solving for α and β to minimize σ and the closed-form optimized solutions are provided in Appendix A. Note that (4.3) requires two model parameters, whereas the CI model only required a single parameter, the PLE. Previous work indicated that the CI and FI path loss models produce very similar shadow fading standard deviations in outdoor mmWave channels [105, 110–112], casting doubt on the value of using an extra modeling parameter when there is a lack of physical relationship to transmitted power.

4.2 Multi-Frequency Path Loss Models

Standards bodies and modeling groups are also interested in multi-frequency path loss models in order to have a general form/model to cover a broad range of frequencies and measurements. The CI model (4.1) can be used for both single and multi-frequency datasets. A multi-frequency three parameter model known as the *alpha-beta-gamma* (ABG) model includes a frequency dependent and distance-dependent term to describe path loss at various frequencies [112, 113]. The ABG model equation is given by (4.4):

$$\text{PL}^{\text{ABG}}(f, d)[\text{dB}] = 10\alpha \log_{10} \left(\frac{d}{d_0} \right) + \beta + 10\gamma \log_{10} \left(\frac{f}{f_0} \right) + X_{\sigma}^{\text{ABG}}, \text{ where } d_0 = 1 \text{ m, } f_0 = 1 \text{ GHz} \quad (4.4)$$

where α and γ are coefficients that describe the distance and frequency dependence on path loss, β is an optimized offset in path loss, f is the frequency in GHz and X_σ^{ABG} is Gaussian random variable representing the shadowing or large-scale signal fluctuations about the mean path loss over distance. The ABG model is an extension of the FI model for multiple frequencies, and reverts to the FI model (when setting $\gamma = 0$ or 2) if only a single frequency is used. The ABG model is solved via MMSE to minimize σ by simultaneously solving for α , β , and γ . Note that the ABG model is identical to the CI model if we equate α in the ABG model in (4.4) with the PLE n in the CI model in (4.1), γ in (4.4) with the free space PLE of 2, and β in (4.4) with $20 \log_{10}(4\pi/c)$. Furthermore, the ABG model requires three parameters and the CI model only one parameter, and as shown subsequently, the additional two variables in the ABG model offer very little improvement in accuracy and have no tie to propagation physics [105]. The closed-form expressions for optimizing the ABG model parameters are described in Appendix A.

Similar to the CIX model, one may consider the *alpha-beta-gamma with XPD factor (ABGX)* model that is used for the specific case of cross-polarized propagation measurements. The ABGX model is provided in (4.5):

$$\text{PL}^{\text{ABGX}}(f, d)[\text{dB}] = 10\alpha \log_{10} \left(\frac{d}{d_0} \right) + \beta + 10\gamma \log_{10} \left(\frac{f}{f_0} \right) + \text{XPD}[\text{dB}] + X_\sigma^{\text{ABGX}}, \text{ where } d_0 = 1 \text{ m, } f_0 = 1 \text{ GHz} \quad (4.5)$$

where the optimum α , β , and γ values found for the ABG co-polarized measurement locations are used to solve for the XPD value using identical cross-polarized locations that minimizes σ via MMSE. The closed-form expressions that optimize the XPD factor for the ABGX model when using the optimized co-polarized ABG model parameters are provided in Appendix A.

A new simple two parameter multi-frequency model can be considered to be an extension of the CI model. The *close-in free space reference distance with frequency weighting (CIF)* path loss model is a multi-frequency, frequency weighted model that employs the same FSPL anchor at 1 m as the CI model. The CIF model equation is presented in (4.6):

$$\text{PL}^{\text{CIF}}(f, d)[\text{dB}] = \text{FSPL}(f, d_0) + 10n \left(1 + b \left(\frac{f - f_0}{f_0} \right) \right) \log_{10} \left(\frac{d}{d_0} \right) + X_\sigma^{\text{CIF}}, \text{ where } d_0 = 1 \text{ m} \quad (4.6)$$

where n denotes the distance dependency of path loss (e.g. the path loss exponent, or PLE), b is an intuitive model-fitting parameter that captures the amount of linear frequency dependency of path loss, thus modeling the results here which show that path loss increases with frequency at a specific distance for indoor channels*, f_0 is a fixed reference frequency that serves as the balancing point for the linear frequency dependency of the PLE, and is based on the average of all frequencies represented by the model, and X_σ^{CIF} is the zero mean Gaussian random variable (in dB) that describes large-scale signal fluctuations about the mean path loss over distance.

In the multi-frequency CIF model, the parameter f_0 is computed as the weighted frequency average of all measurement locations for each specific environment and antenna scenario, found by summing up the number of measurement locations at a particular frequency and antenna scenario, multiplying by the corresponding frequency, and dividing that number by the entire number of measurement locations taken over all frequencies for that specific environment and antenna scenario. Note that we round the calculated f_0 to the nearest integer in GHz. For example, the combined polarization omnidirectional multi-frequency models in this report used $f_0 = 51$ GHz in LOS and $f_0 = 49$ GHz in NLOS, based on the number of measured locations at each frequency in each environment. With a specified f_0 , the MMSE method is used to simultaneously

*As shown in [105], outdoor channels exhibit a PLE that does not have a strong frequency dependence – most of the frequency dependence is captured in the first meter of free space propagation. However, indoor channels, as shown here, have a PLE that is much more frequency dependent and are more lossy as frequency increases.

solve for the two model parameters b and n that minimize σ . The CIF model has a similar form as the ABG model (both have a frequency term, distance term, and constant intercept term) but only requires two model parameters instead of three, while also including the close-in free space leverage point for maintaining a physical tie to the transmitter [105, 114]. The CIF closed-form expressions for the best fit model parameters are given in Appendix A.

A *CIF XPD factor (CIFX)* model naturally follows, similar to the CIX and ABGX models for estimating path loss with cross-polarized antennas over multiple frequencies. The CIFX model equation is provided in (4.7):

$$\text{PL}^{\text{CIFX}}(f, d)[\text{dB}] = \text{FSPL}(f, d_0) + 10n \left(1 + b \left(\frac{f - f_0}{f_0} \right) \right) \log_{10} \left(\frac{d}{d_0} \right) + \text{XPD}[\text{dB}] + X_{\sigma}^{\text{CIFX}}, \text{ where } d_0 = 1 \text{ m} \quad (4.7)$$

where the n and b values found for the co-polarized CIF model and the same f_0 parameter are used to solve for the XPD that minimizes σ via MMSE. The closed-form expressions for optimizing the CIFX model parameters are similar to the CIX and ABGX models and are provided in Appendix A. It is important to note that the single frequency CI model (4.1) can also be used as a multi-frequency path loss model, while requiring only a single parameter, PLE [105].

The large-scale path loss models and parameters presented in the following chapter will be useful for determining capacity and for modeling communication system performance, in addition to determining deployment approaches. Co-channel interference is one of the most important factors to consider when designing a wireless system and network, and the large-scale models to follow in this report can be used to estimate and analyze interference from multiple sources [115, 116]. Estimating bit error rates (BER) for indoor office environments is also vital in order to understand how actual deployments will perform [117]. Shadowing or the large-scale signal fluctuations around the mean path loss is also necessary to understand for radio-system design, and researchers were able to estimate and predict shadowing relatively well for an indoor office environment at 900 MHz and 1900 MHz in the early 1990's [118]. The same approach may also be applicable for simulations at mmWave frequencies.

Chapter 5

Path Loss Model Parameters and Analysis

Single frequency and multi-frequency path loss models and parameters are explained and studied in the following chapter. The distances d in the models to follow are the 3D T-R separation distances from the measurements. Additionally, both co- and cross-polarized path loss models and combined polarization path loss models are given for directional and omnidirectional cases. For combining the polarization measurements, the co- and cross-polarized measurements were lumped into one dataset. For omnidirectional models, the measurements for co- and cross-polarized antennas for the same identical locations were considered *separate*, since full antenna sweeps were conducted across large portions of the azimuth and elevation planes to synthesize omnidirectional path loss at one location for a specific polarization configuration.

5.1 Directional Path Loss Models for Co- and Cross-Polarized Antennas

Directional path loss models are useful for modeling systems at mmWaves that may use directional antennas for arbitrary direction pointing, beam steering, or beam combining techniques [119, 120]. Previous work at 28, 38, 60, and 73 GHz in outdoor environments provided insights into directional path loss models [6, 99, 105, 121–123]. Now, path loss models are given for 28 GHz and 73 GHz indoor channels.

The definitions for descriptors of the physical environments for directional path loss models are identical to those used in [105], and are given in Table 5.1. Figs. 5.1a and 5.1b display the directional path loss scatter plots and best fit CI models (4.1) at 28 GHz in LOS and NLOS environments for co-polarization (V-V) and cross-polarization (V-H) antenna configurations, respectively. Each plot also shows the *NLOS-best* CI path loss model (see Table 5.1) that considers only the strongest received power for each measured NLOS TX-RX location combination. For V-V antenna polarizations, the LOS PLE is 1.7 at 28 GHz and 1.6 at

Table 5.1: Path loss environment definitions for directional path loss models.

Setting	Description
LOS	Path loss determined for environments when TX and RX antennas are pointed at each other, aligned on boresight with no obstructions between them.
NLOS	Path loss determined for environments when TX and RX antennas are separated by obstructions and there is no clear optical path between the antennas. This scenario also includes the case where the TX and RX antennas have a clear line-of-sight path to one another, but the antennas are not aligned on boresight.
NLOS-best	Path loss determined for the unique antenna pointing angles (in the azimuth and elevation planes) resulting in the strongest received power for each specific TX-RX location combination. This results from the single strongest measured PDP from the <i>NLOS</i> data at each TX-RX location combination.

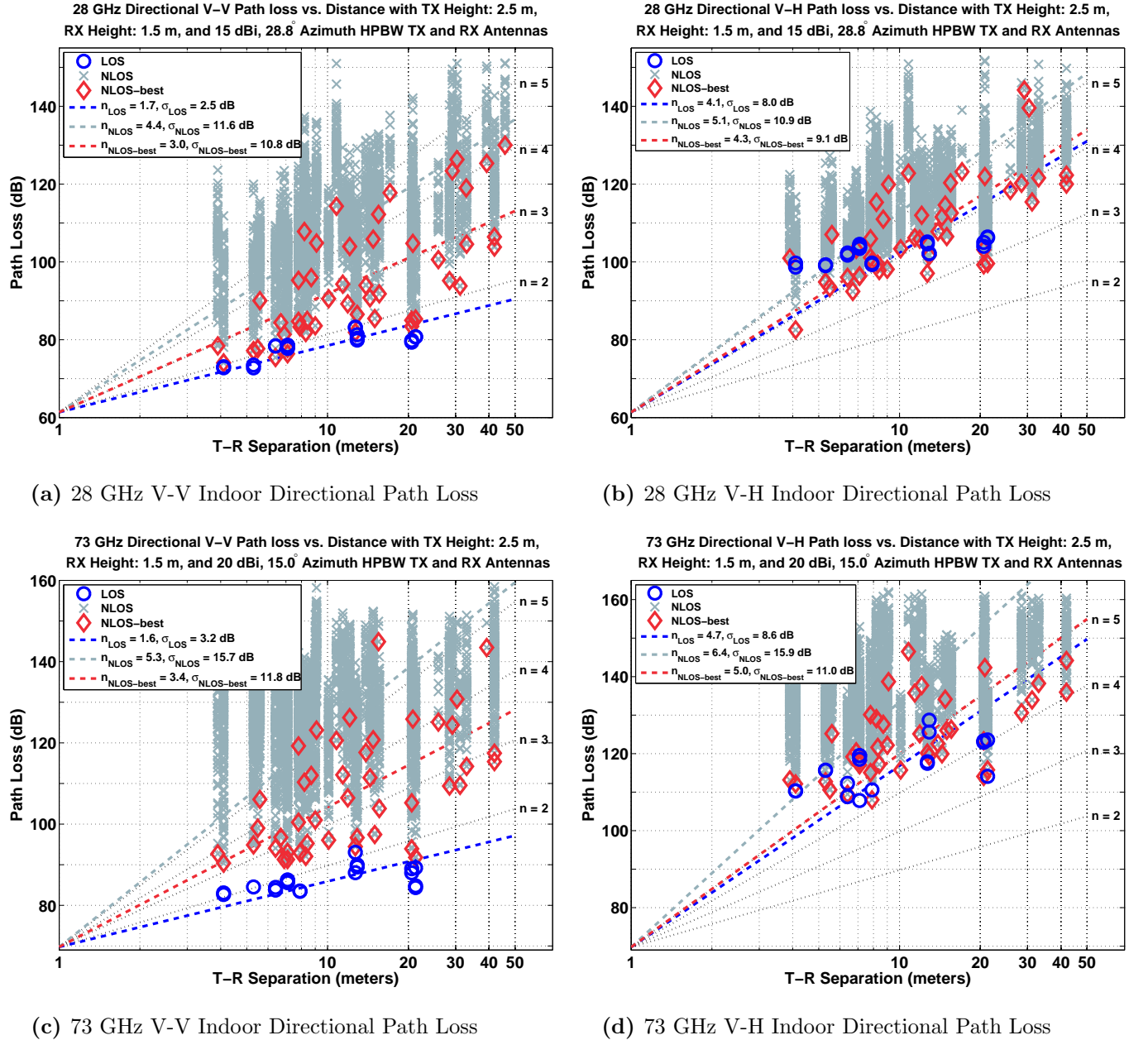


Fig. 5.1: Single frequency 28 GHz and 73 GHz directional CI ($d_0 = 1 \text{ m}$) indoor path loss models with TX antenna heights of 2.5 m and RX antenna heights of 1.5 m in a typical office environment for co- and cross-polarized TX and RX antennas. Each blue circle represents LOS path loss values, gray crosses represent NLOS path loss values measured at unique antenna pointing angles between the TX and RX (provided that signal could be received), and red diamonds represent angles with the lowest path loss measured for each NLOS TX-RX location combination. (a) 28 GHz V-V; (b) 28 GHz V-H; (c) 73 GHz V-V; and (d) 73 GHz V-H.

Table 5.2: Single frequency directional CI path loss model (4.1) parameters with $d_0 = 1$ m for 28 GHz and 73 GHz indoor channels with TX heights of 2.5 m and RX heights of 1.5 m for V-V and V-H antenna polarization configurations. The 28 GHz TX and RX antennas had 15 dBi (28.8° azimuth HPBW) of gain and the 73 GHz TX and RX antennas had 20 dBi (15° azimuth HPBW) of gain. “Freq.” stands for carrier frequency and “Pol.” stands for TX-RX antenna polarization configuration. The LOS distances ranged from 4.6 m to 21.3 m and the NLOS distances ranged from 3.9 m to 45.9 m.

Single Frequency Directional CI Path Loss Models for $d_0 = 1$ m							
Freq.	Pol.	LOS		NLOS		NLOS-best	
		PLE	σ [dB]	PLE	σ [dB]	PLE	σ [dB]
28 GHz	V-V	1.7	2.5	4.4	11.6	3.0	10.8
	V-H	4.1	8.0	5.1	10.9	4.3	9.1
73 GHz	V-V	1.6	3.2	5.3	15.7	3.4	11.8
	V-H	4.7	8.6	6.4	15.9	5.0	11.0

Table 5.3: Single frequency directional CIX path loss model (4.2) parameters with $d_0 = 1$ m for 28 GHz and 73 GHz indoor channels with TX heights of 2.5 m and RX heights of 1.5 m for V-H antenna polarization configurations. The 28 GHz TX and RX antennas had 15 dBi (28.8° azimuth HPBW) of gain and the 73 GHz TX and RX antennas had 20 dBi (15° azimuth HPBW) of gain. “Freq.” stands for carrier frequency and “Pol.” stands for TX-RX antenna polarization configuration.

Single Frequency Directional CIX Path Loss Model Parameters for $d_0 = 1$ m										
Freq.	Pol.	LOS			NLOS			NLOS-Best		
		$n_{(V-V)}$	XPD [dB]	σ [dB]	$n_{(V-V)}$	XPD [dB]	σ [dB]	$n_{(V-V)}$	XPD [dB]	σ [dB]
28 GHz	V-H	1.7	24.7	2.6	4.4	9.1	9.6	3.0	14.0	8.7
73 GHz	V-H	1.6	31.4	4.6	5.3	14.3	13.2	3.4	18.4	8.7

Table 5.4: Single frequency directional FI path loss model (4.3) parameters for 28 GHz and 73 GHz indoor channels with TX heights of 2.5 m and RX heights of 1.5 m for both V-V and V-H antenna polarization configurations. The 28 GHz TX-RX antennas had 15 dBi (28.8° azimuth HPBW) of gain and the 73 GHz TX-RX antennas had 20 dBi (15° azimuth HPBW) of gain. “Ant. Pol.” stands for antenna polarization.

Single Frequency Directional FI Path Loss Model Parameters										
Frequency	Ant. Pol.	LOS			NLOS			NLOS-best		
		α [dB]	β	σ [dB]	α [dB]	β	σ [dB]	α [dB]	β	σ [dB]
28 GHz	V-V	68.3	1.0	2.0	81.6	2.6	10.6	54.1	3.7	10.7
	V-H	94.8	0.8	1.6	92.7	2.3	8.0	73.0	3.3	8.7
73 GHz	V-V	79.6	0.7	2.3	114.0	1.3	11.3	75.6	2.9	11.7
	V-H	101.1	1.6	4.6	120.5	1.7	9.0	100.6	2.3	8.2

73 GHz, both less than the theoretical free space PLE of 2, and virtually identical at both frequencies, indicating that the indoor mmWave propagation channel experiences constructive interference from ground and ceiling bounce reflections and a waveguide effect down hallways and corridors that has a PLE that is not frequency dependent. The same phenomena were reported at lower microwave and Ultra-High Frequency (UHF) frequencies in indoor environments [21, 124]. Table 5.1 shows that by using the strongest single beam combination between the TX and RX at a NLOS location, the signal level is greatly improved (PLE is reduced) when compared to arbitrary beam pointing. This improvement is more prominent at 73 GHz, where the path loss is much greater (PLE = 5.3) for arbitrary pointing beams, and is reduced to PLE = 3.4 for the single best beam formation between the TX and RX antennas.

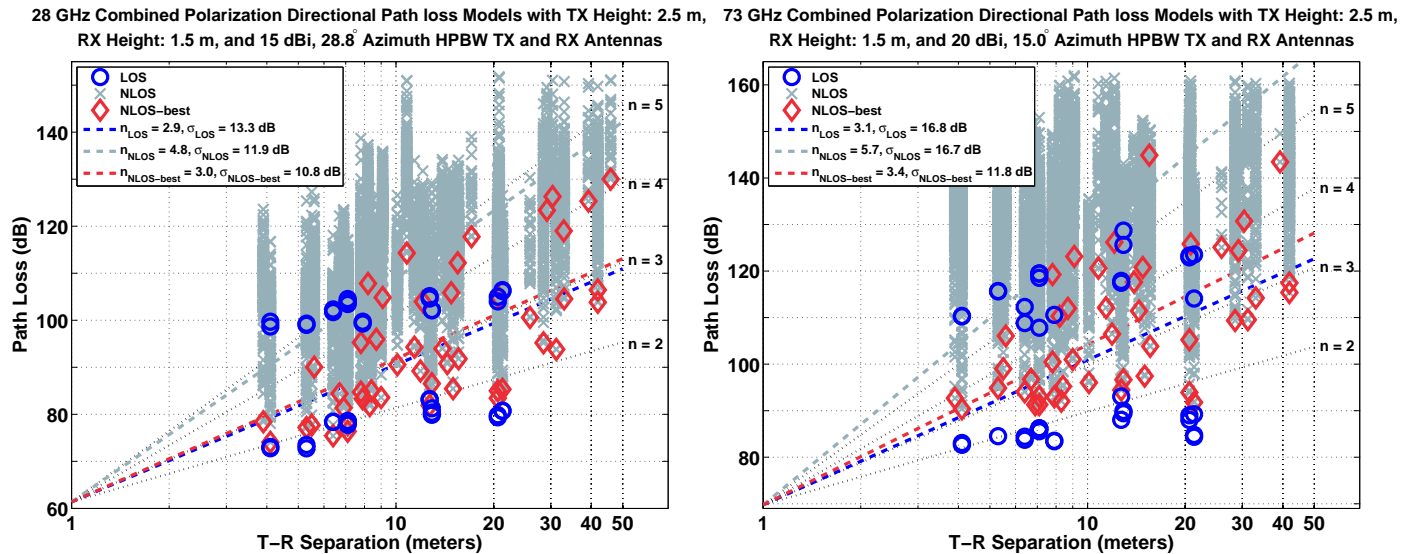
The 28 GHz LOS V-H CIX directional path loss model (4.2) indicates an XPD factor of 24.7 dB for cross-polarized antennas indicating that strong discrimination exists between cross-polarized signals in LOS environments [14, 22, 24, 80, 107]. The CI LOS PLE (n) at 28 GHz for V-H is 4.1, much greater than the 28 GHz V-V CI model PLE (1.7), shown in Table 5.2 and Table 5.3 for 3D T-R separation distances d . For NLOS environments, the CI PLE is 4.4 and 5.1 for the V-V and V-H antenna polarization configurations, respectively. This indicates significant de-polarization effect in NLOS indoor environments at 28 GHz, and

Table 5.5: 28 GHz and 73 GHz multi-frequency directional path loss model parameters for the CI, CIX, CIF, CIFX, ABG, and ABGX models for LOS, NLOS, and NLOS-Best environments and scenarios. The CIX, CIFX, and ABGX cross-polarized models use the corresponding parameters found for their respective co-polarized models to find the XPD factor in dB that minimizes σ . “Pol.” stands for polarization configuration (either V-V or V-H).

28 GHz and 73 GHz Multi-Frequency Directional LOS Path Loss Model Parameters						
	Pol.	PLE	XPD			σ
CI	V-V	1.7	-			2.9 dB
CIX	V-H	1.7	28.1 dB			4.7 dB
	Pol.	n	b	f_0	XPD	σ
CIF	V-V	1.7	-0.07	52 GHz	-	2.9 dB
CIFX	V-H	1.7	-0.07	52 GHz	28.1 dB	5.0 dB
	Pol.	α	β	γ	XPD	σ
ABG	V-V	0.9	43.6	1.8	-	2.1 dB
ABGX	V-H	0.9	43.6	1.8	27.4 dB	4.9 dB
28 GHz and 73 GHz Multi-Frequency Directional NLOS Path Loss Model Parameters						
	Pol.	PLE	XPD			σ
CI	V-V	4.9	-			14.6 dB
CIX	V-H	4.9	11.3 dB			13.3 dB
	Pol.	n	b	f_0	XPD	σ
CIF	V-V	4.8	0.19	50 GHz	-	13.9 dB
CIFX	V-H	4.8	0.19	50 GHz	11.6 dB	11.8 dB
	Pol.	α	β	γ	XPD	σ
ABG	V-V	1.9	27.5	4.3	-	11.1 dB
ABGX	V-H	1.9	27.5	4.3	8.9 dB	8.7 dB
28 GHz and 73 GHz Multi-Frequency Directional NLOS-Best Path Loss Model Parameters						
	Pol.	PLE	XPD			σ
CI	V-V	3.2	-			11.5 dB
CIX	V-H	3.2	16.0 dB			9.6 dB
	Pol.	n	b	f_0	XPD	σ
CIF	V-V	3.2	0.13	50 GHz	-	11.3 dB
CIFX	V-H	3.2	0.13	50 GHz	16.1 dB	9.0 dB
	Pol.	α	β	γ	XPD	σ
ABG	V-V	3.3	11.1	3.2	-	11.2 dB
ABGX	V-H	3.3	11.1	3.2	16.2 dB	8.8 dB

is further emphasized by the XPD factor of 9.1 dB determined from (4.2), which is substantially less than the 24.7 dB XPD factor found for 28 GHz LOS indoor mmWave channels. Similar results were noticed for the 73 GHz indoor channel, where LOS environments indicate an XPD factor of 31.4 dB, but only 14.3 dB for NLOS environments.

Tables 5.2 and 5.3 show the CI (4.1) and CIX (4.2) path loss model parameters, respectively, with $d_0 = 1$ m at 28 GHz and 73 GHz in the indoor environments. Results in Table 5.2 are slightly different than those initially published in [103] due to more stringent noise thresholding described in [105]. The 28 GHz and 73 GHz LOS PLEs for V-V are 1.7 and 1.6, respectively, due to constructive interference, and the shadow fading (SF) standard deviations for V-V and V-H measurements at the two bands are approximately 3 dB and 8 dB for the CI models, respectively. The 73 GHz NLOS CI model shows a much larger shadow fading standard deviation that is approximately 16 dB for V-V and V-H configurations, indicating much larger fluctuations in received signal strength around the mean received power over all T-R separation distances, regardless of whether the polarizations are matched. The NLOS CIX models at 28 GHz and 73 GHz are better estimates of cross-polarization path loss compared to the CI model as they have smaller SF values (1.3 dB and 2.7 dB less) than the CI V-H path loss models.



(a) 28 GHz combined polarization indoor directional path loss (b) 73 GHz combined polarization indoor directional path loss

Fig. 5.2: Single frequency combined polarization 28 GHz and 73 GHz directional CI ($d_0 = 1$ m) indoor path loss models with TX antenna heights of 2.5 m and RX antenna heights of 1.5 m in a typical office environment for LOS and NLOS environments. Each blue circle represents LOS path loss values, gray crosses represent NLOS path loss values measured at unique antenna pointing angles between the TX and RX (provided that signal could be received), and red diamonds represent angles with the lowest path loss measured for each NLOS TX-RX location combination. (a) 28 GHz; (b) 73 GHz.

Table 5.4 shows the parameters for the FI model, where it can be seen that α values can vary widely compared to free space path loss at 1 m in LOS for V-V at 28 GHz (68.3 dB) and 73 GHz (79.6 dB), and in some environments by more than 20 to 30 dB. This reveals that the FI model lacks a physical link to the transmitted signal power, and does not physically model what actually happens in a practical LOS or NLOS system where there are no obstructions, e.g., free space conditions, in the first several meters of propagation. Furthermore, the slope β of the mean least-squares fit line in (4.3) are close to or less than free space ($\beta = 2$) in NLOS environments for both 28 GHz and 73 GHz with co- and cross-polarized antennas, which does not properly predict the intuitive fact that NLOS cross-polarized signals undergo much heavier attenuation with distance than free space signals. This underscores the lack of intuition provided by the FI model when trying to reconcile the physical effects of polarization and environmental loss with distance. The lack of measurements or data samples is often the cause of α and β values that make no physical sense [105, 112]. Post-processing methods that employ different thresholding techniques can also significantly change the parameters in the very sensitive FI model [105]. The results in Tables 5.2–5.4 indicate that there is little value in using a model with more than 1 parameter, since the difference in standard deviation between the CI and FI models is very small, in most cases less than 1 dB.

With regards to the CI path loss model, the 73 GHz band is more lossy than the 28 GHz band in indoor NLOS environments. The 73 GHz band is initially 8.4 dB more lossy in the first meter of propagation, but as seen in Table 5.2, at greater distances the PLE is 0.9 greater for the V-V case, indicating that 73 GHz NLOS propagation experiences an additional 9 dB per decade of distance more path loss beyond the first meter of propagation compared to 28 GHz. The smaller 73 GHz wavelength results in more diffuse scattering and greater shadowing in the physical surroundings that weakens signals when compared to 28 GHz in the NLOS indoor office environment. The carpeted floors, cubicle sound proofing, and textured wall surfaces all likely contribute to greater attenuation due to diffusion at 73 GHz.

The CI model of (4.1) provides the benefit of simple comparisons of measurements across many frequency bands using just one parameter, since frequency dependent effects of the model are primarily contained in the 1 m FSPL where a substantial amount of loss occurs, while the PLE value represents the environmental effects of propagation that are less sensitive to frequency than the loss in the first meter. For outdoor mmWave channels, the PLE was found to be only slightly sensitive to frequency [105]. However, Tables 5.2, 5.3, and 5.4 show that for indoor channels, the environment provides additional and substantial frequency-dependent loss beyond the first meter of free space propagation. Variations of the CI model as described in [3, 105, 114] and presented here with the CIF model (4.6) allow the PLE to vary with frequency.

Table 5.5 provides the 28 GHz and 73 GHz directional multi-frequency CI, CIX, CIF, CIFX, ABG and ABGX path loss models for the directional LOS, NLOS, and NLOS-Best environments and scenarios. The multi-frequency XPD models are used for cross-polarized measurements, as they result in lower standard deviation and better minimization of σ compared to a non-XPD model, as noticed in the differences in σ when comparing the CI cross-polarized (V-H) model and CIX model for directional single frequency measurements in Table 5.2. The standard deviations for the three multi-frequency models are within 1 dB or so of each other in LOS and NLOS environments, as shown in Table 5.5. The CI and CIF models have identical slope parameters (PLE and n , respectively) in LOS (1.7) and NLOS-Best (3.2) environments and differ by only 0.1 in NLOS. In the NLOS-Best environment, the ABG model has a similar slope parameter to the CI and CIF models (α) where the CI (PLE) and CIF (n) parameters are 3.2 and ABG α is 3.3. The CIX, CIFX, and ABGX LOS XPD models show that there is large polarization isolation in LOS environments, where the XPD factors are greater than 27 dB for each. The ABG and ABGX models have lower standard deviations in a majority of scenarios when compared to the CIF and CIFX model, but not by much, except for the arbitrary pointing NLOS situation, where the ABG and ABGX models have a 2.8 dB and 3.1 dB lower standard deviation compared to the CIF and CIFX models. Note, however, the standard deviations for all three models are large, over 11 dB in NLOS cases, and well within measurement error of 1-2 dB in typical measurement campaigns. The ABGX and ABG models do not have a free space path loss leverage point, thus these models are not tied to true transmitted power, and as shown in [114], are much less stable or accurate compared to models that use a free-space reference distance when used outside the measurement range for which the model parameters were optimized for. The standard deviations of multi-frequency path loss models for similar environments in Table 5.5 show just how closely the different directional path loss models predict path loss, with little difference in standard deviations observed for most cases (a majority differ by less than 1 dB). The small differences in standard deviation suggest that the simpler, physics-based CI, CIX, and CIF models may be better suited for closed-form analysis as well as standards work when developing future mmWave indoor networks. As shown subsequently, the omnidirectional path loss models reveal even smaller differences between the CIF and ABG models.

5.2 Omnidirectional Path Loss Models for Co- and Cross-polarized Antennas

While the preceding directional path loss models are useful for wireless systems using directional antennas [120, 125, 126], standards bodies rely on omnidirectional path loss models to allow arbitrary antenna patterns to be used for simulations. In order to synthesize an omnidirectional path loss model from directional measurements, the antenna radiation patterns used during measurements must be de-embedded or removed from the results [127]. This can be achieved by summing received powers (in the linear scale) from unique, non-overlapping pointing angle directional measurements (from adjacent angular bins) and after subtracting the antennas gains, as implemented in [128, 129]. Since the measurement sweeps included antenna pointing directions separated by approximately one antenna HPBW in the azimuth and elevation planes, the summed directions are virtually orthogonal to each other in space, thereby avoiding over-counting

Table 5.6: Path loss definitions for omnidirectional path loss models.

Setting	Description
LOS	Path loss when there is a clear optical path between the TX and RX.
NLOS	Path loss when the TX and RX are separated by obstructions and there is no clear optical path between the TX and RX.

of received power or multipath energy [105, 129]. The raw omnidirectional path loss data used to generate the omnidirectional path loss models presented in this report are provided in tabular form in Appendix B.

The same method used in [128] was performed on the 28 GHz and 73 GHz indoor directional data, where for each TX-RX location pair, the omnidirectional path loss between the i^{th} TX location and the j^{th} RX location was recovered from individual and non-overlapping pointing angle received powers in the azimuth and elevation planes following [105, 128, 129]:

$$PL_{i,j}[\text{dB}] = Pt_{i,j}[\text{dBm}] - 10 \log_{10} \left[\sum_z \sum_y \sum_x \sum_w Pr_{i,j}(\theta_{r_w}, \phi_{r_x}, \theta_{t_y}, \phi_{t_z}) [\text{mW}] \right] \quad (5.1)$$

where θ_t and ϕ_t are the TX antenna pointing angles in the azimuth and elevation planes, respectively, θ_r and ϕ_r are the RX antenna pointing angles in the azimuth and elevation planes, where $Pt_{i,j}$ is the omnidirectional transmit power, and the $Pr_{i,j}$ values are the individual directional received powers from the unique pointing angles, with the antenna gains removed. The individual directional received powers were found from the PDPs recorded for each unique antenna pointing angle, where power is the area under each PDP. To ensure consistency with the omnidirectional path loss models presented in [105, 128], the same descriptors of physical environments for omnidirectional path loss models were used in this article and are defined in Table 5.6.

Figs. 5.3a – 5.3d display the CI ($d_0 = 1$ m) and FI omnidirectional scatter plots and path loss models at 28 GHz and 73 GHz for LOS and NLOS indoor office environments with separate V-V and V-H antenna polarization configurations. Table 5.7 lists the omnidirectional CI and FI path loss model parameters. Table 5.8 gives the CIX model parameters for the V-H omnidirectional cross-polarization scenarios. The tables show that in LOS environments, the V-V CI model omnidirectional PLE is 1.1 and 1.3 at 28 GHz and 73 GHz, respectively. Similar to the directional V-V CI models, the omnidirectional PLEs are less than theoretical free space path loss ($n = 2$), and not surprisingly show significantly lower loss than the directional LOS channels. In NLOS environments for V-V antennas, the omnidirectional PLE is 2.7 and 3.2 at 28 GHz and 73 GHz, respectively, showing higher path loss at 73 GHz than at 28 GHz, likely due to increased diffuse scattering with shorter wavelengths at higher frequencies [7]. The NLOS directional V-V PLEs are 4.4 and 5.3 at 28 GHz and 73 GHz, respectively, compared to the omnidirectional values of 2.7 and 3.2 at 28 GHz and 73 GHz, respectively, showing that omnidirectional antennas would capture more energy than directional antennas, but offer less link margin (less distance range due to smaller antenna gain) [105, 129].

For cross-polarized antennas, the 28 GHz LOS (V-H PLE = 2.5) and NLOS (V-H PLE = 3.6) CIX omnidirectional models resulted in attenuation XPD factors of 14.0 dB and 10.4 dB, respectively. The LOS and NLOS V-H PLEs for 73 GHz were 3.5 (XPD = 22.8 dB) and 4.5 (XPD = 15.4 dB), respectively, also indicating higher path loss at 73 GHz as well as greater polarization discrimination. Similar to the directional path loss models, for omnidirectional LOS channels, a lumped cross-polarization attenuation factor used in (4.2) yields a simple CIX path loss model with lower standard deviation (better fit) about the distance-dependent mean path loss compared to a traditional CI model for cross-polarized path loss data.

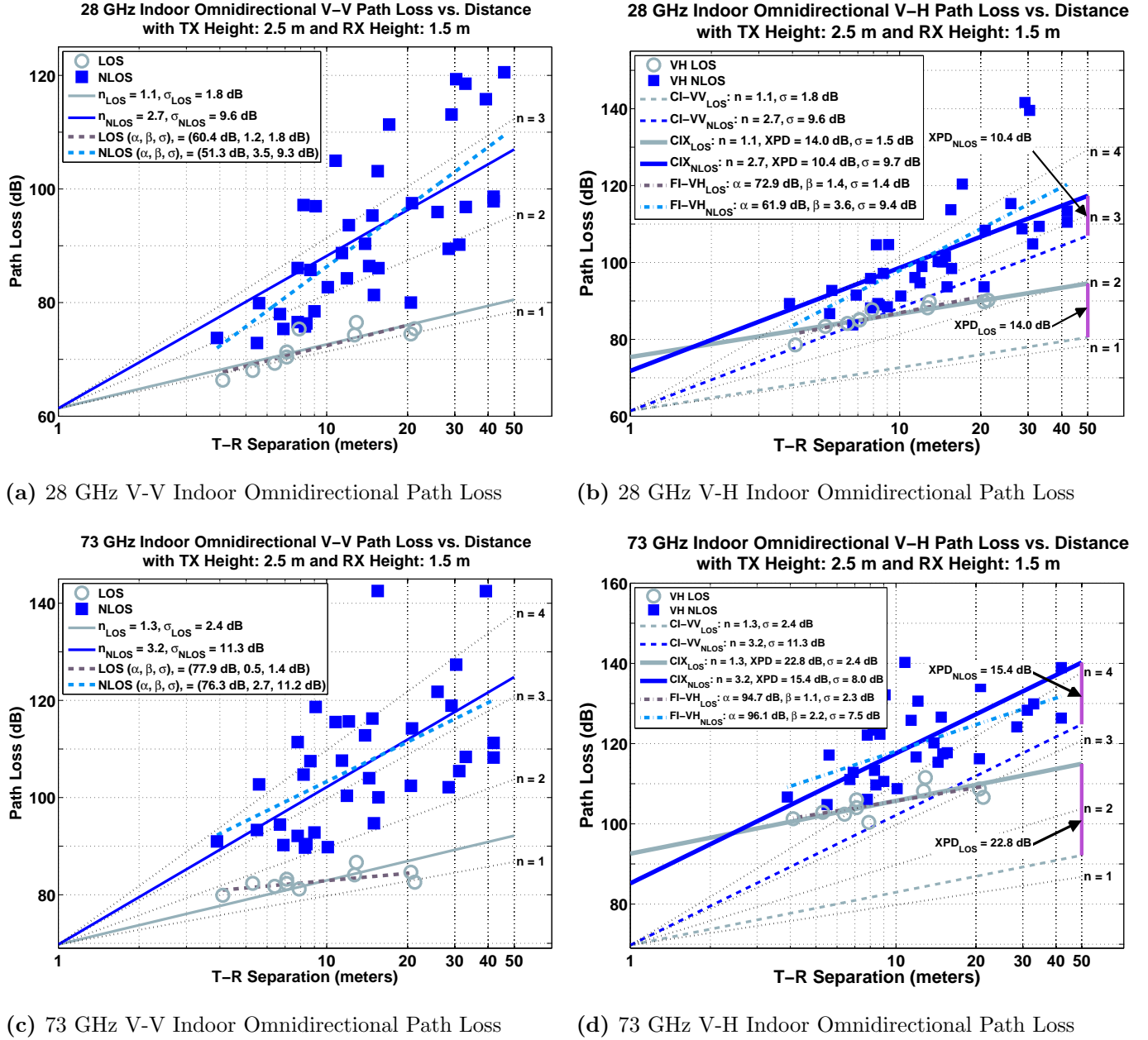


Fig. 5.3: Single frequency 28 GHz and 73 GHz indoor omnidirectional CI ($d_0 = 1$ m) and FI path loss scatter plots and models with TX antenna heights of 2.5 m and RX antenna heights of 1.5 m in a typical office environment for co- and cross-polarized TX and RX antennas. Gray circles represent LOS omnidirectional path loss values and solid blue squares represent NLOS omnidirectional path loss values, using Eq. (5.1). (a) 28 GHz V-V; (b) 28 GHz V-H; (c) 73 GHz V-V; and (d) 73 GHz V-H.

The 14.0 dB and 10.4 dB omnidirectional XPD factors in LOS and NLOS at 28 GHz may not be sufficient for indoor systems to implement simultaneous dual antenna polarization transmission [130, 131], depending on the modulation scheme used, but interference cancellation methods might allow simultaneous transmissions of cross-polarized signals and should be further investigated. The 73 GHz LOS and NLOS XPD factors of 22.8 dB and 15.4 dB are substantially larger than those at 28 GHz and yield remarkable polarization isolation for 73 GHz diversity polarization transmission in indoor environments. The results show that NLOS environments experience higher path loss which results in a lower XPD factor compared to LOS [23].

Table 5.7: Single frequency omnidirectional CI path loss model parameters with $d_0 = 1$ m and FI path loss model parameters for 28 GHz and 73 GHz indoor propagation channels with TX heights of 2.5 m and RX heights of 1.5 m for both V-V and V-H antenna polarization configurations for LOS and NLOS environments. “Freq.” stands for carrier frequency, “Pol.” stands for TX-RX antenna polarization configuration, and “Env.” stands environment.

Single Frequency Omnidirectional CI and FI Path Loss Models							
Freq.	Pol.	Env.	CI: $d_0 = 1$ m		FI		
			PLE	σ [dB]	α [dB]	β	σ [dB]
28 GHz	V-V	LOS	1.1	1.8	60.4	1.2	1.8
		NLOS	2.7	9.6	51.3	3.5	9.3
	V-H	LOS	2.5	3.0	72.9	1.4	1.4
		NLOS	3.6	9.4	61.9	3.6	9.4
73 GHz	V-V	LOS	1.3	2.4	77.9	0.5	1.4
		NLOS	3.2	11.3	76.3	2.7	11.2
	V-H	LOS	3.5	6.3	94.7	1.1	2.3
		NLOS	4.5	9.7	96.1	2.2	7.5

Table 5.8: Single frequency omnidirectional CIX path loss model parameters with $d_0 = 1$ m for 28 GHz and 73 GHz indoor channels with TX heights of 2.5 m and RX heights of 1.5 m for V-H antenna polarization configurations. The 28 GHz TX and RX antennas had 15 dBi (28.8° azimuth HPBW) of gain and the 73 GHz TX and RX antennas had 20 dBi (15° azimuth HPBW) of gain. “Freq.” stands for carrier frequency and “Pol.” stands for TX-RX antenna polarization configuration

Single Frequency Omnidirectional CIX Path Loss Models for $d_0 = 1$ m							
Freq.	Pol.	LOS			NLOS		
		$n_{(V-V)}$	XPB [dB]	$\sigma_{(XPB)}$ [dB]	$n_{(V-V)}$	XPB [dB]	$\sigma_{(XPB)}$ [dB]
28 GHz	V-H	1.1	14.0	1.5	2.7	10.4	9.7
73 GHz	V-H	1.3	22.8	2.4	3.2	15.4	8.0

Table 5.9: 28 GHz and 73 GHz multi-frequency omnidirectional path loss model parameters for the CI, CIX, CIF, CIFX, ABG, and ABGX models for LOS and NLOS environments. The CIX, CIFX, and ABGX cross-polarized models use the corresponding parameters found for their respective co-polarized models to find the XPD factor in dB that minimizes σ . “Pol.” stands for polarization configuration (either V-V or V-H).

28 GHz and 73 GHz Multi-Frequency Omnidirectional LOS Path Loss Model Parameters						
	Pol.	PLE	XPB			σ
CI	V-V	1.2	-			2.3 dB
CIX	V-H	1.2	18.4 dB			5.7 dB
	Pol.	n	b	f_0	XPB	σ
CIF	V-V	1.2	0.18	51 GHz	-	2.1 dB
CIFX	V-H	1.2	0.18	51 GHz	18.4 dB	4.8 dB
	Pol.	α	β	γ	XPB	σ
ABG	V-V	0.9	26.8	2.6	-	1.8 dB
ABGX	V-H	0.9	26.8	2.6	18.2 dB	4.7 dB
28 GHz and 73 GHz Multi-Frequency Omnidirectional NLOS Path Loss Model Parameters						
	Pol.	PLE	XPB			σ
CI	V-V	2.9	-			10.9 dB
CIX	V-H	2.9	12.6 dB			10.4 dB
	Pol.	n	b	f_0	XPB	σ
CIF	V-V	3.0	0.21	50 GHz	-	10.4 dB
CIFX	V-H	3.0	0.21	50 GHz	12.7 dB	9.3 dB
	Pol.	α	β	γ	XPB	σ
ABG	V-V	3.1	1.3	3.8	-	10.3 dB
ABGX	V-H	3.1	1.3	3.8	12.9 dB	9.0 dB

The FI omnidirectional models at 28 GHz and 73 GHz have intercept α values in LOS environments, that are several dB offset from theoretical free space at 1 m at both 28 GHz and 73 GHz. The very low LOS β slope value of 0.5 at 73 GHz shows the extreme sensitivity of the FI model and how the model parameters defy physical interpretation (where a PLE value less than 1 in the CI model implies gain with increasing distance). This illustrates the caution that must be taken to extrapolate the FI model outside of the measurement range.

The small LOS β slope values may be due to the small sample set of LOS locations. The strength of the CI model compared to the FI model is that it only requires a single parameter to accurately predict path loss, and models FSPL up until the reference distance d_0 , giving an accurate physically-based reference anchor point for estimating LOS path loss. Choosing $d_0 = 1$ m is convenient and sensible because FSPL exists in the first meter of propagation, before the transmitted wave encounters most walls, ceilings, and floors that cause reflections, scattering, or diffraction loss (blockage). If more LOS omnidirectional locations were measured, we would expect the FI β slope to converge to the CI PLE values in LOS environments (1.1 and 1.3 at 28 GHz and 73 GHz, respectively), as shown in the 28 GHz LOS V-V model displayed in Fig. 5.3a, where the CI PLE and FI β values are within 0.1 of each other.

Some researchers may correctly argue that the two parameter FI model (4.3) reduces the shadow factor (standard deviation) about the mean path loss line compared to the shadow factor found using the single parameter CI path loss model (4.1). That argument may be true in very sparse measurement data sets, but when enough measurements are taken, the standard deviations are generally within a fraction of a dB for both models as seen in Table 5.7 and [105]. From this study, Table 5.7 shows that there are only three cases (all cross-polarized cases) where the standard deviation is more than 1 dB different between the CI and FI omnidirectional models: the 73 GHz V-H NLOS case, and the 28 GHz and 73 GHz LOS V-H cases, where the standard deviation is different by 2.2 dB, 1.6 dB and 4.0 dB, respectively, yet we have already established that the CIX model with an XPD term in (4.2) is a better estimator of path loss for V-H antenna configurations than either the CI or FI model (Compare Table 5.7 and Table 5.8). Furthermore, the CIX model provides nearly identical standard deviations compared to the FI model, where the maximum difference in standard deviation of both models over all frequencies and environments is 0.5 dB. Important points to consider are that all models here have rather large standard deviations (8 dB or so), so selecting a simpler path loss model that has fewer parameters with less than a dB of difference in standard deviation assures virtually identical modeling accuracy in the face of typical measurement error, physical database error, and cable and calibration fluctuations [105]. Further, in the absence of measured data, the physical foundation of the CI family of path loss models allows for extrapolation beyond the 3D T-R separation distances of the measurements because they are physically-anchored to a known free space (true transmitter power) path loss value and distance, whereas the FI models are only valid over the measured 3D T-R separation distances.

A key observation from the omnidirectional path loss data is the pronounced increase in the PLE for 73 GHz compared to 28 GHz, for any given environment due to the increased loss experienced by signals with smaller wavelengths. The standard deviation also increased at 73 GHz compared to 28 GHz for the omnidirectional models, as seen in Tables 5.7–5.8. Due to a more stringent noise thresholding algorithm used here and described in [105], values in Table 5.7 are slightly different than those presented in [103]. The differences in the CI, FI, and CIX model standard deviations in Tables 5.7–5.8 are 1 dB or less in a majority of the different environments and scenarios, while the overall standard deviations are much larger (greater than 8 dB in NLOS cases).

Multi-frequency omnidirectional path loss model parameters for co- and cross-polarized antennas are given in Table 5.9. Similar to the directional models, the standard deviations for each omnidirectional multi-frequency model with specific polarizations (CI, CIF, and ABG) are within 1 dB for the corresponding LOS and NLOS environments (σ is between 1.8 dB and 2.3 dB in LOS and between 10.3 dB and 10.9 dB in NLOS for the CI, CIF, and ABG models). The FSPL anchoring point is an advantage in the CI and CIF

Table 5.10: Single frequency combined polarization directional path loss models at 28 GHz and 73 GHz for LOS, NLOS, and NLOS-Best scenarios.

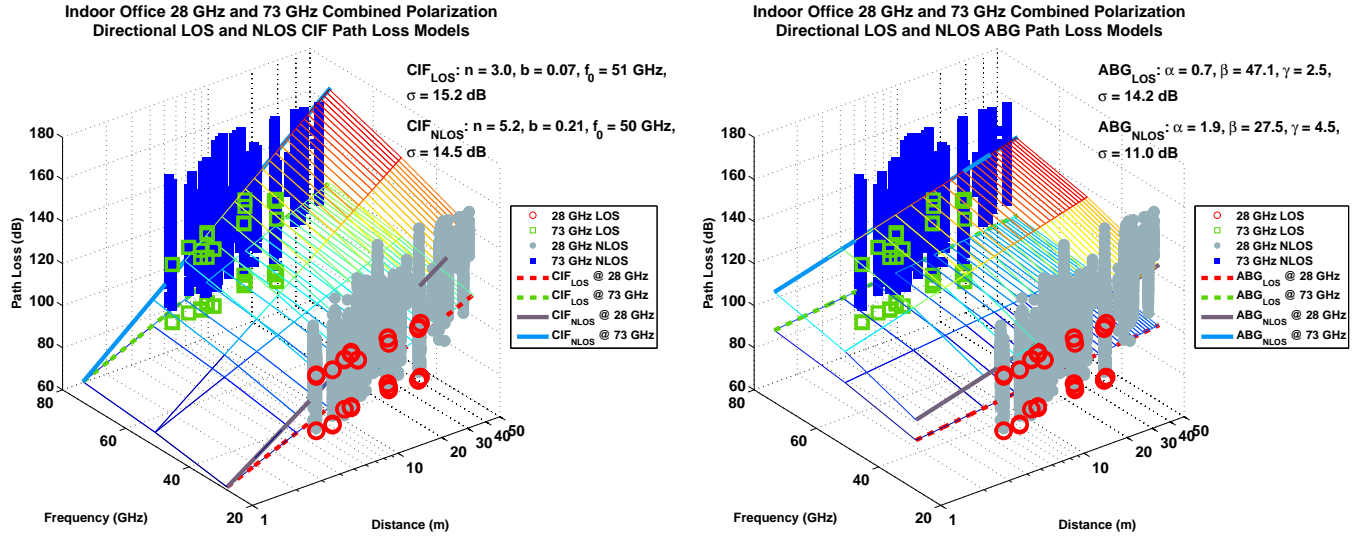
Single Frequency Combined Polarization Directional CI Path Loss Models with $d_0 = 1$ m									
Freq.	LOS			NLOS			NLOS-best		
	PLE	σ [dB]		PLE	σ [dB]		PLE	σ [dB]	
28 GHz	2.9	13.3		4.8	11.9		3.0	10.8	
73 GHz	3.1	16.8		5.7	16.7		3.4	11.8	
Single Frequency Combined Polarization Directional FI Path Loss Models									
Freq.	LOS			NLOS			NLOS-best		
	α [dB]	β	σ [dB]	α [dB]	β	σ [dB]	α [dB]	β	σ [dB]
28 GHz	$4.1 \text{ m} \leq d \leq 21.3 \text{ m}$			$3.9 \text{ m} \leq d \leq 45.9 \text{ m}$					
	83.4	0.8	12.2	87.5	2.4	10.1	54.1	3.7	10.7
73 GHz	$4.1 \text{ m} \leq d \leq 21.3 \text{ m}$			$3.9 \text{ m} \leq d \leq 41.9 \text{ m}$					
	94.5	0.7	15.8	117.8	1.3	11.7	75.6	2.9	11.7

models, where in LOS environments, the CI PLE and CIF n values are identical (1.2), and 2.9 and 3.0 in NLOS, respectively. The advantage of the two parameter CIF model over the single parameter CI model is the frequency weighting term b on the PLE, to account for frequency-dependent loss with distance, which results in a lower standard deviation of 2.1 dB (CIF) compared to 2.3 dB (CI) in LOS, and 10.4 dB (CIF) compared to 11.5 dB (CI) in NLOS. The CI and CIF models for specific polarizations are always well within 1 dB of the three parameter ABG model standard deviation, such that 1 dB reduction in standard deviation is less than an order of magnitude than the standard deviation of either model, thus motivating the use of a simpler model (e.g. fewer parameters) given the lack of substantial model improvement when using more parameters and a non-physically-based model [105]. From Table 5.9, it is also seen that the LOS standard deviations are 5.7 dB, 4.8 dB, and 4.7 dB for the CIX, CIFX, and ABGX models, respectively.

5.3 Directional Path Loss Models for Combined Polarizations

In order to characterize path loss regardless of polarization, the co- and cross-polarization measurements were lumped into a single dataset for 28 GHz and 73 GHz to generate large-scale path loss models that may be applied to arbitrary antenna polarizations, a common practice in standards bodies. Table 5.10 provides the single frequency directional path loss models using combined co- and cross-polarization measurement data at 28 GHz and 73 GHz for the LOS, NLOS, and NLOS-Best scenarios. When considering the single strongest pointing angle combination for each specific T-R separation distance, as compared with arbitrary pointing angles in NLOS conditions, Table 5.10 shows that the PLE reduces by 18 dB and 13 dB per decade of distance for 28 GHz and 73 GHz, respectively. In LOS, the FI β values are lower than 1 (0.8 and 0.7 for 28 GHz and 73 GHz, respectively thus implying channel gain with distance) and thus lack a sensible intuitive explanation based on physics. In the NLOS-Best scenario, the β values are larger (3.7 and 2.9 at 28 GHz and 73 GHz, respectively) than the corresponding β values for the FI NLOS model (2.4 and 1.3 at 28 GHz and 73 GHz, respectively) also contradicting physical intuition for propagation as a function of distance when considering the lowest path loss measured for the best RX antenna pointing angle at each location.

Table 5.11 lists the 28 GHz and 73 GHz multi-frequency combined polarization directional path loss model parameters for the LOS, NLOS, and NLOS-Best scenarios. In all three scenarios, the CI PLE and CIF n values are identical, 3.0 in LOS, 5.2 in NLOS, and 3.2 for NLOS-Best. This result shows the consistency of using a FSPL anchor grounded in true physics for path loss modeling. The CIF model reduces the standard deviation only slightly in the NLOS and NLOS-Best scenarios, by only 1.0 dB and 0.2 dB respectively, and is identical in LOS (15.2 dB). The difference in 1.1 dB or 1.0 dB is much smaller than the actual standard



(a) Multi-frequency combined polarization directional CIF LOS and NLOS scatter plot

(b) Multi-frequency combined polarization directional ABG LOS and NLOS scatter plot

Fig. 5.4: 28 GHz and 73 GHz multi-frequency combined polarization CIF and ABG directional path loss models for LOS and NLOS environments. Red circles represent 28 GHz LOS directional path loss values, green squares represent 73 GHz LOS directional path loss values, solid gray circles represent 28 GHz NLOS directional path loss values, and solid blue squares represent 73 GHz NLOS directional path loss values for (a) CIF Model; (b) ABG Model.

deviation value of 15.5 dB (CI-NLOS) and 14.5 dB (CIF-NLOS) as shown in Table 5.11. For the ABG model, the α and β terms are seen to vary over a wide range of values that do not provide intuitive sense. Table 5.11 does show that the ABG model for LOS, NLOS, and NLOS-best has lower standard deviation than both the CI and CIF models, but the reduction is so small (a few dB to a fraction of a dB) compared to the overall standard deviation values which are all greater than 11 dB. Figs 5.4a and 5.4b show the LOS and NLOS CIF and ABG directional path loss models for combined polarizations. Note that the CIF model standard deviation is within 0.4 dB of the ABG model in the NLOS-Best scenario. For the NLOS arbitrary pointing angle case, the standard deviation for the ABG model is 3.5 dB smaller than the CIF model, reducing it from 14.5 dB to 11 dB through the use of three modeling parameters, but Table 5.11 shows that the ABG model parameters vary over a wide range without intuition of the physics, and in the other cases (LOS and NLOS-Best) the differences in standard deviation between the CIF and ABG models are less than a dB, less than an order of magnitude of standard deviation values of all models, and certainly in the measurement noise.

5.4 Omnidirectional Path Loss Models for Combined Polarizations

Using the synthesized omnidirectional path loss values described here, and given in Appendix B, omnidirectional path loss models were computed for single and multi-frequency cases at 28 GHz and 73 GHz with the co- and cross-polarized measurements lumped into a common dataset. Table 5.12 provides single frequency path loss model parameters at 28 GHz and 73 GHz and Figs. 5.5a and 5.5b display the corresponding 28 GHz and 73 GHz scatter plots. It is apparent that the 28 GHz and 73 GHz NLOS CI model standard deviation is within 1 dB of the NLOS FI model, well within measurement error, and less than an order of magnitude than the actual standard deviations, where the CI model requires only one parameter and uses a physically based FSPL anchoring point. The FI model 73 GHz LOS β slope value indicates channel amplification with distance (0.8). The FI model is limited as it is only valid over the measurement range of the data, which is

Table 5.11: 28 GHz and 73 GHz multi-frequency combined polarization directional path loss models for LOS, NLOS, and NLOS-Best scenarios.

28 GHz and 73 GHz Multi-Frequency Combined Polarization Directional CI Path Loss Models with $d_0 = 1$ m				
Env.	PLE	σ [dB]		
LOS	3.0	15.2		
NLOS	5.2	15.5		
NLOS-Best	3.2	11.5		
28 GHz and 73 GHz Multi-Frequency Combined Polarization Directional CIF Path Loss Models with $d_0 = 1$ m				
Env.	n	b	f_0	σ [dB]
LOS	3.0	0.07	51 GHz	15.2
NLOS	5.2	0.21	50 GHz	14.5
NLOS-Best	3.2	0.13	50 GHz	11.3
28 GHz and 73 GHz Multi-Frequency Combined Polarization Directional ABG Path Loss Models with $d_0 = 1$ m				
Env.	α	β	γ	σ [dB]
LOS	0.7	47.1	2.5	14.2
NLOS	1.9	27.5	4.5	11.0
NLOS-Best	3.3	11.1	3.2	11.2

between 4.1 m and 21.3 m in LOS at 28 GHz and 73 GHz, and 3.9 m to 45.9 m in NLOS at 28 GHz and 3.9 m to 41.9 m in NLOS at 73 GHz.

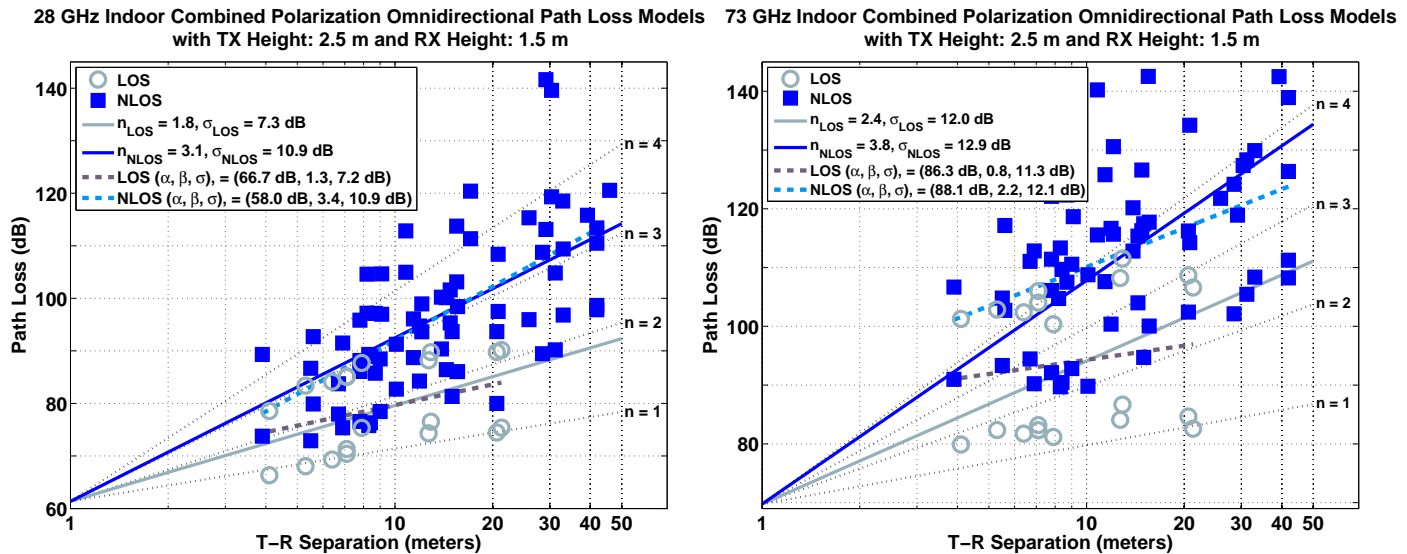
All co- and cross-polarized omnidirectional measurement data at 28 GHz and 73 GHz were combined and used to develop the combined polarization CI, CIF, and ABG omnidirectional multi-frequency path loss models as provided in Table 5.13. The CI and CIF models show stability with the use of a FSPL anchoring point grounded in true physics, such that the CI PLE and CIF n values are identical in LOS (2.1) and NLOS (3.4) environments. As observed for the co- and cross-polarized multi-frequency omnidirectional models, the omnidirectional CIF models using all co- and cross-polarized measurements also have lower standard deviations than the CI models, but only by 0.5 dB and 0.6 dB in LOS and NLOS environments, respectively, due to the model's second parameter, the frequency-dependent balancing term b . The three parameter ABG model has the lowest standard deviation in LOS and NLOS compared to the CI and CIF models, but by only a fraction of a dB in both environments (a very small improvement, considering the standard deviation for all models is about 12 dB). Comparatively, the standard deviation in LOS is 10.4 dB

Table 5.12: 28 GHz and 73 GHz single frequency combined polarization CI and FI omnidirectional path loss models for LOS and NLOS environments.

Single Frequency Combined Polarization Omnidirectional CI Path Loss Models with $d_0 = 1$ m						
Freq.	LOS			NLOS		
	PLE	σ [dB]		PLE	σ [dB]	
28 GHz	1.8	7.3		3.1	10.9	
73 GHz	2.4	12.0		3.8	12.9	
Single Frequency Combined Polarization Omnidirectional FI Path Loss Models						
Freq.	LOS			NLOS		
	α [dB]	β	σ [dB]	α [dB]	β	σ [dB]
28 GHz	4.1 m $\leq d \leq$ 21.3 m			3.9 m $\leq d \leq$ 45.9 m		
	66.7	1.3	7.2	58.0	3.4	10.9
73 GHz	4.1 m $\leq d \leq$ 21.3 m			3.9 m $\leq d \leq$ 41.9 m		
	86.3	0.8	11.3	88.1	2.2	12.1

Table 5.13: 28 GHz and 73 GHz multi-frequency combined polarization CI, CIF, and ABG omnidirectional path loss models for LOS and NLOS environments.

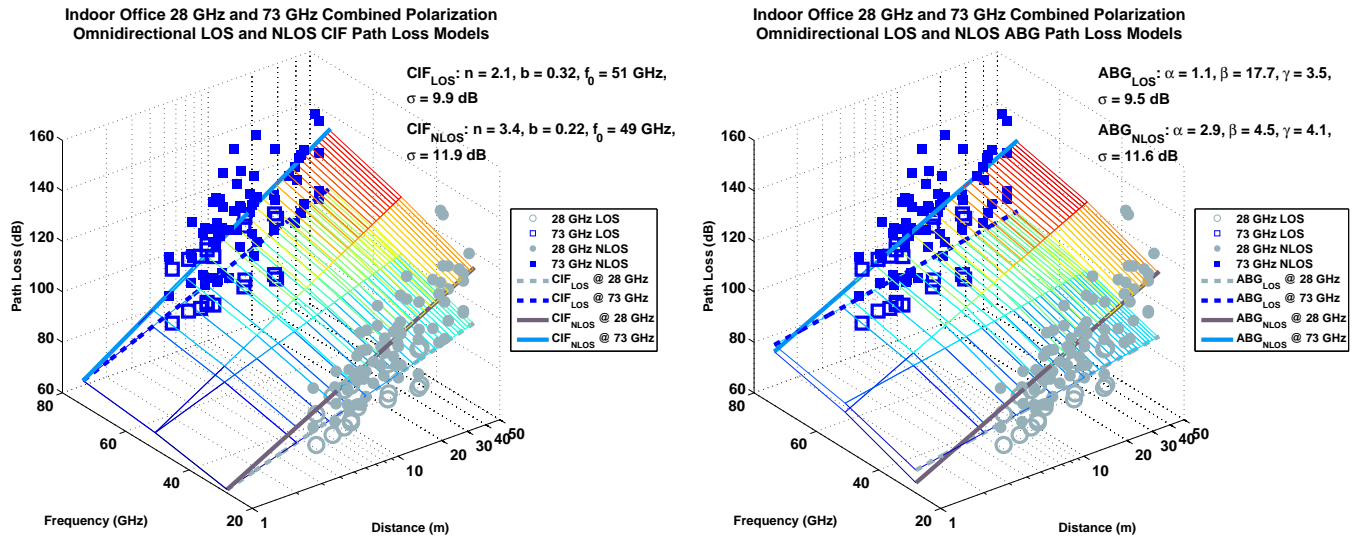
28 GHz and 73 GHz Multi-Frequency Combined Polarization Omnidirectional CI Path Loss Models with $d_0 = 1$ m				
Env.	PLE	σ [dB]		
LOS	2.1	10.4		
NLOS	3.4	12.5		
28 GHz and 73 GHz Multi-Frequency Combined Polarization Omnidirectional CIF Path Loss Models with $d_0 = 1$ m				
Env.	n	b	f_0	σ [dB]
LOS	2.1	0.32	51 GHz	9.9
NLOS	3.4	0.22	49 GHz	11.9
28 GHz and 73 GHz Multi-Frequency Combined Polarization Omnidirectional ABG Path Loss Models with $d_0 = 1$ m				
Env.	α	β	γ	σ [dB]
LOS	1.1	17.7	3.5	9.5
NLOS	2.9	4.5	4.1	11.6



(a) 28 GHz omnidirectional combined polarization path loss (b) 73 GHz omnidirectional combined polarization path loss

Fig. 5.5: 28 GHz and 73 GHz single frequency combined polarization CI and FI omnidirectional path loss models for LOS and NLOS environments. Gray circles represent LOS omnidirectional path loss values and solid blue squares represent NLOS omnidirectional path loss values for (a) 28 GHz; (b) 73 GHz.

for CI, 9.9 dB for CIF, and 9.5 dB for the ABG model, not a large difference for standard deviations that are already greater than 9 dB. Furthermore, the standard deviation in NLOS is 12.5 dB for CI, 11.9 dB for CIF, and 11.6 dB for the ABG model, also within measurement errors and typical cable loss variations or gain drift in typical measurements, and not a vast difference for already large standard deviations. Figs. 5.6a and 5.6b show the 3D scatter plots of omnidirectional LOS and NLOS path loss values and the corresponding CIF and ABG path loss models, where the CIF model is anchored by FSPL at 1 m. Both figures show a similar trend as path loss increases with frequency. The combined polarization omnidirectional path loss models given in Tables 5.12 and 5.13 also show comparable standard deviations in LOS and NLOS environments between the CI and FI single frequency models and the CI, CIF, and ABG multi-frequency models, where differences in standard deviations are less than an order of magnitude of the standard deviation, and less than or equal to 1 dB in all cases.



(a) Multi-frequency combined polarization omnidirectional CIF LOS and NLOS path loss

(b) Multi-frequency combined polarization omnidirectional ABG LOS and NLOS path loss

Fig. 5.6: 28 GHz and 73 GHz multi-frequency combined polarization CIF and ABG omnidirectional path loss model for LOS and NLOS environments. Gray circles represent 28 GHz LOS omnidirectional path loss values, blue squares represent 73 GHz LOS omnidirectional path loss values, solid gray circles represent 28 GHz NLOS omnidirectional path loss values, and solid blue squares represent 73 GHz NLOS omnidirectional path loss values for (a) CIF Model; (b) ABG Model.

From the large-scale path loss models and parameters shown above, it is apparent that the single frequency CI model does an excellent job in predicting indoor path loss at mmWave frequencies by using a single parameter. For multiple-frequency omnidirectional modeling, it is clear that indoor channels offer greater loss with distance at higher frequencies. The work above shows that the two parameter CIF model retains a physical link to the physics of propagation while reducing the standard deviation as compared to the CI model. The three parameter ABG model can typically obtain a fraction of a dB to a dB or two less standard deviation but at the expense of an additional parameter model and a lack of physical basis. Thus, the CIF model appears to be a good candidate for indoor large-scale path loss modeling over a wide range of mmWave frequencies.

This page is intentionally left blank.

Chapter 6

Time Dispersion Properties

6.1 MmWave Indoor Time Dispersion Properties

The time dispersion properties of wideband channels are generally characterized by RMS delay spread, as it is a good measure of the multipath time dispersion and coherence bandwidth nature of multipath channels, and an indication of the potential severity of intersymbol interference, depending on the signal's bandwidth [49, 132, 133]. To build power-efficient mmWave mobile communications systems with simple equalization, it was recently postulated that there could be advantages in searching for particular beam pointing directions that offer both minimum path loss and minimum multipath delay spread [120]. Physical layer design is often dictated by channel RMS delay spread and time dispersion characteristics, and analysis of such properties can provide valuable information for the design of indoor mmWave communications systems. All RMS delay spread and temporal statistics presented in this section are for typical LOS and NLOS environments.

The RMS delay spread is defined as the square root of the second moment of a PDP [49]:

$$\sigma_\tau = \sqrt{\overline{\tau^2} - (\bar{\tau})^2} \quad (6.1)$$

where,

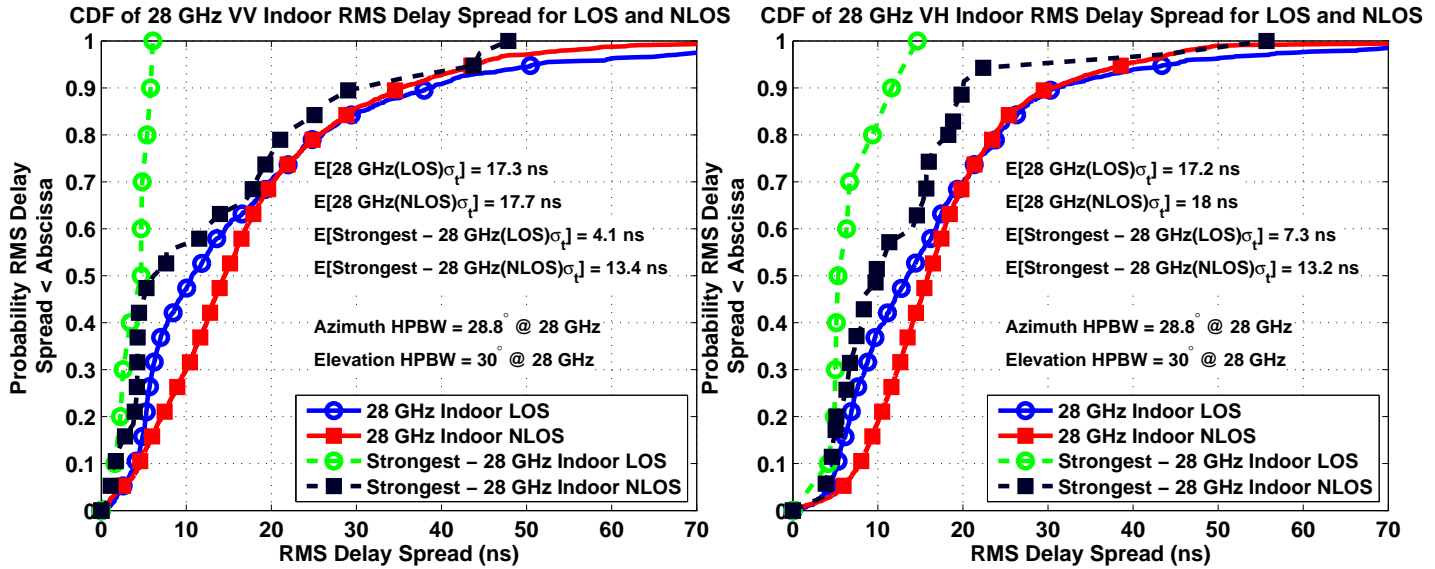
$$\bar{\tau} = \frac{\sum_k P(\tau_k)\tau_k}{\sum_k P(\tau_k)} \quad (6.2)$$

$$\overline{\tau^2} = \frac{\sum_k P(\tau_k)\tau_k^2}{\sum_k P(\tau_k)} \quad (6.3)$$

In Eqs. (6.1)-(6.3), σ_τ is the RMS delay spread, $P(\tau_k)$ is the received power (in mW) at the delay bin centered at τ_k , $\bar{\tau}$ is the mean excess delay which is the first moment of a PDP, and $\overline{\tau^2}$ is the second central moment of a PDP. We captured a PDP at each unique antenna pointing angle between the TX and RX in the azimuth and elevation planes, for all measured TX and RX pointing angles between each TX-RX location combination.

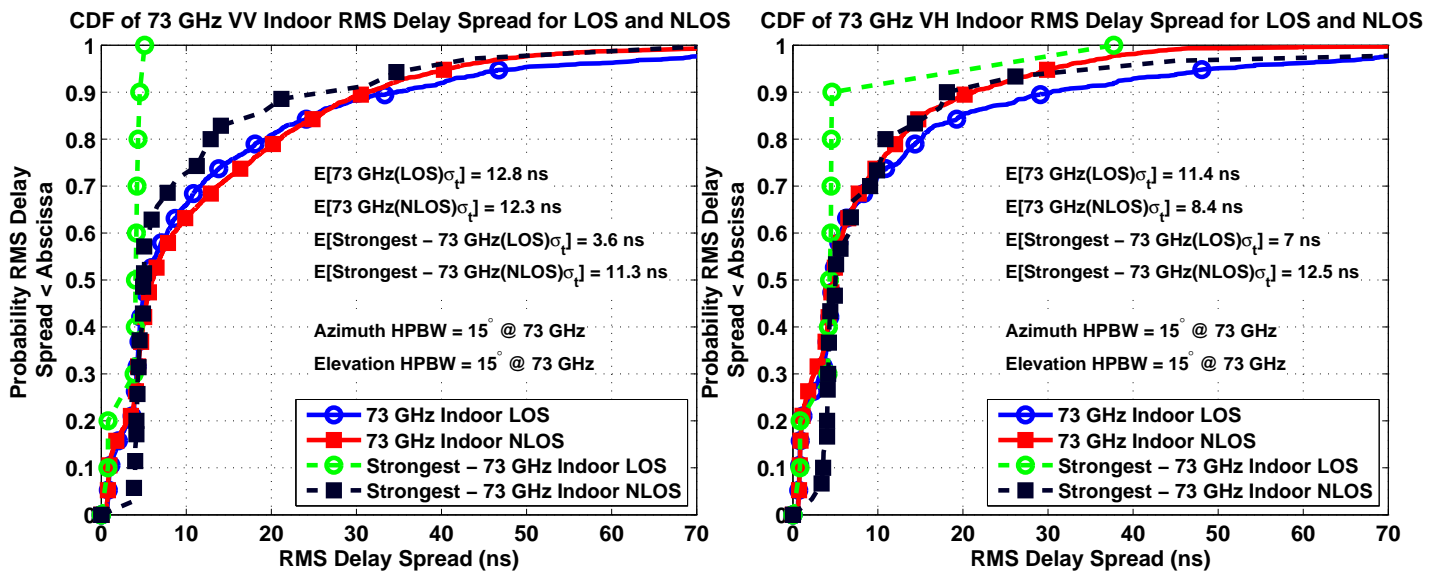
6.1.1 Multipath Time Dispersion Statistics for Co- or Cross-Polarized Antennas

Figs. 6.1a and 6.1b show the cumulative distribution functions (CDF) for the RMS delay spreads of the PDPs measured over all pointing angles at 28 GHz for V-V and V-H antenna polarization configurations, respectively. Both figures show that 90% of the measured RMS delay spreads in both LOS and NLOS



(a) 28 GHz V-V indoor directional RMS delay spread

(b) 28 GHz V-H indoor directional RMS delay spread



(c) 73 GHz V-V indoor directional RMS delay spread

(d) 73 GHz V-H indoor directional RMS delay spread

Fig. 6.1: 28 GHz and 73 GHz arbitrary pointing angle (directional) RMS delay spread CDFs for TX antenna heights of 2.5 m RX antenna heights of 1.5 m in a typical indoor office environment for co- and cross-polarized TX and RX antennas in LOS and NLOS environments. The T-R separation distances ranged from 3.9 m to 45.9 m. (a) 28 GHz V-V; (b) 28 GHz V-H; (c) 73 GHz V-V; and (d) 73 GHz V-H.

environments are less than 40 ns for all measured arbitrary pointing angles. The NLOS locations were generally found to have greater RMS delay spreads than LOS locations, since obstructions in NLOS locations blocked or severely attenuated the direct path, causing multipath to arrive at the receiver over a larger propagation time interval. In LOS environments, the LOS component was much stronger than reflected or scattered paths, leading to lower RMS delay spreads. Similar trends were observed in propagation measurements below 6 GHz, conducted by Hashemi *et al.* in two office environments [133]. The mean RMS delay spread was smaller in LOS environments (where the direct path was dominant) compared to NLOS environments (where the direct path was obstructed). Similar RMS delay spread statistics at 60 GHz were reported by Geng *et al.*, where RMS delay spreads in a NLOS hall were larger than in either a LOS hall or corridor [74].

The measured mean RMS delay spreads at 28 GHz are between 17 ns and 18 ns in all environments and polarization combinations (as summarized in Table 6.1), which in general are larger than the mean RMS delay spreads between 8 ns and 13 ns at 73 GHz. Similar results were reported by Yang *et al.* where the mean RMS delay spreads at 58 GHz (8 ns to 14 ns) were about 50% lower than those at 2.25 GHz (20 ns to 28 ns) due to high penetration loss caused by walls, such that multipath components observed at 58 GHz came mostly from reflected waves confined to the room, while the reflected waves from neighboring rooms at 2.25 GHz had significantly longer delays [134].

The results reported in Table 6.1 and displayed in Fig. 6.1 show that the minimum measured RMS delay spreads are all lower than 1 ns, while the maximum delay spread values observed are all greater than 100 ns, regardless of frequency or environment. Maximum RMS delay spreads were measured to be 98 ns at 58 GHz [68], between 100 ns and 150 ns at 1.5 GHz [18], and up to 250 ns at 850 MHz [135]. At 28 GHz and 73 GHz the maximum measured RMS delay spreads in LOS environments are smaller than in NLOS environments for most cases, with the only exception for the 73 GHz V-H antenna polarization scenario, where the maximum RMS delay in a NLOS environment is larger than that in a LOS environment (21.6 ns greater), as noticed in Table 6.1 and Fig. 6.1. Additionally, standard deviations of RMS delay spreads in LOS and NLOS environments at both frequencies are less than 18 ns. There was no clear trend observed between the minimum RMS delay spreads and standard deviations of RMS delay spreads in relation to environment, polarization, and frequency.

We also studied the RMS delay spreads when considering the single best unique antenna pointing angles between the TX and RX locations that resulted in the strongest received power, for each TX-RX location combination measured. For all LOS and NLOS locations measured, the CDF of the RMS delay spreads for the angles with the strongest received power (lowest path loss) are also provided in the subfigures in Fig. 6.1. For both 28 GHz and 73 GHz, and for the co- and cross-polarized antenna configurations, the mean RMS delay spreads when considering the single strongest pointing angles are less as compared to the mean RMS delay spreads over all unique antenna pointing angles measured for all locations, except for 73 GHz V-H NLOS. This is particularly true for LOS environments, where Fig. 6.1 shows that the strongest beams offer much smaller RMS delay spread than arbitrary pointing beams, although the difference is not as great for NLOS channels. For cross-polarized NLOS channels, however, the best beam can sometimes increase the multipath dispersion. As shown in Table 6.1 and Fig. 6.1, the strongest beams in NLOS locations resulted in greater standard deviations than in LOS locations, which is not observed when considering arbitrary pointing angles. Table 6.1 shows that the minimum values of RMS delay spreads when considering the best beam are in general within 4 ns regardless of frequency, environment, and antenna polarization, indicating that the best beam can simultaneously minimize path loss and RMS delay spread. These observations indicate the opportunity to minimize multipath time dispersion with high gain, narrowbeam, directional, co-polarized antennas for indoor mmWave communications systems when exploiting the strongest pointing angle beams between the TX and RX.

Figs. 6.1c and 6.1d show similar RMS delay spread CDF curves at 73 GHz for both V-V and V-H antenna polarization configurations. The figures indicate that 90% of RMS delay spreads in both LOS and NLOS

indoor environments are less than 30 ns. Little difference in RMS delay spread is noticed between LOS and NLOS locations for both V-V and V-H antenna configurations.

At both 28 GHz and 73 GHz, the mean RMS delay spreads were significantly reduced when considering the single strongest co-polarized pointing angle combinations between the TX and RX antennas, where in V-V LOS cases the mean RMS delay spreads were reduced from 17.3 ns to 4.1 ns, and from 12.8 ns to 3.6 ns, for 28 GHz and 73 GHz respectively. Somewhat smaller reductions in RMS delay spreads were seen in NLOS for the V-V case, where the mean RMS delay spreads were reduced from 17.7 ns to 13.4 ns, and from 12.3 ns to 11.3 ns, for 28 GHz and 73 GHz, respectively, when considering the strongest pointing angles. The smaller RMS delay spreads are due to the strongest received power angle combinations containing a main LOS component and very weak multipath at large excess delays (or none at all). The largest difference in mean RMS delay spread for co-polarized antennas when comparing arbitrary pointing angles to the strongest pointing angles is in the LOS environment, where beamforming and beam steering algorithms [136, 137] will be useful in reducing RMS delay spread by searching for the strongest received power pointing angles. As seen in Table 6.1, the V-H scenario at 28 GHz was very similar to the V-V case with mean RMS delay spreads reduced by 9.9 ns and 1.0 ns in LOS and NLOS respectively; however, 73 GHz mean RMS delay spreads reduced by 4.4 ns in LOS and increased by 4.1 ns in NLOS for the V-H case.

In all cases for the 28 GHz and 73 GHz measurements, the cross-polarized antenna RMS delay spreads were larger than co-polarized antenna RMS delay spreads (see Table 6.1), likely a result of additional energy captured based on wave de-polarization from the TX to RX in the indoor mmWave environment, and was also noticed in [22, 24, 107] where cross-polarized omnidirectional antennas experienced 3-4 ns larger mean and maximum RMS delay spreads compared to co-polarized antennas.

Table 6.1 summarizes the mean, standard deviation, minimum, and maximum measured RMS delay spread statistics calculated from the 28 GHz and 73 GHz measurements for co- and cross-polarized antenna configurations in LOS and NLOS environments. Compared to 28 GHz, the 73 GHz band had smaller observed RMS delay spreads, similar to results reported in [138] when comparing RMS delay spreads of 2 GHz, 5 GHz, and 17 GHz. The time dispersion values given in Table 6.1 are marginally different than those in [103] as a result of a newer more stringent noise thresholding method described in [105].

6.1.2 Multipath Time Dispersion Statistics for Combined-Polarized Antennas

Time dispersion characteristics are also important for modeling applications that will employ arbitrary antenna polarization configurations such as mobile handsets that are constantly changing orientations. Figs. 6.2a and 6.2b show the CDFs for the RMS delay spreads for combined polarization measurements at 28 GHz and 73 GHz, respectively, for PDPs measured over all arbitrary pointing angles and also for the single strongest pointing angles for each TX-RX location combination. Table 6.2 summarizes the mean RMS delay spreads from the figures and includes the standard deviation, minimum, and maximum measured RMS delay spread statistics calculated at 28 GHz and 73 GHz for combined antenna polarizations for LOS and NLOS environments.

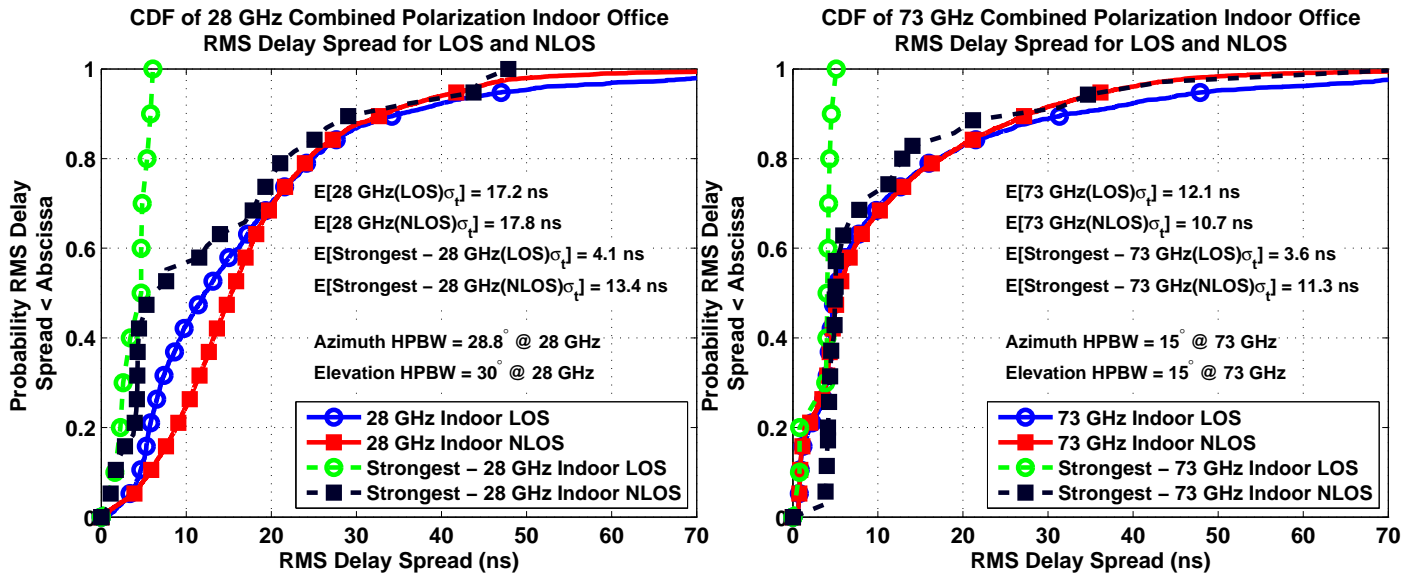
Figs. 6.2a and 6.2b indicate that 90% of RMS delay spreads for combined antenna polarizations, regardless of environment, are less than 35 ns and 30 ns at 28 GHz and 73 GHz, respectively. From Table 6.1 and Table 6.2, there is no distinguishable difference between co-polarization (V-V) and combined polarization in the RMS delay spread statistics. The RMS delay spread statistics at 28 GHz are, in general, slightly greater than the corresponding statistics at 73 GHz. The measured mean RMS delay spreads for combined polarizations at 28 GHz are 17.2 ns (LOS) and 17.8 ns (NLOS), and are larger than the mean RMS delay spreads of 12.1 ns (LOS) and 10.7 ns (NLOS) at 73 GHz. Irrespective of frequency and environment, the minimum RMS delay spreads are all less than 2 ns and the maximum RMS delay spreads are all less than

Table 6.1: Comparison of mean, standard deviation, and maximum RMS delay spreads at 28 GHz and 73 GHz for V-V and V-H antenna polarization combinations in LOS and NLOS indoor propagation environments. “Ant. Pol.” means TX-RX antenna polarization and “Env.” indicates the environment type of the RX locations.

RMS Delay Spreads Over All Arbitrary Angles					
Ant. Pol.	Env.	28 GHz			
		μ (ns)	σ (ns)	Min. (ns)	Max. (ns)
V-V	LOS	17.3	18.0	0.7	134.4
	NLOS	17.7	13.8	0.6	198.5
	LOS-Best	4.1	1.6	1.6	6.1
	NLOS-Best	13.4	13.1	0.9	47.9
V-H	LOS	17.2	14.5	0.9	126.4
	NLOS	18.0	10.9	0.6	128.1
	LOS-Best	7.3	3.5	4.2	14.6
	NLOS-Best	13.2	10.8	3.5	55.7
Ant. Pol.	Env.	73 GHz			
		μ (ns)	σ (ns)	Min. (ns)	Max. (ns)
V-V	LOS	12.8	16.9	0.6	101.9
	NLOS	12.3	14.2	0.5	142.0
	LOS-Best	3.6	1.5	0.8	5.1
	NLOS-Best	11.3	14.4	3.7	73.4
V-H	LOS	11.4	17.5	0.5	143.8
	NLOS	8.4	10.6	0.5	122.2
	LOS-Best	7.0	10.9	0.8	37.7
	NLOS-Best	12.5	22.5	2.2	122.2

Table 6.2: Comparison of mean, standard deviation, and maximum RMS delay spreads at 28 GHz and 73 GHz for combined antenna polarizations in LOS and NLOS indoor propagation environments. “Env.” indicates the environment type of the RX locations.

RMS Delay Spreads Over All Arbitrary Angles For Combined Polarizations				
Env.	28 GHz			
	μ (ns)	σ (ns)	Min. (ns)	Max. (ns)
LOS	17.2	16.4	0.7	134.4
NLOS	17.8	12.5	0.6	198.5
LOS-Best	4.1	1.6	1.6	6.1
NLOS-Best	13.4	13.1	0.9	47.9
Env.	73 GHz			
	μ (ns)	σ (ns)	Min. (ns)	Max. (ns)
LOS	12.1	17.2	0.5	143.8
NLOS	10.7	13.0	0.5	142.0
LOS-Best	3.6	1.5	0.8	5.1
NLOS-Best	11.3	14.4	3.7	73.4



(a) 28 GHz combined polarization indoor directional RMS delay spread

(b) 73 GHz combined polarization indoor directional RMS delay spread

Fig. 6.2: 28 GHz and 73 GHz arbitrary pointing angle (directional) combined polarization RMS delay spread CDFs for TX antenna heights of 2.5 m RX antenna heights of 1.5 m in a typical indoor office environment for LOS and NLOS scenarios. The T-R separation distances ranged from 3.9 m to 45.9 m. (a) 28 GHz combined polarization; (b) 73 GHz combined polarization.

200 ns. A majority of standard deviations of RMS delay spread are around 15 ns. The minimum value and standard deviation of RMS delay spreads show no clear dependence on environment, polarization, and frequency.

Similar to statistics for separate polarizations, the RMS delay spreads are lower when only considering the single strongest antenna pointing orientation between the TX and RX at 28 GHz and 73 GHz, most notably where Table 6.2 and Fig. 6.2 shows in LOS environments that the mean RMS delay spread reduces from 17.2 ns to 4.1 ns at 28 GHz (in LOS) and from 12.1 ns to 3.6 ns at 73 GHz (in LOS). From Table 6.2 it is apparent that the V-V antenna polarization corresponds to the maximum observed RMS delay spreads at 28 GHz in LOS (134.4 ns) and NLOS (198.5 ns) environments for combined polarizations (as observed in Table 6.1). The same observation is made at 73 GHz in NLOS (142.0 ns), however, in the LOS case at 73 GHz, the V-H antenna polarization in LOS (143.8 ns) corresponds to the maximum observed RMS delay spread for combined antenna polarizations.

Work in [120] suggests a simple algorithm to find the best beam directions that can simultaneously minimize both RMS delay spread and path loss (finding the best paths that simultaneously have both strong SNR and very small multipath time dispersion). By selecting a beam with both low RMS delay spread and low path loss, relatively high SNR can be achieved at the RX using directional antennas without complicated equalization, meaning that low latency single carrier (wideband) modulations may be a viable candidate for future mmWave wireless communications systems [131]. The measured values presented in Tables 6.1–6.2 and Figs. 6.1 and 6.2 give insight to the range of multipath channel parameters for arbitrary pointing co-, cross-, or combined-polarized antennas, as well as for the best TX and RX antenna pointing angles that result in the lowest path loss/link attenuation.

Chapter 7

Conclusion

This report provides the world's first comprehensive study of indoor channels at 28 GHz and 73 GHz using different antenna polarizations and combined polarizations to generate large-scale path loss models and time delay spreads for the development of 5G standards at 28 GHz and 73 GHz. Directional and omnidirectional path loss models and directional multipath RMS delay spread values are presented, yielding insight into mmWave indoor office propagation characteristics. Extensive analysis shows that for mmWave indoor channels, large-scale path loss over distance and frequency may be modeled with virtually no sacrifice in accuracy by using simple close-in (CI) free space reference distance models with just one or two parameters that ensure a physical tie to the transmitter power, rather than using existing 3GPP and WINNER floating intercept (FI) models that have no tie to the transmitted power, lack intuition, and require more modeling parameters. The closed-form expressions for optimizing existing and newly proposed large-scale path loss model parameters are given in Appendix A, the raw omnidirectional data used to create the large-scale path loss models in this report are tabulated in Appendix B, and standard deviations of each large-scale path loss model are tabulated for side-by-side comparison in Appendix C.

Single frequency directional path loss models were provided using the 1 m close-in free space reference distance (CI), close-in reference distance with XPD factor (CIX), and floating-intercept (FI) forms. The CI path loss models showed that for co-polarized antennas, constructive interference due to waveguiding and reflections resulted in nearly identical LOS PLEs of 1.7 and 1.6 for 28 GHz and 73 GHz, respectively, smaller than theoretical FSPL ($n = 2$), suggesting that LOS PLEs are independent of frequency. Path loss observed in NLOS environments had much greater attenuation (44 dB ($n = 4.4$) and 53 dB ($n = 5.3$) per decade of distance for 28 GHz and 73 GHz, respectively) than in LOS environments; however, the high attenuation was significantly reduced (resulting in $n = 3.0$ at 28 GHz and $n = 3.4$ at 73 GHz), when considering the best TX and RX antenna pointing angles that resulted in the maximum received power at each measured location. The shadowing factor increased from 28 GHz to 73 GHz (2.5 dB to 3.2 dB in LOS, and 11.6 dB to 15.7 dB in NLOS), indicating more variability in large-scale shadowing at higher mmWave frequencies, most likely due to increased diffuse scattering, greater diffraction loss, and weaker reflections. The directional PLEs for the V-H antenna polarization configurations indicated significant de-polarization in NLOS indoor environments at both 28 GHz and 73 GHz. For LOS channels, large directional XPD factors of 24.7 dB and 31.4 dB were found for V-H scenarios at 28 GHz and 73 GHz, respectively, and showed that there was large isolation between co- and cross-polarized transmission when using high-gain directional horn antennas. Larger fluctuations in received signal strength about the distance-dependent mean path loss were observed at 73 GHz in NLOS environments for cross-polarized directional antennas (15.9 dB) compared to 28 GHz cross-polarized directional antennas (10.9 dB). The CIX model was shown to be a useful and simple path loss model for cross-polarized antenna systems, and was shown to improve (reduce) the standard deviation compared to the CI model, most notably by 4.0 dB and 2.7 dB in LOS and NLOS environments, respectively,

at 73 GHz. The FI path loss model is sensitive to the post-processing methods and was shown to lack a physical basis for radio propagation. The directional CI path loss model better explained the physical propagation at 28 GHz and 73 GHz compared to the FI model, where the β slope values were 1.0 and 0.7 for V-V in LOS at 28 GHz and 73 GHz, respectively, suggesting the nonsensical situation of ultra-low loss or channel gain with distance using the FI model. The better stability and physical sensibility of the CI model is due to the fixation of received power at 1 m from the transmitter, which is based in physics [105], as well as the inherent frequency dependence of path loss in the first meter of propagation.

For the combined co- and cross-polarized measurements, which are the most representative of arbitrary (e.g. random) antenna orientations in an indoor wireless network, the single frequency directional LOS PLEs were 2.9 and 3.1 for 28 GHz and 73 GHz, respectively, noticeably greater than FSPL ($n = 2$). NLOS environments experienced greater attenuation for the combined data, with PLEs of 4.8 and 5.7 at 28 GHz and 73 GHz, respectively, showing a higher path loss with increased distance at higher frequencies in the indoor channel (this frequency dependence on PLE is not as prominent in outdoor channels [105]). However, the NLOS path loss attenuation was reduced (resulting in $n = 3.0$ at 28 GHz and $n = 3.4$ at 73 GHz), when considering the antenna pointing angle combination between the TX and RX that resulted in maximum received power at each measurement location.

Single frequency omnidirectional path loss models were provided in the CI, CIX, and FI forms for the co- and cross-polarization measurements. Similar to the directional models, the CI PLEs calculated in LOS environments were significantly smaller than the theoretical free space PLE (1.1 and 1.3 for 28 GHz and 73 GHz, respectively), due to constructive interference and a waveguide effect in the indoor mmWave propagation channel. In NLOS indoor environments for co-polarized antennas, the 73 GHz CI model PLE was 3.2 (32 dB of attenuation per decade of distance) and the 28 GHz PLE was 2.7 (27 dB of attenuation per decade of distance), with shadow fading factors of 11.3 dB and 9.6 dB at 73 GHz and 28 GHz, respectively. The 73 GHz measurements showed greater omnidirectional isolation for co- and cross-polarized antenna configurations with a LOS XPD factor of 22.8 dB and a NLOS XPD factor of 15.4 dB, encouraging the use of dual polarization modulations and antenna polarization diversity applications for indoor mmWave communications systems. The 28 GHz measurements exhibited smaller omnidirectional isolation than 73 GHz, 14.0 dB and 10.4 dB for LOS and NLOS, respectively, but may still be good enough for polarization diversity. From the directional and omnidirectional path loss models presented here, it is clear that path loss increases with frequency much more prominently than in outdoor channels - likely due to the pronounced impact of the environment which is in very close proximity to the TX and RX and likely induces frequency-dependent diffuse scattering and weaker reflections at smaller wavelengths [105].

The multi-frequency directional and omnidirectional path loss models for both separate and combined polarization measurements showed the simplicity and accuracy of the CI and CIF models which use a FSPL anchored at 1 m to create a physically-based frequency-dependent model for path loss. The three parameter floating ABG model in all cases resulted in lower standard deviation compared to the CI and CIF models, but a large majority of the scenarios had differences or less than 1 dB, and in all cases the differences were usually less than an order of magnitude of the standard deviation of all models. The differences in modeling error between the CIF and ABG models were always minor, well within typical error ranges caused by gain drift, flexing of cables, and other typical measurement errors. All omnidirectional path loss data are provided in tables in Appendix B so that other researchers may generate their own models and conduct further studies based on the indoor propagation data at 28 GHz and 73 GHz.

For the most important case of the combined polarization omnidirectional path loss models, the single frequency CI model showed that there is more attenuation at 73 GHz (LOS PLE = 2.4, NLOS PLE = 3.8) than at 28 GHz (LOS PLE = 1.8, NLOS PLE = 3.1), where the FI model lacked an intuitive explanation of physics with the 73 GHz LOS and NLOS β values of 0.8 and 2.2, respectively. The multi-frequency CI and CIF models exhibited value as a one parameter and two parameter model, respectively, with little variation

in standard deviation from the more complex and less intuitive three parameter ABG model, where in LOS the standard deviations were 10.4 dB (CI), 9.9 dB (CIF), and 9.5 dB (ABG) for each respective model. Furthermore, the NLOS standard deviations were 12.5 dB for CI, 11.9 dB for CIF, and 11.6 dB for the ABG model, not considerably different for already large standard deviations that are greater than 11 dB. The CI PLEs and CIF n values also matched in LOS (PLE and $n = 2.1$) and NLOS (PLE and $n = 3.4$) environments for the combined polarization omnidirectional models. The ABG model did provide slightly lower standard deviations in LOS and NLOS (fraction of a dB from CI and CIF), but at the expense of more parameters and without a physical tie to transmitted power.

This work showed the efficacy of the CI model standardized to a 1 m free space reference distance. This model allows for simple calculations of large-scale path loss, as well as easy comparisons across frequency bands, environments, and measurements from other researchers [105, 114]. The CIF model naturally extends the CI model to account for frequency-dependent path loss with distance, and uses two parameters while retaining a link to the close-in free space distance, and offers virtually identical performance to the more complex ABG three parameter model. This work shows that either the one parameter CI model or the two parameter CIF model may be most suitable for indoor large-scale path loss modeling, with the CIF model providing a better fit to measured data over a wide range of mmWave frequencies, whereas outdoor channels are suitably modeled with the one parameter CI model. 3GPP, ITU, and other standards bodies would do well to consider the simplicity, accuracy, and stability of the CI and CIF models for future 5G standards.

Time dispersion characteristics using directional antennas showed that 90% of the RMS delay spreads in both LOS and NLOS environments were under 40 ns and 30 ns at 28 GHz and 73 GHz, respectively. LOS locations were generally found to have smaller RMS delay spreads than NLOS locations due to less obstructions and multipath in the LOS environment, but by no more than a few ns (not an order of magnitude). The higher frequency of 73 GHz had greater path loss for a fixed transmitter power, thus making late arriving components weaker than at 28 GHz. The mean RMS delay spreads for the single strongest pointing angles were reduced by 13.2 ns in LOS (from 17.3 ns to 4.1 ns) and 4.3 ns in NLOS (from 17.7 ns to 13.4 ns) for 28 GHz V-V scenarios, and were reduced by 9.2 ns and 1.0 ns in LOS and NLOS 73 GHz V-V scenarios, respectively, compared to the corresponding mean RMS delay spreads averaged over all arbitrary antenna pointing angles, indicating the potential for implementing steerable beams to reduce multipath time dispersion while increasing SNR for indoor mmWave wideband communications systems. Cross-polarized channels had less reduction in RMS delay spread when choosing the strongest angles between the TX and RX at both 28 GHz and 73 GHz, and in NLOS at 73 GHz, cross-polarized strongest received angles increased the RMS delay spread compared to arbitrary beam pointing. For time dispersion statistics with combined polarizations at 28 GHz and 73 GHz, it is apparent that the V-V polarized antennas contribute to larger delay spreads (maximum of 198.5 ns in NLOS), due to cross-polarization isolation. Similar to the co- and cross-polarized time dispersion statistics, the combined polarization mean RMS delay spreads were reduced when only considering the single strongest beams in LOS environments (reduced from 17.2 ns to 4.1 ns at 28 GHz and 12.1 ns to 3.6 ns at 73 GHz).

The multipath time dispersion characteristics and large-scale path loss models presented here will be important for mmWave channel modeling and may assist in the creation of new mmWave systems that support the Internet of Things (IoT) and the indoor use of future unlicensed bands or 5G cellular for high bandwidth applications. The large-scale path loss models presented in this report were explored and compared with extensive propagation data, and introduced new multi-frequency path loss models for use across the entire mmWave spectrum. Results suggest the use of simpler and physically-based path loss models compared to previous 3GPP models that use more parameters but offer very little additional accuracy while lacking a physical basis. While path loss characteristics at 73 GHz showed higher attenuation than at 28 GHz, both will be attractive options for high bandwidth and high data-rate applications in indoor environments.

This page is intentionally left blank.

Appendix A

Path Loss Model Parameter Closed-Form Expressions

Here we provide mathematical closed-form solutions for minimizing the shadow fading (SF) standard deviation (i.e. best fit) for the following large-scale path loss models: the CI (4.1), CIX (4.2), CIF (4.6), CIFX (4.7), FI (4.3), ABG (4.4), and ABGX (4.5) path loss models. The raw data used to compute the omnidirectional models in this report are given in Tables B.1–B.4.

A.1 CI Path Loss Model

The CI model with a reference distance of 1 m is given by (4.1) where n denotes the path loss exponent (PLE), d is the 3D T-R separation distance, and X_σ^{CI} is the SF. $\text{FSPL}(f, 1 \text{ m})$ denotes the free space path loss in dB at a 3D T-R separation distance of 1 m at the carrier frequency f :

$$\text{FSPL}(f, 1 \text{ m})[\text{dB}] = 10 \log_{10} \left(\frac{4\pi f}{c} \right)^2 \quad (\text{A.1})$$

where c is the speed of light.

From (4.1), the SF random variable is given by (A.2)

$$X_\sigma^{\text{CI}} = \text{PL}^{\text{CI}}(f, d)[\text{dB}] - \text{FSPL}(f, 1 \text{ m})[\text{dB}] - 10n \log_{10}(d) = A - nD \quad (\text{A.2})$$

where A (in dB) represents $\text{PL}^{\text{CI}}(f, d)[\text{dB}] - \text{FSPL}(f, 1 \text{ m})[\text{dB}]$, and D denotes $10 \log_{10}(d)$. It follows that the standard deviation of the random variable X_σ^{CI} is:

$$\sigma^{\text{CI}} = \sqrt{\sum X_\sigma^{\text{CI}2}/N} = \sqrt{\sum (A - nD)^2/N} \quad (\text{A.3})$$

where N is the number of measured path loss data points (see Tables B.1–B.4 for omnidirectional path loss data points and values). All summations in this appendix are performed over the length of the data or sample size, and the sums are calculated *directly* from the elements, i.e., if the elements are in dB units then the sum is calculated by adding all of the elements in dB units.

Minimizing the SF standard deviation σ^{CI} is equivalent to minimizing the term $\sum (A - nD)^2$. When $\sum (A - nD)^2$ is minimized, the derivative with respect to n should be zero:

$$\begin{aligned} \frac{d \sum (A - nD)^2}{dn} &= \sum 2D(nD - A) \\ &= 2 \sum D(nD - A) \\ &= 2(n \sum D^2 - \sum DA) \\ &= 0 \end{aligned} \tag{A.4}$$

Therefore, from (A.4):

$$n = \frac{\sum DA}{\sum D^2} \tag{A.5}$$

and hence the minimum SF standard deviation for the CI model is:

$$\sigma_{min}^{\text{CI}} = \sqrt{\sum (A - D \frac{\sum DA}{\sum D^2})^2 / N} \tag{A.6}$$

To find the closed-form solutions for software processing such as MATLAB, A and D are written as column vectors, and n can be expressed in matrix form as:

$$n = A^T (D^T D)^{-1} D \tag{A.7}$$

Accordingly, the minimum SF standard deviation for the CI model becomes:

$$\sigma_{min}^{\text{CI}} = \sqrt{\sum (A - (A^T (D^T D)^{-1} D) D)^2 / N} \tag{A.8}$$

From Section IV the CI model may be used for estimating path loss from either co- and cross-polarization measurements, as well as for combined polarization measurement data with arbitrary polarizations, where the PLE n is usually higher for cross-polarization as compared to co-polarization for the same locations.

A.2 CIX Path Loss Model

The CIX model (4.2) is an extension of the CI model (4.1) that describes path loss from cross-polarization measurements, where XPD denotes the cross-polarization discrimination factor. The CIX model in (4.2) uses the same PLE n as in the co-polarization CI model (4.1). The proper value for XPD is solved via the minimum mean square error (MMSE) method that fits the measured cross-polarized path loss data with the smallest error (i.e., minimum SF standard deviation).

Using the same notations as (A.2), the SF in (4.2) is expressed as:

$$X_{\sigma}^{\text{CIX}} = A - nD - \text{XPD} \tag{A.9}$$

and the SF standard deviation is:

$$\sigma^{\text{CIX}} = \sqrt{\sum X_{\sigma}^{\text{CIX}2} / N} = \sqrt{\sum (A - nD - \text{XPD})^2 / N} \tag{A.10}$$

The term $\sum (A - nD - \text{XPD})^2$ should be minimized in order to minimize σ^{CIX} . Let the derivative of $\sum (A - nD - \text{XPD})^2$ with respect to XPD be zero, such that:

$$\begin{aligned}
 \frac{\partial \sum (A - nD - \text{XPD})^2}{\partial \text{XPD}} &= \sum 2(\text{XPD} + nD - A) \\
 &= 2(\text{XPD} \times N + n \sum D - \sum A) \\
 &= 2(\text{XPD} \times N + \frac{\sum DA \sum D}{\sum D^2} \\
 &\quad - \sum A) \\
 &= 0
 \end{aligned} \tag{A.11}$$

From (A.11):

$$\text{XPD} = \frac{\sum A}{N} - \frac{\sum DA \sum D}{N \sum D^2} \tag{A.12}$$

Therefore, the minimum SF standard deviation for the CIX model is:

$$\sigma_{\min}^{\text{CIX}} = \sqrt{\sum (A - D \frac{\sum DA}{\sum D^2} - \frac{\sum A}{N} + \frac{\sum DA \sum D}{N \sum D^2})^2 / N} \tag{A.13}$$

Since both A and D can be considered column vectors, the optimum XPD can also be expressed in matrix form as:

$$\text{XPD} = \frac{\sum A - (A^T (D^T D)^{-1} D) D}{N} \tag{A.14}$$

A.3 CIF Path Loss Model

The equation of the CIF model (4.6) with a reference distance of 1 m is re-organized in the form:

$$\text{PL}^{\text{CIF}}(f, d)[\text{dB}] = \text{FSPL}(f, 1 \text{ m})[\text{dB}] + 10 \log_{10} \left(\frac{d}{d_0} \right) \left(n(1 - b) + \frac{nb}{f_0} f \right) + X_{\sigma}^{\text{CIF}} \tag{A.15}$$

where n is the PLE that includes the frequency-effect parameter b , and f_0 is the specified reference frequency that may be selected as the average of all measured frequencies. Let $A = \text{PL}^{\text{CIF}}(f, d)[\text{dB}] - \text{FSPL}(f, 1 \text{ m})[\text{dB}]$, $D = 10 \log_{10}(d)$, $a = n(1 - b)$, and $g = \frac{nb}{f_0}$, then we have:

$$X_{\sigma}^{\text{CIF}} = A - D(a + gf) \tag{A.16}$$

The SF standard deviation is:

$$\sigma^{\text{CIF}} = \sqrt{\sum X_{\sigma}^{\text{CIF}2} / N} = \sqrt{\sum (A - D(a + gf))^2 / N} \tag{A.17}$$

Minimizing σ^{CIF} is equivalent to minimizing $\sum (A - D(a + gf))^2$. When $\sum (A - D(a + gf))^2$ is minimized, its derivatives with respect to a and g should be zero, i.e.

$$\begin{aligned} \frac{\partial \sum (A - D(a + gf))^2}{\partial a} &= \sum 2D(aD + gDf - A) \\ &= 2(a \sum D^2 + g \sum D^2 f - \sum DA) \\ &= 0 \end{aligned} \quad (\text{A.18})$$

$$\begin{aligned} \frac{\partial \sum (A - D(a + gf))^2}{\partial g} &= \sum 2Df(aD + gDf - A) \\ &= 2(a \sum D^2 f + g \sum D^2 f^2 \\ &\quad - \sum DAf) \\ &= 0 \end{aligned} \quad (\text{A.19})$$

which can be simplified to:

$$a \sum D^2 + g \sum D^2 f - \sum DA = 0 \quad (\text{A.20})$$

$$a \sum D^2 f + g \sum D^2 f^2 - \sum DAf = 0 \quad (\text{A.21})$$

Combining (A.20) and (A.21) yields:

$$a = \frac{\sum D^2 f \sum DAf - \sum D^2 f^2 \sum DA}{(\sum D^2 f^2)^2 - \sum D^2 \sum D^2 f^2} \quad (\text{A.22})$$

$$g = \frac{\sum D^2 f \sum DA - \sum D^2 \sum DAf}{(\sum D^2 f)^2 - \sum D^2 \sum D^2 f^2} \quad (\text{A.23})$$

Put into matrix form, a and g are:

$$a = \frac{f^T \text{diag}(DD^T) f^T \text{diag}(DA^T) - (\text{diag}(ff^T))^T \text{diag}(DD^T) D^T A}{((\text{diag}(ff^T))^T \text{diag}(DD^T))^2 - (\text{diag}(ff^T))^T \text{diag}(DD^T) D^T D} \quad (\text{A.24})$$

$$g = \frac{f^T \text{diag}(DD^T) D^T A - f^T \text{diag}(DA^T) D^T D}{((\text{diag}(ff^T))^T \text{diag}(DD^T))^2 - (\text{diag}(ff^T))^T \text{diag}(DD^T) D^T D} \quad (\text{A.25})$$

Equations (A.22)–(A.25) are closed-form solutions for a and g . Substituting a and g in (A.17) with (A.24) and (A.25), the minimum SF standard deviation for the CIF model is found.

After solving for a and g , we can use the previous definition $a = n(1 - b)$ and $g = \frac{nb}{f_0}$ to calculate n , b , and f_0 . However, there are two equations but three unknowns, hence there is no unique solution in general using three parameters. However, a unique closed-form solution is available when f_0 is specified as a constant deemed appropriate by the user, such as the weighted average of all frequencies used in the model, or at a natural loss transition band (e.g., where measurements show an inflection point in the PLE), or at known transition points like the 60 GHz oxygen absorption band. Consequently, n and b are solved by:

$$n = a + gf_0 \quad (\text{A.26})$$

$$b = \frac{gf_0}{a + gf_0} \quad (\text{A.27})$$

A.4 CIFX Path Loss Model

The CIFX path loss model (4.7) and also expressed as:

$$\text{PL}^{\text{CIFX}}(f, d)[\text{dB}] = \text{FSPL}(f, 1 \text{ m})[\text{dB}] + 10 \log_{10} \left(\frac{d}{d_0} \right) (a + gf) + \text{XPD} + X_{\sigma}^{\text{CIFX}} \quad (\text{A.28})$$

where XPD denotes the cross-polarization discrimination factor, n , b , and f_0 have the same meanings as in the CIF model (A.15). Note that the CIFX model (A.28) uses the same a and g as substituted in the CIF model (A.15), thus the a and g in (A.28) are also given by (A.24) and (A.25), respectively. The XPD is solved via the MMSE method that fits the measured cross-polarized path loss data with the smallest error (i.e., SF standard deviation).

Using the same notations as in the CIF model, the SF in the CIFX model can be expressed as

$$X_{\sigma}^{\text{CIFX}} = A - (a + gf)D - \text{XPD} \quad (\text{A.29})$$

Hence the SF standard deviation is:

$$\begin{aligned} \sigma^{\text{CIFX}} &= \sqrt{\sum X_{\sigma}^{\text{CIFX}2}/N} \\ &= \sqrt{\sum (A - (a + gf)D - \text{XPD})^2/N} \end{aligned} \quad (\text{A.30})$$

Thus the term $\sum (A - (a + gf)D - \text{XPD})^2$ should be minimized in order to minimize σ^{CIFX} . With the derivative of $\sum (A - (a + gf)D - \text{XPD})^2$ with respect to XPD set to zero, we have:

$$\begin{aligned} &\frac{\partial \sum (A - (a + gf)D - \text{XPD})^2}{\partial \text{XPD}} \\ &= \sum 2(\text{XPD} + (a + gf)D - A) \\ &= 2(\text{XPD} \times N + a \sum D + g \sum Df - \sum A) \\ &= 0 \end{aligned} \quad (\text{A.31})$$

From (A.11):

$$\text{XPD} = \frac{\sum A - a \sum D - g \sum Df}{N} \quad (\text{A.32})$$

Or equivalently

$$\text{XPD} = \frac{\sum A - a \sum D - gD^T f}{N} \quad (\text{A.33})$$

Therefore, by plugging (A.24), (A.25) and (A.32) back into (A.30), the minimum SF standard deviation for the CIFX model is found.

A.5 FI Path Loss Model

The FI path loss model (4.3) uses α as the floating intercept in dB (different from a FSPL reference), and β is the slope of the line (different from a PLE). Assuming $B = \text{PL}^{\text{ABG}}(d)[\text{dB}]$, and $D = 10 \log_{10}(d)$, the SF is given by:

$$X_{\sigma}^{\text{FI}} = B - \alpha - \beta D \quad (\text{A.34})$$

and the SF standard deviation is:

$$\sigma^{\text{FI}} = \sqrt{\sum X_{\sigma}^{\text{FI}2}/N} = \sqrt{\sum (B - \alpha - \beta D)^2/N} \quad (\text{A.35})$$

The term $\sum (B - \alpha - \beta D)^2$ is to be minimized, which means its partial derivatives with respect to α and β should be zero, i.e.,

$$\begin{aligned} \frac{\partial \sum (B - \alpha - \beta D)^2}{\partial \alpha} &= \sum 2(\alpha + \beta D - B) \\ &= 2(N\alpha + \beta \sum D - \sum B) \\ &= 0 \end{aligned} \quad (\text{A.36})$$

$$\begin{aligned} \frac{\partial \sum (B - \alpha - \beta D)^2}{\partial \beta} &= \sum 2D(\alpha + \beta D - B) \\ &= 2(\alpha \sum D + \beta \sum D^2 - \sum DB) \\ &= 0 \end{aligned} \quad (\text{A.37})$$

(A.36) and (A.37) yield:

$$N\alpha + \beta \sum D - \sum B = 0 \quad (\text{A.38})$$

$$\alpha \sum D + \beta \sum D^2 - \sum DB \quad (\text{A.39})$$

Combining (A.38) and (A.39) yields:

$$\alpha = \frac{\sum D \sum DB - \sum D^2 \sum B}{(\sum D)^2 - N \sum D^2} \quad (\text{A.40})$$

$$\beta = \frac{\sum D \sum B - N \sum DB}{(\sum D)^2 - N \sum D^2} \quad (\text{A.41})$$

The minimum SF standard deviation can be obtained by substituting α and β in (A.35) with (A.40) and (A.41), respectively. Alternatively, α and β in the FI model can be expressed in matrix form as

$$\beta = (D - \bar{D})^T ((D - \bar{D})^T (D - \bar{D}))^{-1} (B - \bar{B}) \quad (\text{A.42})$$

$$\alpha = \bar{B} - \beta \bar{D} \quad (\text{A.43})$$

where \bar{D} and \bar{B} denote the mean value of the elements in column vectors D and B , respectively. All the mean values are calculated *directly* from the elements in the vector, i.e., if the elements are in dB scale then the mean is calculated directly in dB scale.

A.6 ABG Path Loss Model

The ABG model (4.4) has a 1 m reference distance and 1 GHz reference frequency) where α and γ are coefficients showing the dependence of path loss on distance and frequency, respectively, β is the offset in path loss, d is the 3D T-R separation distance in meters, and f is the carrier frequency in GHz. Assuming $B = \text{PL}^{\text{ABG}}(f, d)[\text{dB}]$, $D = 10 \log_{10}(d)$, and $F = 10 \log_{10}(f)$ in (4.4), the SF is given by:

$$X_{\sigma}^{\text{ABG}} = B - \alpha D - \beta - \gamma F \quad (\text{A.44})$$

and the SF standard deviation is:

$$\sigma^{\text{ABG}} = \sqrt{\sum X_{\sigma}^{\text{ABG}2}/N} = \sqrt{\sum (B - \alpha D - \beta - \gamma F)^2/N} \quad (\text{A.45})$$

Similar to minimizing Eqs. (A.2) and (A.17) the term $\sum (B - \alpha D - \beta - \gamma F)^2$ is to be minimized, which means its partial derivatives with respect to α , β , and γ should be zero, i.e.,

$$\begin{aligned} \frac{\partial \sum (B - \alpha D - \beta - \gamma F)^2}{\partial \alpha} &= \sum 2D(\alpha D + \beta + \gamma F - B) \\ &= 2(\alpha \sum D^2 + \beta \sum D \\ &\quad + \gamma \sum DF - \sum DB) \\ &= 0 \end{aligned} \quad (\text{A.46})$$

$$\begin{aligned} \frac{\partial \sum (B - \alpha D - \beta - \gamma F)^2}{\partial \beta} &= \sum 2(\alpha D + \beta + \gamma F - B) \\ &= 2(\alpha \sum D + N\beta + \gamma \sum F \\ &\quad - \sum B) \\ &= 0 \end{aligned} \quad (\text{A.47})$$

$$\begin{aligned} \frac{\partial \sum (B - \alpha D - \beta - \gamma F)^2}{\partial \gamma} &= \sum 2F(\alpha D + \beta + \gamma F - B) \\ &= 2(\alpha \sum DF + \beta \sum F \\ &\quad + \gamma \sum F^2 - \sum FB) \\ &= 0 \end{aligned} \quad (\text{A.48})$$

from (A.46), (A.47), and (A.48) it is clear that

$$\alpha \sum D^2 + \beta \sum D + \gamma \sum DF - \sum DB = 0 \quad (\text{A.49})$$

$$\alpha \sum D + N\beta + \gamma \sum F - \sum B = 0 \quad (\text{A.50})$$

$$\alpha \sum DF + \beta \sum F + \gamma \sum F^2 - \sum FB = 0 \quad (\text{A.51})$$

Such that (A.49), (A.50), and (A.51) in matrix form is:

$$\begin{pmatrix} \sum D^2 & \sum D & \sum DF \\ \sum D & N & \sum F \\ \sum DF & \sum F & \sum F^2 \end{pmatrix} \begin{pmatrix} \alpha \\ \beta \\ \gamma \end{pmatrix} = \begin{pmatrix} \sum DB \\ \sum B \\ \sum FB \end{pmatrix} \quad (\text{A.52})$$

Through calculation and simplification, the closed-form solutions for α , β , and γ are given by (A.55), (A.56), and (A.57), respectively. Equations (A.58), (A.59), and (A.60) show the solutions in matrix form. Finally, the minimum SF standard deviation for the ABG model can be obtained by plugging (A.55), (A.56), and (A.57) back into (A.45). Or a system of simultaneous equations allow for α , β , and γ to be found by:

$$\begin{pmatrix} \alpha \\ \beta \\ \gamma \end{pmatrix} = \begin{pmatrix} \sum D^2 & \sum D & \sum DF \\ \sum D & N & \sum F \\ \sum DF & \sum F & \sum F^2 \end{pmatrix}^{-1} \begin{pmatrix} \sum DB \\ \sum B \\ \sum FB \end{pmatrix} \quad (\text{A.53})$$

A.7 ABGX Path Loss Model

The ABGX model (4.5) is found in the exact same manner as the CIX and CIFX models. The α , β , and γ values found for the co-polarized ABG model (4.4) are substituted into the right hand side of (4.4) for all measured distances d to form a vector of estimated path loss values, specified as ABG_{PL} . Then using the cross-polarized path loss values in vector form A from measurements, the XPD factor for the ABGX model is:

$$\text{XPD} = \frac{\sum A - ABG_{PL}}{N} \quad (\text{A.54})$$

$$\alpha = \frac{(\sum D \sum B - N \sum DB)((\sum F)^2 - N \sum F^2) - (\sum D \sum F - N \sum DF)(\sum F \sum B - N \sum FB)}{((\sum D)^2 - N \sum D^2)((\sum F)^2 - N \sum F^2) - (\sum D \sum F - N \sum DF)^2} \quad (\text{A.55})$$

$$\beta = \frac{(\sum D \sum FB - \sum B \sum DF)(\sum F \sum D^2 - \sum D \sum DF) - (\sum B \sum D^2 - \sum D \sum DB)(\sum D \sum F^2 - \sum F \sum DF)}{((\sum D)^2 - N \sum D^2)(\sum D \sum F^2 - \sum F \sum DF) + (\sum D \sum F - N \sum DF)(\sum F \sum D^2 - \sum D \sum DF)} \quad (\text{A.56})$$

$$\gamma = \frac{(\sum F \sum B - N \sum FB)((\sum D)^2 - N \sum D^2) - (\sum D \sum F - N \sum DF)(\sum D \sum B - N \sum DB)}{((\sum F)^2 - N \sum F^2)((\sum D)^2 - N \sum D^2) - (\sum D \sum F - N \sum DF)^2} \quad (\text{A.57})$$

$$\alpha = \frac{(\sum D \sum B - ND^T B)((\sum F)^2 - NF^T F) - (\sum D \sum F - ND^T F)(\sum F \sum B - NF^T B)}{((\sum D)^2 - ND^T D)((\sum F)^2 - NF^T F) - (\sum D \sum F - ND^T F)^2} \quad (\text{A.58})$$

$$\beta = \frac{(F^T B \sum D - D^T F \sum B)(D^T D \sum F - D^T F \sum D) - (D^T D \sum B - D^T B \sum D)(F^T F \sum D - D^T F \sum F)}{((\sum D)^2 - ND^T D)(F^T F \sum D - D^T F \sum F) + (\sum D \sum F - ND^T F)(D^T D \sum F - D^T F \sum D)} \quad (\text{A.59})$$

$$\gamma = \frac{(\sum F \sum B - NF^T B)((\sum D)^2 - ND^T D) - (\sum D \sum F - ND^T F)(\sum D \sum B - ND^T B)}{((\sum F)^2 - NF^T F)((\sum D)^2 - ND^T D) - (\sum D \sum F - ND^T F)^2} \quad (\text{A.60})$$

This page is intentionally left blank.

Appendix B

Omnidirectional Path Loss Values

Table B.1: 28 GHz co-polarized antenna (V-V) omnidirectional path loss values with corresponding Environment (Env.) TX IDs, RX IDs, path loss (PL) in dB, and 3D T-R separation distance in meters.

28 GHz Omnidirectional V-V Path Loss				
Env.	TX ID	RX ID	PL (dB)	T-R (m)
LOS	1	1	69.3	6.4
LOS	1	4	75.3	7.9
LOS	1	7	76.5	12.9
LOS	2	10	66.3	4.1
LOS	3	16	68.0	5.3
LOS	4	11	74.3	12.7
LOS	4	12	70.4	7.1
LOS	4	28	75.4	21.3
LOS	4	121	71.3	7.1
LOS	4	161	74.5	20.6
NLOS	1	2	76.6	7.8
NLOS	1	3	82.7	10.1
NLOS	1	5	84.3	11.9
NLOS	1	6	86.4	14.4
NLOS	1	8	95.9	25.9
NLOS	1	9	118.5	32.9
NLOS	2	11	78.5	9.0
NLOS	2	12	89.5	28.5
NLOS	2	13	113.1	29.2
NLOS	2	14	119.3	30.4
NLOS	2	15	115.8	39.2
NLOS	2	16	97.8	41.9
NLOS	2	17	120.5	45.9
NLOS	2	18	93.6	12.1
NLOS	2	19	103.1	15.5
NLOS	2	20	111.3	17.1
NLOS	2	21	78.0	6.7
NLOS	2	22	95.3	14.8
NLOS	2	161	98.6	41.9
NLOS	3	17	85.8	8.7
NLOS	3	23	79.9	5.6
NLOS	3	24	86.1	7.8
NLOS	3	25	76.31	8.4
NLOS	3	26	72.9	5.5
NLOS	3	27	75.8	8.3
NLOS	4	13	97.2	8.2
NLOS	4	14	105.0	10.8
NLOS	4	15	97.5	20.8
NLOS	4	16	80.0	20.6
NLOS	4	18	96.8	33.0
NLOS	5	8	73.8	3.9
NLOS	5	19	75.3	6.9
NLOS	5	28	86.1	15.6
NLOS	5	29	81.3	15.0
NLOS	5	30	88.7	11.4
NLOS	5	31	90.4	13.9
NLOS	5	32	90.2	31.2
NLOS	5	33	97.0	9.1

Table B.2: 28 GHz cross-polarized antenna (V-H) omnidirectional path loss values with corresponding Environment (Env.) TX IDs, RX IDs, path loss (PL) in dB, and 3D T-R separation distance in meters.

28 GHz Omnidirectional V-H Path Loss				
Env.	TX ID	RX ID	PL (dB)	T-R (m)
LOS	1	1	84.1	6.4
LOS	1	4	87.7	7.9
LOS	1	7	89.7	12.9
LOS	2	10	78.6	4.1
LOS	3	16	83.4	5.3
LOS	4	11	88.2	12.7
LOS	4	12	85.1	7.1
LOS	4	28	90.2	21.3
LOS	4	121	85.0	7.1
LOS	4	161	89.8	20.6
NLOS	1	2	88.2	7.8
NLOS	1	3	91.3	10.1
NLOS	1	5	94.7	11.9
NLOS	1	6	100.1	14.4
NLOS	1	8	115.3	25.9
NLOS	2	11	88.5	9.0
NLOS	2	12	108.8	28.5
NLOS	2	13	141.6	29.2
NLOS	2	14	139.6	30.4
NLOS	2	16	113.4	41.9
NLOS	2	18	98.9	12.1
NLOS	2	19	113.7	15.5
NLOS	2	20	120.4	17.1
NLOS	2	21	83.7	6.7
NLOS	2	22	101.6	14.8
NLOS	2	161	110.5	41.9
NLOS	3	17	97.2	8.7
NLOS	3	23	92.7	5.6
NLOS	3	24	95.8	7.8
NLOS	3	25	88.9	8.4
NLOS	3	26	86.7	5.5
NLOS	3	27	89.3	8.3
NLOS	4	13	104.6	8.2
NLOS	4	14	112.8	10.8
NLOS	4	15	108.4	20.8
NLOS	4	16	93.7	20.6
NLOS	4	18	109.4	33.0
NLOS	5	8	89.3	3.9
NLOS	5	19	91.5	6.9
NLOS	5	28	98.4	15.6
NLOS	5	29	93.7	15.0
NLOS	5	30	96.1	11.4
NLOS	5	31	100.2	13.9
NLOS	5	32	104.8	31.2
NLOS	5	33	104.6	9.1

Table B.3: 73 GHz co-polarized antenna (V-V) omnidirectional path loss values with corresponding Environment (Env.) TX IDs, RX IDs, path loss (PL) in dB, and 3D T-R separation distance in meters.

73 GHz Omnidirectional V-H Path Loss				
Env.	TX ID	RX ID	PL (dB)	T-R (m)
LOS	1	1	81.7	6.4
LOS	1	4	81.2	7.9
LOS	1	7	86.7	12.9
LOS	2	10	79.9	4.1
LOS	3	16	82.4	5.3
LOS	4	11	84.1	12.7
LOS	4	12	82.3	7.1
LOS	4	28	82.6	21.3
LOS	4	121	83.2	7.1
LOS	4	161	84.6	20.6
NLOS	1	2	92.1	7.8
NLOS	1	3	89.8	10.1
NLOS	1	5	100.4	11.9
NLOS	1	6	104.0	14.4
NLOS	1	8	121.8	25.9
NLOS	2	11	92.8	9.0
NLOS	2	12	102.1	28.5
NLOS	2	13	118.9	29.2
NLOS	2	14	127.4	30.4
NLOS	2	15	142.5	39.2
NLOS	2	16	111.2	41.9
NLOS	2	18	115.7	12.1
NLOS	2	19	142.5	15.5
NLOS	2	21	94.5	6.7
NLOS	2	22	116.3	14.8
NLOS	2	161	108.2	41.9
NLOS	3	17	107.5	8.7
NLOS	3	23	102.7	5.6
NLOS	3	24	111.4	7.8
NLOS	3	25	90.4	8.4
NLOS	3	26	93.3	5.5
NLOS	3	27	89.7	8.3
NLOS	4	13	104.7	8.2
NLOS	4	14	115.5	10.8
NLOS	4	15	114.2	20.8
NLOS	4	16	102.4	20.6
NLOS	4	18	108.4	33
NLOS	5	8	91.0	3.9
NLOS	5	19	90.2	6.9
NLOS	5	28	100.1	15.6
NLOS	5	29	94.7	15.0
NLOS	5	30	107.6	11.4
NLOS	5	31	112.8	13.9
NLOS	5	32	105.5	31.2
NLOS	5	33	118.7	9.1

Table B.4: 73 GHz cross-polarized antenna (V-H) omnidirectional path loss values with corresponding Environment (Env.) TX IDs, RX IDs, path loss (PL) in dB, and 3D T-R separation distance in meters.

73 GHz Omnidirectional V-H Path Loss				
Env.	TX ID	RX ID	PL (dB)	T-R (m)
LOS	1	1	102.4	6.4
LOS	1	4	100.4	7.9
LOS	1	7	111.5	12.9
LOS	2	10	101.3	4.1
LOS	3	16	102.9	5.3
LOS	4	11	108.2	12.7
LOS	4	12	104.0	7.1
LOS	4	28	106.6	21.3
LOS	4	121	106.0	7.1
LOS	4	161	108.7	20.6
NLOS	1	2	106.1	7.8
NLOS	1	3	108.8	10.1
NLOS	1	5	116.7	11.9
NLOS	1	6	115.3	14.4
NLOS	2	11	110.6	9
NLOS	2	12	124.2	28.5
NLOS	2	16	138.9	41.9
NLOS	2	18	130.6	12.1
NLOS	2	21	111.0	6.7
NLOS	2	22	126.6	14.8
NLOS	2	161	126.4	41.9
NLOS	3	17	122.3	8.7
NLOS	3	23	117.2	5.6
NLOS	3	24	122.1	7.8
NLOS	3	25	109.7	8.4
NLOS	3	26	104.8	5.5
NLOS	3	27	113.3	8.3
NLOS	4	13	123.4	8.2
NLOS	4	14	140.2	10.8
NLOS	4	15	134.2	20.8
NLOS	4	16	116.2	20.6
NLOS	4	18	129.9	33.0
NLOS	5	8	106.7	3.9
NLOS	5	19	112.8	6.9
NLOS	5	28	117.7	15.6
NLOS	5	29	117.4	15.0
NLOS	5	30	125.8	11.4
NLOS	5	31	120.2	13.9
NLOS	5	32	128.3	31.2
NLOS	5	33	132.1	9.1

This page is intentionally left blank.

Appendix C

Path Loss Model Standard Deviations Side-by-Side

Table C.1: Single frequency directional path loss model standard deviations for the CI model with $d_0 = 1$ m, the CIX model, and the FI path loss model. “Freq.” stands for carrier frequency, “Pol.” stands for TX-RX antenna polarization configuration, “Env.” stands for environment, and “Comb.” stands for combined polarization. Differences in standard deviations are also shown.

Single Frequency Directional CI, CIX, and FI Models								
Freq.	Pol.	Env.	CI	CIX	FI	$\sigma_{\text{CI}} - \sigma_{\text{FI}}$	$\sigma_{\text{CI}} - \sigma_{\text{CIX}}$	$\sigma_{\text{CIX}} - \sigma_{\text{FI}}$
			σ [dB]	σ [dB]	σ [dB]	Δ [dB]	Δ [dB]	Δ [dB]
28 GHz	V-V	LOS	2.5	-	2.0	0.5	-	-
		NLOS	11.6	-	10.6	1.0	-	-
		NLOS-best	10.8	-	10.7	0.1	-	-
	V-H	LOS	8.0	2.6	1.6	6.4	5.4	1.0
		NLOS	10.9	9.6	8.0	2.9	1.3	1.6
		NLOS-best	9.1	8.7	8.7	0.4	0.4	0.0
	Comb.	LOS	13.3	-	12.2	1.1	-	-
		NLOS	11.9	-	10.1	1.8	-	-
		NLOS-best	10.8	-	10.7	0.1	-	-
73 GHz	V-V	LOS	3.2	-	2.3	0.9	-	-
		NLOS	15.7	-	11.3	4.4	-	-
		NLOS-best	11.8	-	11.7	0.1	-	-
	V-H	LOS	8.6	4.6	4.6	4.0	4.0	0.0
		NLOS	15.9	13.2	9.0	6.9	2.7	4.2
		NLOS-best	11.0	8.7	8.2	2.8	2.3	0.5
	Comb.	LOS	16.8	-	15.8	1.0	-	-
		NLOS	16.7	-	11.7	5.0	-	-
		NLOS-best	11.8	-	11.7	0.1	-	-

Table C.2: Multi-frequency directional path loss model standard deviations for the CI, CIX, CIF, CIFX, ABG, and ABGX large-scale path loss models. “Pol.” stands for TX-RX antenna polarization configuration, “Env.” stands for environment, and “Comb.” stands for combined polarization. Differences in standard deviations are also shown.

Multi-Frequency Directional CI(X), CIF(X), and ABG(X) Models							
Pol.	Env.	CI	CIF	ABG	$\sigma_{CI} - \sigma_{CIF}$	$\sigma_{CI} - \sigma_{ABG}$	$\sigma_{CIF} - \sigma_{ABG}$
		σ [dB]	σ [dB]	σ [dB]	Δ [dB]	Δ [dB]	Δ [dB]
V-V	LOS	2.9	2.9	2.1	0.0	0.8	0.8
	NLOS	14.6	13.9	11.1	0.7	3.5	2.8
	NLOS-best	11.5	11.3	11.2	0.2	0.3	0.1
Pol.	Env.	CIX	CIFX	ABGX	$\sigma_{CIX} - \sigma_{CIFX}$	$\sigma_{CIX} - \sigma_{ABGX}$	$\sigma_{CIFX} - \sigma_{ABGX}$
		σ [dB]	σ [dB]	σ [dB]	Δ [dB]	Δ [dB]	Δ [dB]
V-H	LOS	4.7	5.0	4.9	-0.3	-0.2	0.1
	NLOS	13.3	11.8	8.7	1.5	4.6	3.1
	NLOS-best	9.6	9.0	8.8	0.6	0.8	0.2
Pol.	Env.	CI	CIF	ABG	$\sigma_{CI} - \sigma_{CIF}$	$\sigma_{CI} - \sigma_{ABG}$	$\sigma_{CIF} - \sigma_{ABG}$
		σ [dB]	σ [dB]	σ [dB]	Δ [dB]	Δ [dB]	Δ [dB]
Comb.	LOS	15.2	15.2	14.2	0.0	1.0	1.0
	NLOS	15.5	14.5	11.0	1.0	4.5	3.5
	NLOS-best	11.5	11.3	11.2	0.2	0.3	0.1

Table C.3: Single frequency omnidirectional path loss model standard deviations for the CI model with $d_0 = 1$ m, the CIX model, and the FI path loss model. “Freq.” stands for carrier frequency, “Pol.” stands for TX-RX antenna polarization configuration, “Env.” stands for environment, and “Comb.” stands for combined polarization. Differences in standard deviations are also shown.

Single Frequency Omnidirectional CI, CIX, and FI Models								
Freq.	Pol.	Env.	CI	CIX	FI	$\sigma_{CI} - \sigma_{FI}$	$\sigma_{CI} - \sigma_{CIX}$	$\sigma_{CIX} - \sigma_{FI}$
			σ [dB]	σ [dB]	σ [dB]	Δ [dB]	Δ [dB]	Δ [dB]
28 GHz	V-V	LOS	1.8	-	1.8	0.0	-	-
		NLOS	9.6	-	9.3	0.3	-	-
	V-H	LOS	3.0	1.5	1.4	1.6	1.5	0.1
		NLOS	9.4	9.7	9.4	0.0	-0.3	0.3
	Comb.	LOS	7.3	-	7.2	0.1	-	-
		NLOS	10.9	-	10.9	0.0	-	-
73 GHz	V-V	LOS	2.4	-	1.4	1.0	-	-
		NLOS	11.3	-	11.2	0.1	-	-
	V-H	LOS	6.3	2.4	2.3	4.0	3.9	0.1
		NLOS	9.7	8.0	7.5	2.2	1.7	0.5
	Comb.	LOS	12.0	-	11.3	0.7	-	-
		NLOS	12.9	-	12.1	0.8	-	-

Table C.4: Multi-frequency omnidirectional path loss model standard deviations for the CI, CIX, CIF, CIFX, ABG, and ABGX large-scale path loss models. “Pol.” stands for TX-RX antenna polarization configuration, “Env.” stands for environment, and “Comb.” stands for combined polarization. Differences in standard deviations are also shown.

Multi-Frequency Omnidirectional CI(X), CIF(X), and ABG(X) Models							
Pol.	Env.	CI	CIF	ABG	$\sigma_{\text{CI}} - \sigma_{\text{CIF}}$	$\sigma_{\text{CI}} - \sigma_{\text{ABG}}$	$\sigma_{\text{CIF}} - \sigma_{\text{ABG}}$
		σ [dB]	σ [dB]	σ [dB]	Δ [dB]	Δ [dB]	Δ [dB]
V-V	LOS	2.3	2.1	1.8	0.2	0.5	0.3
	NLOS	10.9	10.4	10.3	0.5	0.6	0.1
Pol.	Env.	CIX	CIFX	ABGX	$\sigma_{\text{CIX}} - \sigma_{\text{CIFX}}$	$\sigma_{\text{CIX}} - \sigma_{\text{ABGX}}$	$\sigma_{\text{CIFX}} - \sigma_{\text{ABGX}}$
		σ [dB]	σ [dB]	σ [dB]	Δ [dB]	Δ [dB]	Δ [dB]
V-H	LOS	5.7	4.8	4.7	0.9	1.0	0.1
	NLOS	10.4	9.3	9.0	1.1	1.4	0.3
Pol.	Env.	CI	CIF	ABG	$\sigma_{\text{CI}} - \sigma_{\text{CIF}}$	$\sigma_{\text{CI}} - \sigma_{\text{ABG}}$	$\sigma_{\text{CIF}} - \sigma_{\text{ABG}}$
		σ [dB]	σ [dB]	σ [dB]	Δ [dB]	Δ [dB]	Δ [dB]
Comb.	LOS	10.4	9.9	9.5	0.5	0.9	0.4
	NLOS	12.5	11.9	11.6	0.6	0.9	0.3

This page is intentionally left blank.

Bibliography

- [1] Z. Pi and F. Khan, “An introduction to millimeter-wave mobile broadband systems,” *IEEE Communications Magazine*, vol. 49, no. 6, pp. 101–107, June 2011.
- [2] L. Yinzhou, J. Yang, and N. Ansari, “Cellular smartphone traffic and user behavior analysis,” in *2014 IEEE International Conference on Communications (ICC)*, June 2014, pp. 1326–1331.
- [3] T. S. Rappaport, “Keynote Speech: Millimeter Wave Wireless Communications - The Renaissance of Computing and Communications,” in *2014 IEEE International Conference on Communications (ICC)*, Sydney, Australia, June 2014. [Online]. Available: http://icc2014.ieee-icc.org/speakers_28_4101586138.pdf
- [4] F. Aldhaban, “Exploring the adoption of smartphone technology: Literature review,” in *Proceedings of PICMET '12: Technology Management for Emerging Technologies (PICMET)*, July 2012, pp. 2758–2770.
- [5] Gartner, “Gartner says by 2018, more than 50 percent of users will use a tablet or smartphone first for all online activities,” Dec. 2014. [Online]. Available: <http://www.gartner.com/newsroom/id/2939217>
- [6] T. S. Rappaport, S. Sun, R. Mayzus, H. Zhao, Y. Azar, K. Wang, G. N. Wong, J. K. Schulz, M. K. Samimi, and F. Gutierrez, Jr., “Millimeter Wave Mobile Communications for 5G Cellular: It Will Work!” *IEEE Access*, vol. 1, pp. 335–349, 2013.
- [7] T. S. Rappaport, R. W. Heath, Jr., R. C. Daniels, and J. N. Murdock, *Millimeter Wave Wireless Communications*. Pearson/Prentice Hall, 2015.
- [8] CISCO, “20 Myths of Wi-Fi Interference: Dispel Myths to Gain High Performing and Reliable Wireless,” 2007. [Online]. Available: http://www.cisco.com/c/en/us/products/collateral/wireless/spectrum-expert-wi-fi/prod_white_paper0900aecd807395a9.pdf
- [9] Z. Hays, G. Richter, S. Berger, C. Baylis, and R. J. Marks, “Alleviating airport WiFi congestion: An comparison of 2.4 GHz and 5 GHz WiFi usage and capabilities,” in *2014 Texas Symposium on Wireless and Microwave Circuits and Systems (WMCS)*, Apr. 2014, pp. 1–4.
- [10] C. Na, J. K. Chen, and T. S. Rappaport, “Hotspot traffic statistics and throughput models for several applications,” in *2004 Proceedings of the Global Telecommunications Conference (GLOBECOM)*, 2004, pp. 3257–3263.
- [11] —, “Measured traffic statistics and throughput of IEEE 802.11b public WLAN hotspots with three different applications,” *IEEE Transactions on Wireless Communications*, vol. 5, no. 11, pp. 3296–3305, 2006.
- [12] C. Sergiou, P. Antoniou, and V. Vassiliou, “A comprehensive survey of congestion control protocols in wireless sensor networks,” *IEEE Communications Surveys Tutorials*, vol. 16, no. 4, pp. 1839–1859, 2014.

-
- [13] H. Xu, V. Kukshya, and T. S. Rappaport, "Spatial and temporal characteristics of 60-GHz indoor channels," *IEEE Journal on Selected Areas in Communications*, vol. 20, no. 3, pp. 620–630, Apr. 2002.
- [14] A. Maltsev, R. Maslennikov, A. Sevastyanov, A. Khoryaev, and A. Lomayev, "Experimental investigations of 60 GHz WLAN systems in office environment," *IEEE Journal on Selected Areas in Communications*, vol. 27, no. 8, pp. 1488–1499, Oct. 2009.
- [15] X. Ge, H. Cheng, M. Guizani, and T. Han, "5G wireless backhaul networks: challenges and research advances," *IEEE Network*, vol. 28, no. 6, pp. 6–11, Nov. 2014.
- [16] S. E. Alexander, "Characterising buildings for propagation at 900 MHz," *Electronics Letters*, vol. 19, no. 20, pp. 860–861, Sept. 1983.
- [17] D. Akerberg, "Properties of a TDMA pico cellular office communication system," in *IEEE 39th Vehicular Technology Conference*, vol. 1, May 1989, pp. 186–191.
- [18] A. A. M. Saleh and R. A. Valenzuela, "A statistical model for indoor multipath propagation," *IEEE Journal on Selected Areas in Communications*, vol. 5, no. 2, pp. 128–137, Feb. 1987.
- [19] R. J. C. Bultitude, "Measurement, characterization and modeling of indoor 800/900 MHz radio channels for digital communications," *IEEE Communications Magazine*, vol. 25, no. 6, pp. 5–12, June 1987.
- [20] A. J. Motley and J. Keenan, "Personal communication radio coverage in buildings at 900 MHz and 1700 MHz," *Electronics Letters*, vol. 24, no. 12, pp. 763–764, Jun. 1988.
- [21] T. S. Rappaport, "Characterization of UHF multipath radio channels in factory buildings," *IEEE Transactions on Antennas and Propagation*, vol. 37, no. 8, pp. 1058–1069, Aug. 1989.
- [22] T. S. Rappaport and D. A. Hawbaker, "Effects of circular and linear polarized antennas on wide-band propagation parameters in indoor radio channels," in *Global Telecommunications Conference, 1991. GLOBECOM '91. Countdown to the New Millennium. Featuring a Mini-Theme on: Personal Communications Services*, vol. 2, Dec. 1991, pp. 1287–1291.
- [23] A. F. Molisch, L. J. Greenstein, and M. Shafi, "Propagation issues for cognitive radio," *Proceedings of the IEEE*, vol. 97, no. 5, pp. 787–804, May 2009.
- [24] C. Ho, T. S. Rappaport, and M. P. Koushik, "Antenna effects on indoor obstructed wireless channels and a deterministic image-based wide-band propagation model for in-building personal communication systems," *International Journal of Wireless Information Networks*, vol. 1, no. 1, pp. 61–76, Jan. 1994.
- [25] J. B. Andersen, T. S. Rappaport, and S. Yoshida, "Propagation measurements and models for wireless communications channels," *IEEE Communications Magazine*, vol. 33, no. 1, pp. 42–49, Jan. 1995.
- [26] T. S. Rappaport and S. Sandhu, "Radio-wave propagation for emerging wireless personal-communication systems," *IEEE Antennas and Propagation Magazine*, vol. 36, no. 5, pp. 14–24, Oct. 1994.
- [27] A. Alvarez, G. Valera, M. Lobeira, R. P. Torres, and J. L. Garcia, "Ultra wideband channel model for indoor environments," *Journal of Communications and Networks*, vol. 5, no. 4, pp. 309–318, 2003.
- [28] S. S. Ghassemzadeh, R. Jana, C. W. Rice, W. Turin, and V. Tarokh, "Measurement and modeling of an ultra-wide bandwidth indoor channel," *IEEE Transactions on Communications*, vol. 52, no. 10, pp. 1786–1796, Oct. 2004.
-

-
- [29] G. D. Durgin, T. S. Rappaport, and H. Xu, "Partition-based path loss analysis for in-home and residential areas at 5.85 GHz," in *IEEE Global Telecommunications Conference. GLOBECOM 1998: The Bridge to Global Integration*, vol. 2, Nov. 1998, pp. 904–909.
- [30] —, "Radio path loss and penetration loss measurements in and around homes and trees at 5.85 GHz," in *IEEE Antennas and Propagation Society International Symposium*, vol. 2, June 1998, pp. 618–621.
- [31] —, "5.85-GHz radio path loss and penetration loss measurements in and around homes and trees," *IEEE Communications Letters*, vol. 2, no. 3, pp. 70–72, Mar. 1998.
- [32] —, "Measurements and models for radio path loss and penetration loss in and around homes and trees at 5.85 GHz," *IEEE Transactions on Communications*, vol. 46, no. 11, pp. 1484–1496, Nov. 1998.
- [33] G. D. Durgin, V. Kukshya, and T. S. Rappaport, "Wideband measurements of angle and delay dispersion for outdoor and indoor peer-to-peer radio channels at 1920 MHz," *IEEE Transactions on Antennas and Propagation*, vol. 51, no. 5, pp. 936–944, May 2003.
- [34] —, "Joint angle and delay spread statistics for 1920 MHz peer-to-peer wireless channels," in *IEEE Antennas and Propagation Society International Symposium*, vol. 2, July 2001, pp. 182–185.
- [35] N. Patwari, G. D. Durgin, T. S. Rappaport, and R. J. Boyle, "Peer-to-peer low antenna outdoor radio wave propagation at 1.8 GHz," in *IEEE 49th Vehicular Technology Conference*, vol. 1, Jul. 1999, pp. 371–375.
- [36] J. W. McKown and R. L. Hamilton, Jr., "Ray tracing as a design tool for radio networks," *IEEE Network*, vol. 5, no. 6, pp. 27–30, Nov. 1991.
- [37] G. E. Athanasiadou, A. R. Nix, and J. P. McGeehan, "A ray tracing algorithm for microcellular wideband propagation modelling," in *IEEE 45th Vehicular Technology Conference*, vol. 1, Jul. 1995, pp. 261–265.
- [38] K. R. Schaubach, N. J. Davis, and T. S. Rappaport, "A ray tracing method for predicting path loss and delay spread in microcellular environments," in *IEEE 42nd Vehicular Technology Conference*, May 1992, pp. 932–935.
- [39] S. Y. Seidel and T. S. Rappaport, "A ray tracing technique to predict path loss and delay spread inside buildings," in *IEEE Global Telecommunications Conference, 1992*, vol. 2, Dec. 1992, pp. 649–653.
- [40] —, "Site-specific propagation prediction for wireless in-building personal communication system design," *IEEE Transactions on Vehicular Technology*, vol. 43, no. 4, pp. 879–891, Nov. 1994.
- [41] S. Y. Seidel, K. R. Schaubach, T. T. Tran, and T. S. Rappaport, "Research in site-specific propagation modeling for pcs system design," in *43rd IEEE Vehicular Technology Conference*, May 1993, pp. 261–264.
- [42] R. R. Skidmore, T. S. Rappaport, and A. L. Abbott, "Interactive coverage region and system design simulation for wireless communication systems in multifloored indoor environments: SMT plus," in *5th IEEE International Conference on Universal Personal Communications*, vol. 2, Sept. 1996, pp. 646–650.
- [43] S. Y. Seidel and T. S. Rappaport, "Path loss prediction in multifloored buildings at 914 MHz," *Electronics Letters*, vol. 40, no. 2, pp. 207–217, Feb 1992.
- [44] G. D. Durgin, N. Patwari, and T. S. Rappaport, "Improved 3D ray launching method for wireless propagation prediction," *Electronics Letters*, vol. 33, no. 16, pp. 1412–1413, July 1997.
-

-
- [45] T. S. Rappaport *et al.*, “Statistical channel impulse response models for factory and open plan building radio communication system design,” *IEEE Transactions on Communications*, vol. 39, no. 5, pp. 794–807, May 1991.
- [46] T. S. Rappaport, W. Huang, and M. J. Feuerstein, “Performance of decision feedback equalizers in simulated urban and indoor radio channels,” in *IEICE TRANSACTIONS on Communications*, vol. E76-B, no. 2, Feb. 1993, pp. 78–79.
- [47] T. S. Rappaport *et al.*, “900-MHz multipath propagation measurements for US digital cellular radiotelephone,” *IEEE Transactions on Vehicular Technology*, vol. 39, no. 2, pp. 132–139, May 1990.
- [48] S. Y. Seidel *et al.*, “Path loss, scattering and multipath delay statistics in four European cities for digital cellular and microcellular radiotelephone,” *IEEE Transactions on Vehicular Technology*, vol. 40, no. 4, pp. 721–730, Nov. 1991.
- [49] T. S. Rappaport, *Wireless Communications: Principles and Practice*, 2nd ed. Upper Saddle River, NJ: Prentice Hall, 2002.
- [50] J. E. Nuckols, “Implementation of geometrically based single-bounce models for simulation of angle-of-arrival of multipath delay components in the wireless channel simulation tools, SMRCIM and SIRCIM,” *Virginia Tech Library, Master of Science*, 1999.
- [51] E. Perahia, C. Cordeiro, M. Park, and L. L. Yang, “IEEE 802.11ad: Defining the next generation multi-Gbps Wi-Fi,” in *7th IEEE Consumer Communications and Networking Conference (CCNC)*, Jan. 2010, pp. 1–5.
- [52] N. Guo, R. C. Qiu, S. Mo, and K. Takahashi, “60-GHz millimeter-wave radio: Principle, technology, and new results,” *EURASIP Journal on Wireless Communications and Networking*, vol. 2007, no. 1, pp. 48–48, 2007.
- [53] R. C. Daniels, J. N. Murdock, T. S. Rappaport, and R. W. Heath, “60 GHz wireless: Up close and personal,” *IEEE Microwave Magazine*, vol. 11, pp. 44–55, Dec. 2010.
- [54] S. K. Yong and C. C. Chong, “An overview of multigigabit wireless through millimeter wave technology: potentials and technical challenges,” *EURASIP Journal on Wireless Communications and Networking*, vol. 2007, no. 1, pp. 50–50, 2007.
- [55] C. H. Doan, S. Emami, D. A. Sobel, A. M. Niknejad, and R. W. Brodersen, “Design considerations for 60 GHz CMOS radios,” *IEEE Communications Magazine*, vol. 42, no. 12, pp. 132–140, Dec. 2004.
- [56] S. K. Reynolds, B. A. Floyd, U. R. Pfeiffer, T. Beukema, J. Grzyb, C. Haymes, B. Gaucher, and M. Soyuer, “A silicon 60-GHz receiver and transmitter chipset for broadband communications,” *IEEE Journal of Solid-State Circuits*, vol. 41, no. 12, pp. 2820–2831, Dec. 2006.
- [57] F. Gutierrez, K. Parrish, and T. S. Rappaport, “On-chip integrated antenna structures in CMOS for 60 GHz WPAN systems,” in *IEEE Global Telecommunications Conference, 2009. GLOBECOM 2009*, Nov 2009, pp. 1–7.
- [58] M. Chelouche and A. Plattner, “Mobile broadband system (MBS): trends and impact on 60 GHz band MMIC development,” *Electronics Communication Engineering Journal*, vol. 5, no. 3, pp. 187–197, June 1993.
- [59] P. Smulders, “Exploiting the 60 GHz band for local wireless multimedia access: prospects and future directions,” *IEEE Communications Magazine*, vol. 40, no. 1, pp. 140–147, Jan. 2002.
-

-
- [60] Y. Shoji, K. Hamaguchi, and H. Ogawa, "Millimeter-wave remote self-heterodyne system for extremely stable and low-cost broad-band signal transmission," *IEEE Transactions on Microwave Theory and Techniques*, vol. 50, no. 6, pp. 1458–1468, June 2002.
- [61] D. Cabric, M. S. Chen, D. A. Sobel, S. Wang, J. Yang, and R. W. Brodersen, "Novel radio architectures for uwb, 60 GHz, and cognitive wireless systems," *EURASIP Journal on Wireless Communications and Networking*, no. 2, pp. 22–22, 2006.
- [62] Y. Takimoto and T. Ihara, "Research activities on millimeter wave indoor communication systems in japan," in *IEEE MTT-S International Microwave Symposium Digest*, Jun. 1993, pp. 673–676 vol.2.
- [63] T. Ihara, T. Manabe, M. Fujita, T. Matsui, and Y. Sugimoto, "Research activities on millimeter-wave indoor wireless communication systems at CRL," in *1995 Fourth IEEE International Conference on Universal Personal Communications*, Nov. 1995, pp. 197–200.
- [64] P. Shrivastava and T. R. Rao, "Performance investigations with antipodal linear tapered slot antenna on 60 GHz radio link in a narrow hallway environment," *Progress In Electromagnetics Research C*, vol. 58, pp. 69–77, 2015.
- [65] A. Kumar and T. R. Rao, "Analysis of planning and deployment issues for short range gigabit radio's at 60 GHz," in *International Conference on Communications and Signal Processing (ICCSP)*, April 2013, pp. 24–28.
- [66] S. Ramesh and T. R. Rao, "Indoor radio link characterization studies for millimeter wave wireless communications utilizing dielectric loaded exponentially tapered slot antenna," *Journal of Electromagnetic Waves and Applications*, vol. 29, no. 4, pp. 551–564, Feb. 2015.
- [67] P. F. M. Smulders and A. G. Wagemans, "Wide-band measurements of mm-wave indoor radio channels," in *Third IEEE International Symposium on Personal, Indoor and Mobile Radio Communications (PIMRC)*, Oct. 1992, pp. 329–333.
- [68] —, "Wideband indoor radio propagation measurements at 58 GHz," *Electronics Letters*, vol. 28, no. 13, pp. 1270–1272, June 1992.
- [69] —, "Frequency-domain measurement of the millimeter wave indoor radio channel," *IEEE Transactions on Instrumentation and Measurement*, vol. 44, no. 6, pp. 1017–1022, Dec. 1995.
- [70] H. Xu, V. Kukshya, and T. S. Rappaport, "Spatial and temporal characterization of 60 GHz indoor channels," in *52nd IEEE Vehicular Technology Conference (IEEE-VTS Fall VTC 2000)*, vol. 1, Sept. 2000, pp. 6–13.
- [71] M. Bensebti, J. P. McGeehan, and M. A. Beach, "Indoor multipath radio propagation measurements and characterisation at 60 GHz," in *21st European Microwave Conference*, vol. 2, Sept. 1991, pp. 1217–1222.
- [72] T. Zwick, T. J. Beukema, and H. Nam, "Wideband channel sounder with measurements and model for the 60 GHz indoor radio channel," *IEEE Transactions on Vehicular Technology*, vol. 54, no. 4, pp. 1266–1277, July 2005.
- [73] S. Geng, J. Kivinen, X. Zhao, and P. Vainikainen, "Millimeter-wave propagation channel characterization for short-range wireless communications," *IEEE Transactions on Vehicular Technology*, vol. 58, no. 1, pp. 3–13, Jan. 2009.
- [74] S. Geng, J. Kivinen, and P. Vainikainen, "Propagation characterization of wideband indoor radio channels at 60 GHz," in *IEEE International Symposium on Microwave, Antenna, Propagation and EMC Technologies for Wireless Communications*, vol. 1, Aug. 2005, pp. 314–317.
-

-
- [75] C. R. Anderson and T. S. Rappaport, "In-building wideband partition loss measurements at 2.5 and 60 GHz," *IEEE Transactions on Wireless Communications*, vol. 3, no. 3, pp. 922–928, May 2004.
- [76] C. R. Anderson *et al.*, "In-building wideband multipath characteristics at 2.5 and 60 GHz," in *2002 IEEE 56th Vehicular Technology Conference, Proceedings VTC 2002-Fall*, vol. 1, 2002, pp. 97–101.
- [77] T. Manabe, Y. Miura, and T. Ihara, "Effects of antenna directivity and polarization on indoor multipath propagation characteristics at 60 GHz," *IEEE Journal on selected Areas in Communications*, vol. 14, no. 3, pp. 441–448, Apr. 1996.
- [78] T. Manabe, K. Sato, H. Masuzawa, K. Taira, T. Ihara, Y. Kasashima, and K. Yamaki, "Polarization dependence of multipath propagation and high-speed transmission characteristics of indoor millimeter-wave channel at 60 GHz," *IEEE Transactions on Vehicular Technology*, vol. 44, no. 2, pp. 268–274, May 1995.
- [79] N. Moraitis and P. Constantinou, "Millimeter wave propagation measurements and characterization in an indoor environment for wireless 4G systems," in *IEEE 16th International Symposium on Personal, Indoor and Mobile Radio Communications (PIMRC)*, vol. 1, Sept. 2005, pp. 594–598.
- [80] A. Maltsev, E. Perahia, R. Maslennikov, A. Sevastyanov, A. Lomayev, and A. Khoryaev, "Impact of polarization characteristics on 60-GHz indoor radio communication systems," *IEEE Antennas and Wireless Propagation Letters*, vol. 9, pp. 413–416, 2010.
- [81] E. Torkildson, C. Sheldon, U. Madhow, and M. Rodwell, "Millimeter-wave spatial multiplexing in an indoor environment," in *IEEE GLOBECOM Workshops*, Nov. 2009, pp. 1–6.
- [82] E. Torkildson, U. Madhow, and M. Rodwell, "Indoor millimeter wave MIMO: Feasibility and performance," *IEEE Transactions on Wireless Communications*, vol. 10, no. 12, pp. 4150–4160, Dec. 2011.
- [83] K. Haneda, J. Jarvelainen, A. Karttunen, M. Kyro, and J. Putkonen, "Indoor short-range radio propagation measurements at 60 and 70 GHz," in *2014 8th European Conference on Antennas and Propagation (EuCAP)*, Apr. 2014, pp. 634–638.
- [84] J. Poutanen, J. Salmi, K. Haneda, V. Kolmonen, and P. Vainikainen, "Angular and shadowing characteristics of dense multipath components in indoor radio channels," *IEEE Transactions on Antennas and Propagation*, vol. 59, no. 1, pp. 245–253, Jan. 2011.
- [85] M. Lei, J. Zhang, T. Lei, and D. Du, "28-GHz indoor channel measurements and analysis of propagation characteristics," in *2014 IEEE 25th Annual International Symposium on Personal, Indoor, and Mobile Radio Communication (PIMRC)*, Sept. 2014, pp. 208–212.
- [86] X. Wu *et al.*, "28 GHz indoor channel measurements and modelling in laboratory environment using directional antennas," in *2015 9th European Conference on Antennas and Propagation (EuCAP)*, Apr. 2015, pp. 1–5.
- [87] H. Katsuyuki, "Channel models and beamforming at millimeter-wave frequency bands," *IEICE Transactions on Communications*, vol. E98, no. 5, pp. 755–772, May 2015.
- [88] FCC, "Allocations and service rules for the 71–76 GHz, 81–86 GHz, and 92–95 GHz bands," *FCC Memorandum Opinion and Order 05–45*, Federal Communications Commission, Washington D. C., 2010.
- [89] ECC, "Radio frequency channel arrangements for fixed service systems operating in the bands 71–76 GHz and 81–86 GHz," *ECC Recommendation (05)07*, Electronic Communications Committee, 2005.
-

-
- [90] Ofcom, “Making spectrum available for the 71–78 GHz and 81–86 GHz bands,” Nov. 2006.
- [91] DGTP-001-005, “Consultation on a renewed spectrum policy framework for Canada and continued advancement in spectrum managements,” Sept. 2005.
- [92] Federal Communications Commission, “FCC 14-154,” Oct. 2014. [Online]. Available: https://apps.fcc.gov/edocs_public/attachmatch/FCC-14-154A1.pdf
- [93] Federal Communications Commission, “FCC 14-177,” Jan. 2015. [Online]. Available: <http://apps.fcc.gov/ecfs/proceeding/view?name=14-177>
- [94] Ofcom, “Spectrum above 6 GHz for future mobile communications,” Feb. 2015. [Online]. Available: http://stakeholders.ofcom.org.uk/binaries/consultations/above-6ghz/summary/spectrum_above_6_GHz_CFI.pdf
- [95] L. Yujiri, M. Shoucri, and P. Moffa, “Passive millimeter wave imaging,” *IEEE Microwave Magazine*, vol. 4, no. 3, pp. 39–50, Sept. 2003.
- [96] S. Y. Seidel and T. S. Rappaport, “914 MHz path loss prediction models for indoor wireless communications in multifloored buildings,” *IEEE Transactions on Antennas and Propagation*, vol. 40, no. 2, pp. 207–217, Feb 1992.
- [97] S. Deng, C. J. Slezak, G. R. MacCartney, Jr., and T. S. Rappaport, “Small wavelengths - big potential: millimeter wave propagation measurements for 5G,” *Microwave Journal*, vol. 57, no. 11, pp. 4–12, Sept. 2014.
- [98] Y. Azar, G. N. Wong, K. Wang, R. Mayzus, J. K. Schulz, H. Zhao, F. Gutierrez, Jr., D. Hwang, and T. S. Rappaport, “28 GHz propagation measurements for outdoor cellular communications using steerable beam antennas in New York City,” in *2013 IEEE International Conference on Communications (ICC)*, June 2013, pp. 5143–5147.
- [99] G. R. MacCartney, Jr. and T. S. Rappaport, “73 GHz millimeter wave propagation measurements for outdoor urban mobile and backhaul communications in New York City,” in *2014 IEEE International Conference on Communications (ICC)*, June 2014, pp. 4862–4867.
- [100] S. Nie, G. R. MacCartney, Jr., S. Sun, and T. S. Rappaport, “72 GHz millimeter wave indoor measurements for wireless and backhaul communications,” in *2013 IEEE 24th International Symposium on Personal Indoor and Mobile Radio Communications (PIMRC)*, Sept. 2013, pp. 2429–2433.
- [101] D. Cox, “Delay doppler characteristics of multipath propagation at 910 MHz in a suburban mobile radio environment,” *IEEE Transactions on Antennas and Propagation*, vol. 20, no. 5, pp. 625–635, Sept. 1972.
- [102] R. J. Pirkl and G. D. Durgin, “Optimal sliding correlator channel sounder design,” *IEEE Transactions on Wireless Communications*, vol. 7, no. 9, pp. 3488–3497, Sept. 2008.
- [103] S. Deng, M. K. Samimi, and T. S. Rappaport, “28 GHz and 73 GHz millimeter-wave indoor propagation measurements and path loss models,” in *IEEE International Conference on Communications Workshops (ICC Workshops)*, June 2015.
- [104] T. S. Rappaport and S. Deng, “73 GHz wideband millimeter-wave foliage and ground reflection measurements and models,” in *IEEE International Conference on Communications Workshops (ICC Workshops)*, June 2015.
-

-
- [105] T. S. Rappaport *et al.*, “Wideband millimeter-wave propagation measurements and channel models for future wireless communication system design (invited paper),” *IEEE Transactions on Communications*, vol. 63, no. 9, pp. 3029–3056, Sept. 2015.
- [106] V. S. Abhayawardhana, I. J. Wassell, D. Crosby, M. P. Sellars, and M. Brown, “Comparison of empirical propagation path loss models for fixed wireless access systems,” in *IEEE 61st Vehicular Technology Conference, VTC 2005-Spring*, vol. 1, May 2005, pp. 73–77.
- [107] T. S. Rappaport and D. A. Hawbaker, “Wide-band microwave propagation parameters using circular and linear polarized antennas for indoor wireless channels,” *IEEE Transactions on Communications*, vol. 40, no. 2, pp. 240–245, Feb 1992.
- [108] P. Kyosti *et al.*, “WINNER II channel models,” European Commission, IST-WINNER, Tech. Rep. D1.1.2.
- [109] 3GPP, “Spatial channel model for multiple input multiple output (MIMO) simulations,” 3rd Generation Partnership Project (3GPP), TR 25.996, Sept. 2003. [Online]. Available: <http://www.3gpp.org>
- [110] M. K. Samimi, T. S. Rappaport, and G. R. MacCartney, Jr., “Probabilistic omnidirectional path loss models for millimeter-wave outdoor communications,” *IEEE Wireless Communications Letters*, vol. 4, no. 4, pp. 357–360, Aug 2015.
- [111] A. I. Sulyman, A. T. Nassar, M. K. Samimi, G. R. MacCartney, Jr., T. S. Rappaport, and A. Alsanie, “Radio propagation path loss models for 5G cellular networks in the 28 GHz and 38 GHz millimeter-wave bands,” *IEEE Communications Magazine*, vol. 52, no. 9, pp. 78–86, Sept. 2014.
- [112] G. R. MacCartney, Jr., J. Zhang, S. Nie, and T. S. Rappaport, “Path loss models for 5G millimeter wave propagation channels in urban microcells,” in *2013 IEEE Global Communications Conference (GLOBECOM)*, Dec. 2013, pp. 3948–3953.
- [113] S. Piersanti, L. A. Annoni, and D. Cassioli, “Millimeter waves channel measurements and path loss models,” in *2012 IEEE International Conference on Communications (ICC)*, June 2012, pp. 4552–4556.
- [114] S. Sun *et al.*, “Propagation path loss models for 5G urban micro- and macro-cellular scenarios,” in *IEEE 83rd Vehicular Technology Conference (VTC-Spring)*, May 2016, submitted paper.
- [115] P. Cardieri and T. S. Rappaport, “Statistics of the sum of lognormal variables in wireless communications,” in *2000 IEEE 51st Vehicular Technology Conference Proceedings. VTC 2000-Spring Tokyo.*, vol. 3, 2000, pp. 1823–1827.
- [116] —, “Statistical analysis of co-channel interference in wireless communications systems,” vol. 3, pp. 111–121, 2001.
- [117] J. He *et al.*, “Globally optimal transmitter placement for indoor wireless communication systems,” *IEEE Transactions on Wireless Communications*, vol. 3, no. 6, pp. 1906–1911, Nov. 2004.
- [118] J. C. Liberti and T. S. Rappaport, “Statistics of shadowing in indoor radio channels at 900 and 1900 MHz,” in *IEEE Military Communications Conference, 1992. MILCOM '92, Conference Record. Communications - Fusing Command, Control and Intelligence.*, Oct. 1992, pp. 1066–1070.
- [119] G. R. MacCartney, Jr., M. K. Samimi, and T. S. Rappaport, “Exploiting directionality for millimeter-wave wireless system improvement,” in *2015 IEEE International Conference on Communications (ICC)*, June 2015, pp. 4019–4025.
-

-
- [120] S. Sun, T. S. Rappaport, R. W. Heath, A. Nix, and S. Rangan, "MIMO for millimeter-wave wireless communications: beamforming, spatial multiplexing, or both?" *IEEE Communications Magazine*, vol. 52, no. 12, pp. 110–121, Dec. 2014.
- [121] T. S. Rappaport, F. Gutierrez, Jr., E. Ben-Dor, J. N. Murdock, Y. Qiao, and J. I. Tamir, "Broadband millimeter-wave propagation measurements and models using adaptive-beam antennas for outdoor urban cellular communications," in *IEEE Transactions on Antennas and Propagation*, vol. 61, no. 4, Apr. 2013, pp. 1850 – 1859.
- [122] E. Ben-Dor, T. S. Rappaport, Y. Qiao, and S. J. Lauffenburger, "Millimeter-wave 60 GHz outdoor and vehicle AOA propagation measurements using a broadband channel sounder," in *2011 IEEE Global Telecommunications Conference (GLOBECOM 2011)*, Dec. 2011, pp. 1–6.
- [123] T. S. Rappaport, E. Ben-Dor, J. N. Murdock, and Y. Qiao, "38 GHz and 60 GHz angle-dependent propagation for cellular and peer-to-peer wireless communications," in *2012 IEEE International Conference on Communications (ICC)*, June 2012, pp. 4568–4573.
- [124] P. Nobles, D. Ashworth, and F. Halsall, "Propagation measurements in an indoor radio environment at 2, 5 and 17 GHz," in *IEEE Colloquium on High Bit Rate UHF/SHF Channel Sounders - Technology and Measurement*, Dec. 1993, pp. 4–6.
- [125] S. Sun and T. S. Rappaport, "Multi-beam antenna combining for 28 GHz cellular link improvement in urban environments," in *2013 IEEE Global Communications Conference (GLOBECOM)*, Dec. 2013, pp. 3754–3759.
- [126] S. Sun, G. R. MacCartney, Jr., M. K. Samimi, S. Nie, and T. S. Rappaport, "Millimeter wave multi-beam antenna combining for 5G cellular link improvement in New York City," in *2014 IEEE International Conference on Communications (ICC)*, June 2014, pp. 5468–5473.
- [127] M. Kaske, C. Schneider, W. Kotterman, and R. Thoma, "Solving the problem of choosing the right MIMO measurement antenna: Embedding/de-embedding," in *Proceedings of the 5th European Conference on Antennas and Propagation (EUCAP)*, Apr. 2011, pp. 2551–2555.
- [128] G. R. MacCartney, Jr., M. K. Samimi, and T. S. Rappaport, "Omnidirectional path loss models in New York City at 28 GHz and 73 GHz," in *2014 IEEE 25th International Symposium on Personal Indoor and Mobile Radio Communications (PIMRC)*, Sept. 2014, pp. 227–231.
- [129] S. Sun, G. R. MacCartney, Jr., M. K. Samimi, and T. S. Rappaport, "Synthesizing omnidirectional antenna patterns, received power and path loss from directional antennas for 5G millimeter-wave communications," in *2015 IEEE Global Communications Conference (GLOBECOM)*, Dec. 2015.
- [130] U. Beckman, C. Wahlberg, "Antenna systems for polarization diversity: Reducing the size and number of antennas needed for mobile network deployment through polarization diversity," *Microwave Journal*, May. 1997.
- [131] A. Ghosh, T. A. Thomas, M. C. Cudak, R. Ratasuk, P. Moorut, F. W. Vook, T. S. Rappaport, G. R. MacCartney, S. Sun, and S. Nie, "Millimeter-wave enhanced local area systems: A high-data-rate approach for future wireless networks," *IEEE Journal on Selected Areas in Communications*, vol. 32, no. 6, pp. 1152–1163, June 2014.
- [132] Y. Zahedi, R. Ngah, U. Chude-Onkonkwo, S. Nunoo, and M. Mokayef, "Modeling the RMS delay spread in time-varying UWB communication channels," in *2014 5th International Conference on Intelligent and Advanced Systems (ICIAS)*, June 2014, pp. 1–5.
-

-
- [133] H. Hashemi and D. Tholl, "Statistical modeling and simulation of the RMS delay spread of indoor radio propagation channels," *IEEE Transactions on Vehicular Technology*, vol. 43, no. 1, pp. 110–120, Feb. 1994.
- [134] H. Yang, P. F. M. Smulders, and M. Herben, "Indoor channel measurements and analysis in the frequency bands 2 GHz and 60 GHz," in *IEEE 16th International Symposium on Personal, Indoor and Mobile Radio Communications*, vol. 1, Sept. 2005, pp. 579–583.
- [135] D. Devasirvatham, "A comparison of time delay spread and signal level measurements within two dissimilar office buildings," *IEEE Transactions on Antennas and Propagation*, vol. 35, no. 3, pp. 319–324, Mar. 1987.
- [136] J. Qiao, X. Shen, J. W. Mark, and Y. He, "MAC-layer concurrent beamforming protocol for indoor millimeter-wave networks," *IEEE Transactions on Vehicular Technology*, vol. 64, no. 1, pp. 327–338, Jan. 2015.
- [137] S. Mao, Z. He, and T. S. Rappaport, "On link scheduling under blockage and interference in 60 GHz Ad Hoc networks," *IEEE Access*, vol. 3, pp. 1437–1449, Sept. 2015.
- [138] P. Nobles and F. Halsall, "Delay spread and received power measurements within a building at 2 GHz, 5 GHz and 17 GHz," in *International Conference on Antennas and Propagation*, vol. 2, Apr. 1997, pp. 319–324.
-